Optical Imaging of Emergent Transport Phenomena in Transition Metal Oxides

Dissertation
der Mathematisch-Naturwissenschaftlichen Fakultät
der Eberhard Karls Universität Tübingen
zur Erlangung des Grades eines
Doktors der Naturwissenschaften
(Dr. rer. nat.)

vorgelegt von
Farnaz Tahouni
aus Tabriz/Iran

Tübingen
2026

Gedruckt mit Genehmigung der Mathematisch-Naturwissenschaftlichen Fakultät der Eberhard Karls Universität Tübingen.

Tag der mündlichen Qualifikation:	07.09.2026
Dekan:	Prof. Dr. Thilo Stehle
1. Berichterstatter:	Prof. Dr. Dieter Kölle
2. Berichterstatter:	Prof. Dr. Alejandro Silhanek

Abstract

Transition metal oxides exhibit a close coupling between electronic, structural, thermal, and lattice degrees of freedom. This coupling gives rise to emergent phenomena such as metal–insulator transitions, phase coexistence, nonlinear transport, filament formation, and domain-mediated heat transport. Owing to these properties, materials such as V_2O_3, $NdNiO_3$, VO_2, and $SrTiO_3$ are promising platforms for future oxide electronics, neuromorphic devices, and energy-efficient information technologies.

This thesis investigates these phenomena by combining electrical transport measurements with spatially resolved optical microscopy. The central experimental approach is based on a multifunctional optical microscope that enables real-time imaging of devices during thermal, electrical or optical excitation. This method provides direct access to microscopic phase textures, metallic filament formation, and ferroelastic domain structures, allowing macroscopic transport behavior to be linked to the underlying spatial dynamics.

Using V_2O_3 as a model Mott insulator, local laser excitation is applied to perturb the first-order Mott metal–insulator transition. Optical imaging reveals that irradiation modifies the balance between metallic and insulating phases, reduces the hysteresis, and relaxes thermal history effects. In $NdNiO_3$ thin-film devices, electrothermal resistive switching is investigated. Joule heating drives the formation of metallic filaments, which are stabilized by the hysteresis of the transition and enable nonvolatile multistate resistance states. These states remain stable at constant temperature and can be reset by thermal cycling.

The thesis further explores phonon transport in $SrTiO_3$, where the formation of ferroelastic domain walls below the structural phase transition temperature of approximately 105 K modifies the heat flow in the hydrodynamic regime. Optical imaging shows sample-size dependent domain-

wall structures that act as intrinsic scattering centers and suppress the expected enhancement of hydrodynamic phonon transport. Finally, multiterminal VO_2 devices are investigated as electrothermal memristive systems. Simultaneous optical and electrical measurements reveal history-dependent metallic filament configurations that can be controlled by terminal biasing.

Together, these results demonstrate the importance of spatially resolved measurements for understanding functional behavior in transition metal oxides. By directly connecting microscopic phase and domain structures to macroscopic transport properties, this thesis provides insight into optical control of metastability, electrothermal switching, and domain-wall-mediated heat transport. The findings highlight transition metal oxides as versatile materials for future electronic, neuromorphic, and thermal technologies.

Kurzfassung

Übergangsmetalloxide zeichnen sich durch eine enge Kopplung zwischen elektronischen, strukturellen, thermischen und Gitter-Freiheitsgraden aus. Diese Kopplung führt zu emergenten Phänomenen wie Metall–Isolator-Übergängen, Phasenkoexistenz, nichtlinearem Transport, Filamentbildung und domänenvermitteltem Wärmetransport. Aufgrund dieser Eigenschaften sind Materialien wie V_2O_3, $NdNiO_3$, VO_2 und $SrTiO_3$ vielversprechende Plattformen für eine zukünftige Oxidelektronik, neuromorphe Bauelemente und energieeffiziente Informationstechnologien.

Diese Arbeit untersucht diese Phänomene durch die Kombination elektrischer Transportmessungen mit ortsaufgelöster optischer Mikroskopie. Der zentrale experimentelle Ansatz basiert auf einem multifunktionalen optischen Mikroskop, das die Echtzeit-Abbildung von Bauelementen während elektrischer oder optischer Anregung ermöglicht. Diese Methode erlaubt einen direkten Zugang zu mikroskopischen Phasenstrukturen, metallischer Filamentbildung und ferroelastischen Domänenstrukturen und ermöglicht es, das makroskopische Transportverhalten mit den zugrunde liegenden räumlichen Dynamiken zu verknüpfen.

Unter Verwendung von V_2O_3 als Modell-Mott-Isolator wird lokale Laseranregung eingesetzt, um den Mott-Metall–Isolator-Übergang erster Ordnung gezielt zu beeinflussen. Optische Abbildungen zeigen, dass die Bestrahlung das Gleichgewicht zwischen metallischen und isolierenden Phasen verändert, die Hysterese reduziert und thermische Vorgeschichtseffekte abschwächt. In $NdNiO_3$-Dünnschichtbauelementen wird elektrothermisches resistives Schalten untersucht. Joule-Heizung führt zur Bildung metallischer Filamente, die durch die Hysterese des Übergangs stabilisiert werden und nichtflüchtige multistabile Widerstandszustände ermöglichen. Diese Zustände bleiben bei konstanter Temperatur stabil und können durch thermisches Zyklen zurückgesetzt

werden.

Darüber hinaus untersucht diese Arbeit den Phononentransport in $SrTiO_3$, wobei ferroelastische Domänenwände, die unterhalb der strukturellen Übergangstemperatur von etwa 105 K entstehen, den Wärmetransport im hydrodynamischen Regime verändern. Optische Abbildungen zeigen von der Probengröße abhängige Domänenwandstrukturen, die als intrinsische Streuzentren wirken und die erwartete Verstärkung des hydrodynamischen Phononentransports unterdrücken. Abschließend werden multiterminale VO_2-Bauelemente als elektrothermische memristive Systeme untersucht. Simultane optische und elektrische Messungen zeigen von der Vorgeschichte abhängige metallische Filamentkonfigurationen, die durch die angelegte Spannung an verschiedenen Kontakten kontrolliert werden können.

Zusammenfassend zeigen diese Ergebnisse die Bedeutung ortsaufgelöster Messmethoden für das Verständnis funktioneller Eigenschaften in stark korrelierten Oxiden. Durch die direkte Verknüpfung mikroskopischer Phasen- und Domänenstrukturen mit makroskopischen Transporteigenschaften liefert diese Arbeit Einblicke in die optische Kontrolle von Metastabilität, elektrothermischem Schalten und domänenwandvermittelten Wärmetransport. Die Ergebnisse unterstreichen das Potenzial von Übergangsmetalloxiden als vielseitige Materialien für zukünftige elektronische, neuromorphe und thermische Technologien.

List of Publications

This cumulative thesis is based on the four publications listed below, which investigate phase transitions, resistive switching, domain-wall physics, and thermal transport in oxide materials. Publications 1 and 2 focus on electrically and optically induced metal–insulator transitions in V_2O_3 and $NdNiO_3$, respectively. Publication 3 explores the impact of ferroelastic domain walls on hydrodynamic phonon transport in $SrTiO_3$, while Publication 4 examines filament formation and electrothermal switching in multiterminal VO_2 devices. The full texts of the publications are included in the appendix of this thesis.

Publication 1 T. Luibrand, L. Fratino, **F. Tahouni-Bonab**, A. Kronman, Y. Kalcheim, I. K. Schuller, M. Rozenberg, R. Kleiner, D. Koelle, S. Guénon
Laser-induced quenching of metastability at the Mott insulator to metal transition
Phys. Rev. B **110**, L081108 (2024)

Publication 2 **F. Tahouni-Bonab**, M. Hepting, T. Luibrand, G. Cristiani, C. Schmid, G. Logvenov, B. Keimer, R. Kleiner, D. Koelle, S. Guénon
Nonvolatile multistate electrothermal resistive switching in a strongly correlated insulator thin-film device
Phys. Rev. Applied **24**, 034014 (2025)

Publication 3 S. Guo, **F. Tahouni-Bonab**, J. Han, J. He, T. Hoke, D. Koelle, R. Kleiner, J. Zhou, S. Guénon, S. Lee
Domain-wall-driven anomaly in hydrodynamic phonon transport in $SrTiO_3$
Newton, 100407 (2026)

Publication 4 S. Smink, **F. Tahouni-Bonab**, W. Schmitz, D. J. v. Rensburg, J. v. Putten, L. Cool, C. Evers, S. Guénon, R. Kleiner, D. Koelle, C. M. M. Rosário, H. Hilgenkamp
History-dependent filament configuration in multiterminal electrothermal memristors
Appl. Phys. Lett. **128**, 243501 (2026)

List of Acronyms

CMOS complementary metal–oxide–semiconductor

DMFT dynamical mean-field theory

IMT insulator–metal transition

MIT metal–insulator transition

LHB lower Hubbard band

UHB upper Hubbard band

ZSA Zaanen–Sawatzky–Allen

AFD antiferrodistortive

FDW ferroelastic domain wall

WFPM wide-field polarization microscopy

LTSPM low-temperature scanning laser polarization microscopy

ETM electrothermal memristor

NNO $NdNiO_3$

STO $SrTiO_3$

Contents

1 Introduction **1**

2 Summary of publications and contributions **15**

2.1 **Publication 1:** Laser-induced quenching of metastability at the Mott insulator to metal transition 15

2.2 **Publication 2:** Nonvolatile multistate electrothermal resistive switching in a strongly correlated insulator thin-film device 20

2.3 **Publication 3:** Domain-wall-driven anomaly in hydrodynamic phonon transport in $SrTiO_3$ 25

2.4 **Publication 4:** History-dependent filament configuration in multiterminal electrothermal memristors 31

3 Conclusion **37**

Bibliography **41**

Appended publications **55**

Acknowledgements **99**

1 Introduction

The remarkable progress of modern electronics over the past decades has been largely driven by the continuous miniaturization of semiconductor devices, commonly referred to as Moore's law[1,2]. This scaling has enabled significant improvements in computational performance, integration density, and energy efficiency. Within complementary metal–oxide–semiconductor (CMOS) technology, it was historically supported by Dennard scaling, where proportional voltage reduction ensured approximately constant power density[3].

As device dimensions approach the nanometer scale, however, this paradigm faces fundamental physical limitations. Quantum mechanical effects, such as direct tunneling through ultrathin gate dielectrics and source–drain tunneling, lead to increased leakage currents and degrade the distinction between ON and OFF states required for reliable switching[4–7]. Additionally, atomic-scale disorder and discrete dopant fluctuations introduce variability in device characteristics, limiting reproducibility. The breakdown of Dennard scaling further prevents voltage reduction, resulting in increased power density and heat generation, which constrain performance[8–10].

At the system level, the conventional von Neumann architecture introduces an additional bottleneck, as the separation of memory and processing units necessitates continuous data transfer, leading to increased latency and energy consumption[11]. This limitation is particularly critical for data-intensive applications, where the energy cost of data movement can exceed that of computation.

Together, these limitations have driven the search for alternative material platforms and device concepts that can provide functionalities beyond those achievable with conventional charge-based electronics. In this context, electronic oxide materials, particularly complex transition metal oxides, have emerged as a promising class of systems[12–14]. Unlike con-

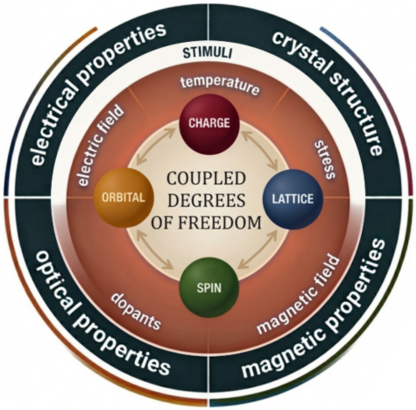


Figure 1.1: Schematic illustration of emergent properties in transition metal oxides from coupled microscopic degrees of freedom. External perturbations can drive phase transitions, giving rise to macroscopic functionalities. Figure is redrawn after Ref. [15]. © 2015 IEEE.

ventional semiconductors, the macroscopic properties of transition metal oxides are not solely determined by single-particle band structure, but instead arise from the collective interplay between charge, lattice, spin, and orbital degrees of freedom[15–18]. This strong coupling leads to complex phase diagrams with competing ground states, where small changes in external conditions can drive transitions between distinct electronic phases[17,18]. Depending on the material system, these phenomena may be governed by strong electronic correlations, lattice dynamics, or electron–phonon interactions, encompassing both correlation-driven phase transitions and unconventional transport regimes[19–23]. As a consequence, the electronic and thermal transport properties of oxide materials are highly sensitive to external perturbations such as temperature, electric field, current, and strain[24–29]. Figure 1.1 shows a schematic illustration of the interplay between various degrees of freedom under external perturbations, leading to the tunability of the physical properties of oxide materials.

This tunability, combined with the possibility of nonlinear and often abrupt responses, makes electronic oxides particularly attractive for applications in memory devices, neuromorphic computing, and energy-efficient switching technologies[15,30–33].

One of the most prominent examples of emergent behavior in transition metal oxides, many of which belong to the class of strongly correlated materials, is the metal–insulator transition (MIT), in which a material undergoes a drastic change in electrical conductivity[16,34–36]. Unlike conventional semiconductor switching, which relies on gradual modulation of carrier density, the MIT involves a fundamental reorganization of the electronic state of the system, often accompanied by structural and lattice changes[37,38].

Two main frameworks are commonly used to describe MIT in strongly correlated materials. The first model is the Mott–Hubbard picture, based on the Hubbard model, which describes electrons moving in a periodic lattice within a single electronic band[39,40]. The corresponding Hamiltonian is

$$H = -t \sum_{\langle i,j \rangle,\sigma} c^{\dagger}_{i,\sigma} c_{j,\sigma} + U \sum_{i} n_{i,\uparrow} n_{i,\downarrow}, \tag{1.1}$$

where t is the hopping amplitude and U is the on-site Coulomb repulsion. When the Coulomb interaction exceeds the electronic bandwidth W, the electronic states split into lower and upper Hubbard bands (LHB and UHB), resulting in a Mott insulating state. On the other side, the second framework describes charge-transfer insulators, relevant for many transition metal oxides. In these materials, the oxygen p-band lies close to the transition metal d-band, and the lowest excitation corresponds to charge transfer from oxygen to the metal site, with an energy cost Δ smaller than U. So, there is n+1 electrons at the transition site. This process can be written as $d^n \rightarrow d^{n+1}\underline{L}$, where $\underline{L}$ denotes a ligand hole. The Zaanen–Sawatzky–Allen (ZSA) scheme classifies transition metal compounds based on these two models and according to the relative magnitudes of U and Δ[41]. Figures 1.2(a,b) illustrate the single-band Mott–Hubbard and multi-band charge-transfer models, while Figs. 1.2(c,d) present representative dynamical mean-field theory (DMFT) results showing how the Coulomb interaction governs the redistribution of spectral

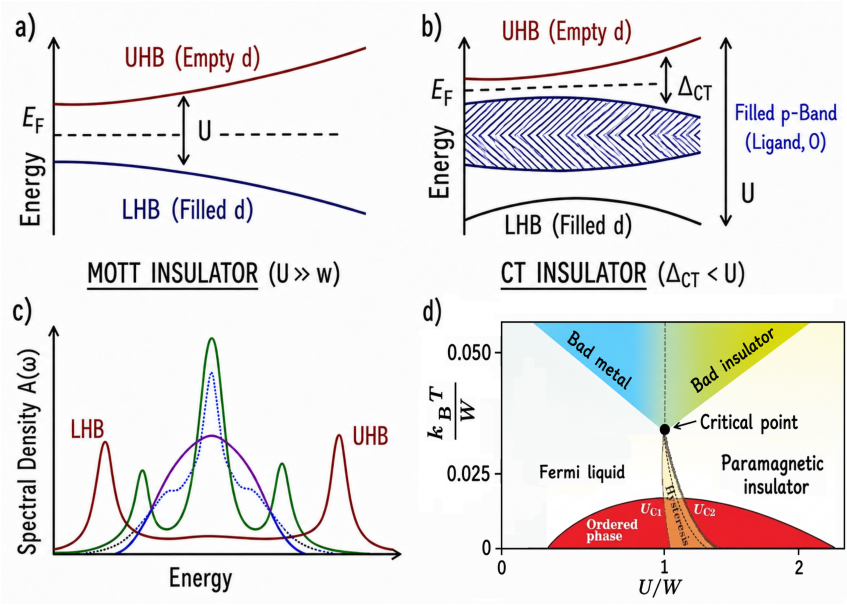


Figure 1.2: Overview of the fundamental models and Phase diagram in strongly correlated materials. (a) Single-band Mott–Hubbard model for a half-filled d band in Mott insulators with $U \gg W$. (b) Multi-band charge-transfer model for charge-transfer insulators, in which the charge-transfer gap Δ_{CT} is smaller than the interaction energy U. (c) The evolution of the spectral weight: Purple curve represents the metallic phase with small U/W. The blue dashed lines are the representative of critical region. Green and Red colors are the representative of LHB/UHB-like structure and insulating phase with large U/W, respectively. (d) Phase diagram of the MIT in strongly correlated materials. The figures in (c) and (d) are schematic representations based on DMFT calculations. Figure (c) adapted and modified from Ref. [42] with permission from authors and Fig. (d) adapted and modified from Ref. [43], © 2004 AIP Publishing.

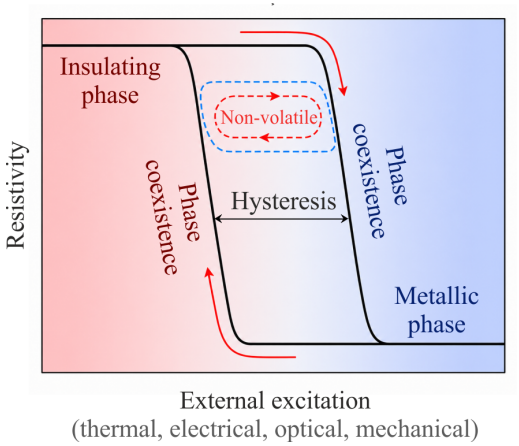


Figure 1.3: Schematic illustration of a first-order MIT. The transition can be triggered by a variety of external stimuli, including thermal, electrical, optical, and mechanical perturbations. As the excitation exceeds a critical threshold, the resistivity undergoes a pronounced change associated with the conversion between insulating and metallic phases. In the transition region, both phases may coexist, resulting in a hysteretic response and a bistable regime. Adapted and modified from Ref. [15]. © 2015 IEEE.

weight and the resulting MIT phase diagram in strongly correlated materials[42–46].

Among the various oxide systems exhibiting MITs, vanadium dioxide (VO_2)[47–50], vanadium sesquioxide (V_2O_3)[51–54], and neodymium nickelate ($NdNiO_3$)[55–57] represent prototypical examples of correlated materials with rich phase behavior. In VO_2, the transition occurs near room temperature and is accompanied by a structural change from a monoclinic insulating phase to a rutile metallic phase[47,50]. This transition can be triggered not only by temperature but also by electric field or current, making VO_2 a widely studied candidate for electronic switching devices[58–61].

V_2O_3 exhibits a classic Mott transition driven by strong electron–electron interactions, serving as a model system for studying correlation effects in solids[51,52]. Similarly, $NdNiO_3$, commonly referred to as NNO, exhibits a temperature-driven MIT that is strongly influenced by lattice distortions and strain, highlighting the importance of coupling between electronic and structural degrees of freedom[27,57,62].

Despite their differences, these materials share a common characteristic: the MIT is often spatially inhomogeneous. Rather than occurring uniformly throughout the sample, the transition proceeds through the nucleation and growth of metallic and insulating domains[50,63,64]. Near the transition, phase coexistence emerges, where regions with distinct electronic character coexist within the material. Under external bias, this spatial inhomogeneity can promote filamentary conduction pathways, where the current becomes concentrated in narrow and dynamically evolving regions[65–68].

A first-order MIT can be driven by various external stimuli, as illustrated in Fig. 1.3. In electrically driven experiments, the position of the operating point along the insulator–metal transition (IMT) curve is particularly important. The selected base temperature is one of the key parameters that controls the stability of the induced conducting state and therefore strongly influences the resulting resistive switching response.

The formation and evolution of conductive filaments are closely connected to resistive switching phenomena. Depending on the material parameters and experimental conditions, the switched state may either relax after removal of the external stimulus or remain stabilized. Relaxation of the switched state is typically associated with thermally driven or transient filament formation and corresponds to volatile behavior[69–72]. In contrast, stabilization of the switched state is often linked to structural rearrangements, phase stabilization, or defect- and oxygen vacancy related processes, enabling memory retention and corresponding to nonvolatile behavior[30,72–75].

This distinction is illustrated for NNO thin-film devices in Fig. 1.4. In Fig. 1.4(a), the device recovers its initial high-resistance state after completion of the voltage–current (I–V) sweep, indicating a volatile response.

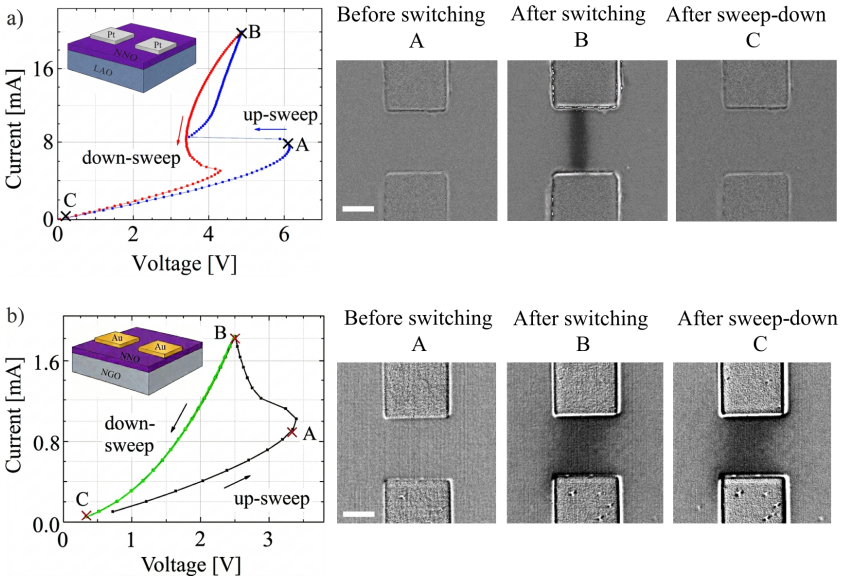


Figure 1.4: Volatile and nonvolatile electrothermal switching in strongly correlated NNO thin films. (a) I–V characteristic of a 45 nm-thick NNO device exhibiting volatile switching at $T = 80$ K . The accompanying photomicrographs were acquired during the up-sweep before switching at point A ($I_A = 8.8\,\mathrm{mA}$), after filament formation (dark regions) at the maximum current B ($I_B = 20\,\mathrm{mA}$), and after completion of the measurement at point C ($I_C = 0\,\mathrm{mA}$) during the down-sweep. The metallic filament formed during switching disappears when the current is reduced to zero, indicating volatile switching. (b) I–V characteristic of a 7 nm-thick NNO device exhibiting nonvolatile switching at $T = 167$ K. The optical images correspond to the device states before switching (A, $I_A = 0.8\,\mathrm{mA}$), after switching (B, $I_B = 1.8\,\mathrm{mA}$), and after completion of the measurement cycle at zero current (C, $I_C = 0\,\mathrm{mA}$). The first sweep is shown in black, while the second and third sweeps are plotted in red and green, respectively. Scale bars: 10 μm. Figure (a) adapted from Ref. [76] and the curve in Fig. (b) adapted and modified from appended publication 2. © 2025 American Physical Society.

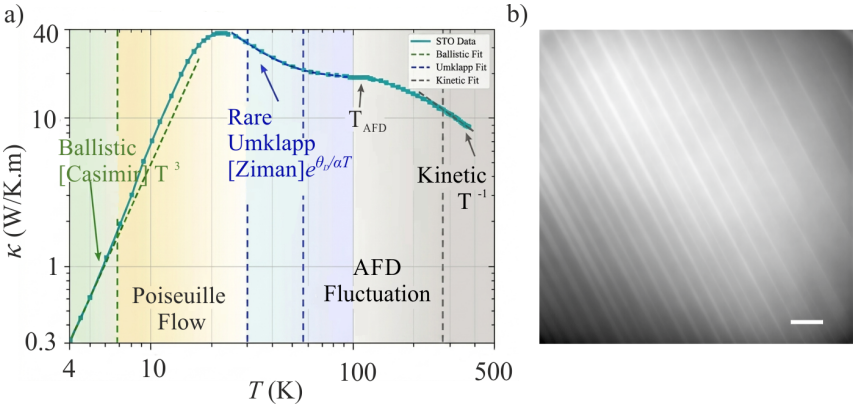


Figure 1.5: (a) Thermal conductivity of $SrTiO_3$ as a function of temperature, highlighting the dominant phonon scattering and transport regimes across the investigated temperature range. (b) Optical photomicrograph of a $SrTiO_3$ crystal acquired at $T = 50$ K, below the antiferrodistortive transition temperature ($T_{AFD} \approx 105$ K), revealing the ferroelastic domain structure formed in the tetragonal phase. Scale bar: 50 μm. Figure (a) is adapted and modified from Ref. [77], © 2018 American Physical Society and Fig. (b) reprinted from appended publication 3, with permission from Elsevier.

In contrast, Fig. 1.4(b) shows that the electrically induced low-resistance state is retained after the sweep, demonstrating nonvolatile switching.

This coexistence of volatile and nonvolatile switching behavior, together with the intrinsic nonlinear dynamics of correlated oxides, makes these materials highly attractive for applications in resistive memory and neuromorphic computing architectures[31–33,78–80].

Another key emergent phenomenon in transition metal oxides is the formation of domains and domain walls, which introduces an additional level of complexity to their physical properties. Domain walls, which separate regions of different phases, can exhibit electronic properties that are distinct from those of the surrounding bulk material[81,82]. In some cases,

domain walls can act as preferential conduction channels, while in others they may serve as barriers to transport[81,83]. The dynamics of domain walls under external stimuli, such as electric fields or temperature gradients, therefore play a key role in determining the overall transport properties of the material[82,84]. Understanding how these domain structures form, evolve, and interact is essential for controlling the functionality of oxide-based devices[83].

Strontium titanate ($SrTiO_3$, STO) is a complex oxide in which domain walls can play a central role in determining its physical behavior. In contrast to the strongly correlated systems described above, STO provides a complementary platform in which transport properties are governed primarily by lattice dynamics and electron–phonon interactions[21,85]. Although STO is a band insulator in its stoichiometric form, it exhibits a range of remarkable phenomena when doped or subjected to external perturbations, including superconductivity, high-mobility electron gases, and unusual thermal transport behavior[77,86–88]. In particular, STO has been shown to exhibit hydrodynamic transport regimes, where collective phonon excitations dominate heat conduction[77,89]. These properties make it an ideal system for exploring transport phenomena that are not directly driven by strong electronic correlations, but nevertheless fall outside the framework of conventional semiconductor physics.

The relevant thermal transport regimes are summarized in Fig. 1.5(a), which shows the thermal conductivity of STO across the investigated temperature range. The observed regimes include ballistic (Casimir), hydrodynamic (Poiseuille), and kinetic (Umklapp) transport, as well as fluctuations associated with the antiferrodistortive (AFD) transition. Below this transition, STO forms ferroelastic domain walls (FDWs), as shown in Fig. 1.5(b) for an optical image acquired at $T = 50$ K.

A unifying aspect of these oxide materials is that their macroscopic transport properties emerge from microscopic spatial processes that evolve dynamically under external stimuli. Conventional electrical transport measurements, while providing valuable information about global properties such as conductivity, do not capture the spatial complexity of these processes. As a result, key phenomena such as filament formation, domain evolution, and phase coexistence remain difficult to access using purely

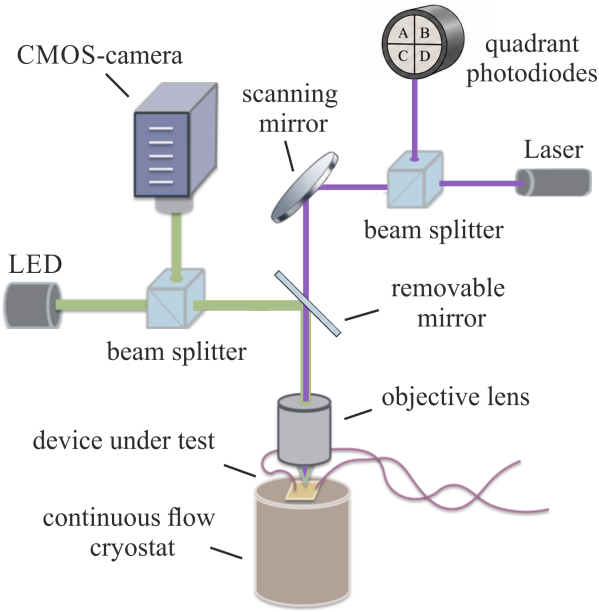


Figure 1.6: Simplified schematic of the multifunctional optical microscope setup. The instrument integrates electrical transport measurements with two optical microscopy modalities: wide-field polarization microscopy (WFPM) on the left, using illumination from a 528 nm LED light source, and Low-temperature scanning laser polarization microscopy (LTSPM) on the right, performed with a 405 nm laser. Figure adapted and modified from appended publication 1, © 2024 American Physical Society.

electrical techniques. To overcome this limitation, it is necessary to employ experimental approaches that combine electrical measurements with spatially resolved probes. The experimental investigations presented in this work focus on a range of complex oxide materials, providing a perspective on emergent transport phenomena in oxide systems.

In this thesis, the local spatial processes underlying the macroscopic transport properties of transition metal oxides are investigated by integrating electrical transport measurements with real-time optical imaging[90], as illustrated in Fig. 1.6. This approach enables the direct visualization of spatial inhomogeneities and their evolution during electrically driven processes[69,91–93]. By correlating local optical contrast with global electrical response, it becomes possible to establish a direct link between microscopic mechanisms and macroscopic behavior.

Through systematic studies of transition metal oxides, this thesis aims to elucidate the role of spatial inhomogeneity, domain dynamics, and nonequilibrium processes in determining their transport behavior. Particular emphasis is placed on understanding the mechanisms underlying resistive switching, including both volatile and nonvolatile regimes, domain evolution, and the formation of conductive filaments. In addition, the influence of domain walls on transport properties is investigated, together with the extent to which these processes can be controlled and manipulated through external parameters such as electric field, current, and temperature.

Beyond their fundamental significance, these phenomena are closely related to potential technological applications. The ability to achieve abrupt and energy-efficient switching, combined with intrinsic memory effects and nonlinear dynamics, makes transition metal oxides attractive candidates for next-generation electronic devices. In particular, their relevance for neuromorphic computing, where information processing is inspired by the human brain, has attracted significant attention. In such systems, the coexistence of multiple states, history-dependent behavior, and spatially distributed activity can be exploited to implement functionalities that are difficult to realize with conventional semiconductor technology.

Publication 1 demonstrates the use of laser irradiation as a powerful tool to locally perturb and control the phase transition in strongly correlated V_2O_3 thin films. A focused laser beam is employed as a controllable external stimulus to manipulate the material across its first-order metal–insulator transition. By combining spatially resolved optical imaging with scanning laser exposure, the evolution of metallic and insulating domains is monitored in real time during both heating and cooling cycles. This approach enables direct investigation of the influence of laser-induced

perturbations on metastable states and reveals how the system is driven toward thermodynamic equilibrium. The results show that local laser excitation can effectively control phase coexistence and thermal-history-dependent behavior in a correlated electron system.

Another correlated oxide that has emerged as a highly attractive platform for unconventional electronic functionalities is NNO, due to its pronounced first-order insulator–metal transition and strong thermal hysteresis, as explored in **Publication 2**. This intrinsic phase-transition physics enables stable multistate resistive switching, which is highly relevant for high-density memory and neuromorphic technologies. Current-induced Joule heating triggers a pronounced electrothermal instability that drives the formation of a metallic filament within the insulating matrix. In contrast to ion-migration-based devices, the filament is purely thermal in origin and is stabilized by the hysteretic behavior of the resistance–temperature relation, resulting in reliable nonvolatile switching. The device supports more than 100 distinct and stable resistance states, which remain robust at constant temperature and can be fully reset non-destructively by thermal cycling. These results highlight electrothermal switching in correlated oxides as a promising route toward high-endurance analog memory and neuromorphic systems.

In **Publication 3**, the focus is on understanding heat transport in STO, which is one of the key physical properties relevant for oxide electronics and for exploring unconventional phonon dynamics. Owing to its high crystalline quality and low-energy soft phonon modes, STO provides an ideal platform for hydrodynamic phonon transport. Below the antiferrodistortive transition, FDWs emerge and strongly influence phonon propagation. To establish a direct link between structure and transport, polarized optical microscopy was employed to image domain walls in samples of different widths. The analysis reveals that reducing the sample width increases the domain-wall density and decreases the characteristic spacing Λ between the domain walls. In combination with thermal transport measurements, this demonstrates that domain walls act as internal scattering centers that disrupt collective phonon flow. As a result, decreasing the sample size suppresses phonon Poiseuille transport and reduces the thermal conductivity peak. These findings demonstrate that domain walls

are active elements in controlling phonon dynamics, highlighting domain-wall engineering as a promising strategy for tuning thermal transport in complex oxides.

Publication 4 demonstrates the potential of VO_2 as a promising material for multiterminal electrothermal memristors, where resistive switching is governed by Joule heating induced IMT and the formation of metallic filaments. By combining electrical transport measurements with optical imaging, it is shown that multiple filaments can form between different terminal pairs and interact through current redistribution and thermal coupling. The application of a control voltage enables access to several distinct operational regimes, in which filament formation can be selectively promoted, suppressed, or stabilized, leading to different conduction pathways. These regimes highlight the key role of multiterminal geometry, where the distribution of currents among interchangeable terminals determines the filament configuration and switching dynamics, resulting in strongly hysteretic and history-dependent transport. This behavior establishes VO_2 multiterminal devices as reconfigurable network elements with built-in memory, offering strong potential for neuromorphic and in-memory computing applications.

2 Summary of publications and contributions

2.1 Publication 1: Laser-induced quenching of metastability at the Mott insulator to metal transition

This study demonstrates that focused laser irradiation can actively manipulate the phase-transition behavior of a strongly correlated material, specifically a V_2O_3 thin film, which is a prototypical system exhibiting a first-order Mott metal–insulator transition. Because the transition in V_2O_3 is governed by strong electron–electron correlations[51] and involves coexistence of metallic and insulating domains[91,94], this material provides an excellent platform for exploring how external stimuli such as light can influence phase dynamics and history-dependent behavior.

In the experiments, a continuous V_2O_3 thin film with a thickness of 300 nm is locally irradiated with a focused laser beam at various temperatures across the transition. Changes in phase morphology are imaged in real time using a multifunctional microscope that combines wide-field imaging with a scanning laser, enabling spatially resolved observation of both the MIT during heating and the IMT during cooling processes. Figure 2.1(b) illustrates the laser exposure and imaging process, while Fig. 2.1(a) shows the corresponding resistance versus temperature curve $R(T)$ that characterizes the hysteretic nature of the transition.

Although local heating by the laser would normally be expected to promote metallic domains[95,96], the experimental results reveal a more intricate behavior. As shown in Fig. 2.1(c), irradiation during heating indeed enhances the formation of metallic regions, consistent with thermal excitation.

However, during cooling, as shown in Fig. 2.1(d), the same irradiation unexpectedly promotes the formation of insulating domains, thereby accelerating the MIT. This asymmetry indicates that the influence of the

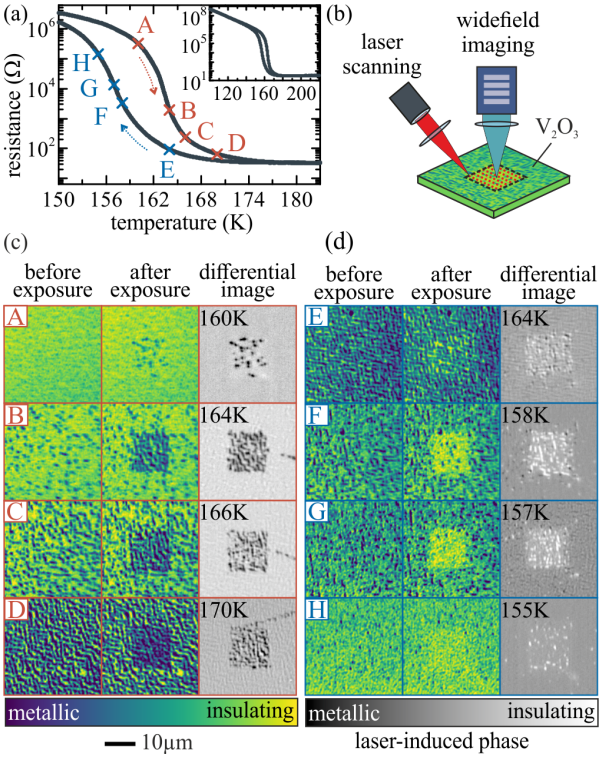


Figure 2.1: (a) Enlarged view of the phase-transition region in the $R(T)$ curve. The red and blue dashed arrows denote the heating and cooling branches, respectively, while the capital letters indicate the temperatures selected for laser irradiation. The inset displays the complete $R(T)$ curve of the V_2O_3 sample. (b) Schematic representation of the experimental setup. (c,d) Sequences of photomicrographs acquired during heating and cooling, showing the sample before and after laser scanning. In each panel, the third column presents the corresponding differential images obtained by comparing the states before and after laser exposure. Figure reprinted from appended publication 1. © 2024 American Physical Society.

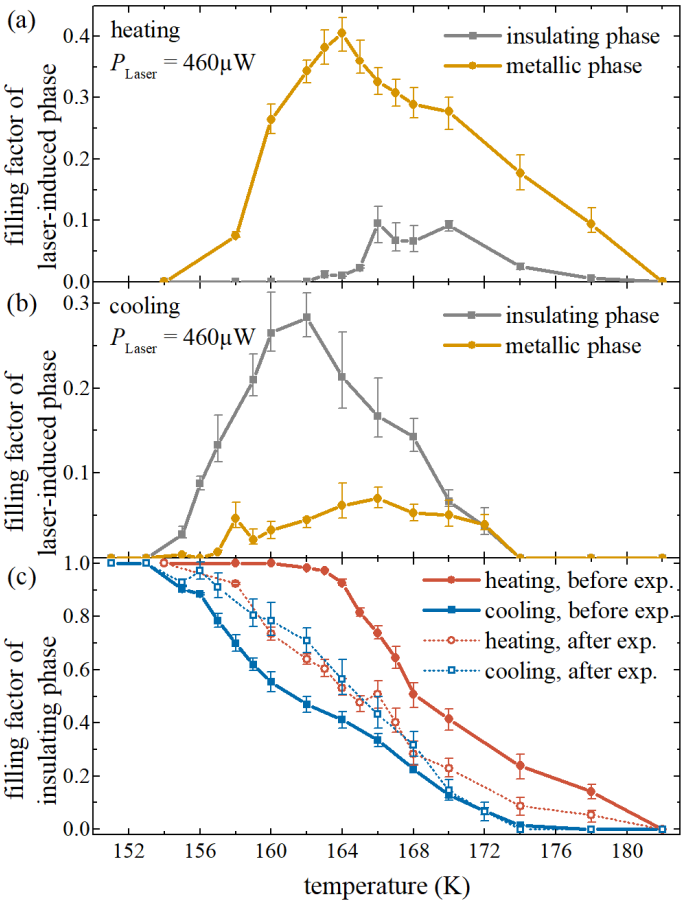


Figure 2.2: Evolution of the metallic and insulating phase fractions as a function of temperature under $460\,\mu$W **laser irradiation.** (a,b) Temperature-dependent filling factors during the heating and cooling branches, respectively. (c) Filling factor of the insulating phase recorded over a complete thermal cycle. Figure reprinted from appended publication 1. © 2024 American Physical Society.

laser extends beyond simple local heating and suggests that it affects the underlying transition dynamics and metastability.[97,98].

To quantify these effects, the *filling factor*, defined as the fraction of the surface occupied by a given phase, was analyzed. The metallic and insulating regions are distinguished by their brightness in the photomicrographs, as shown in Fig. 2.1. Figures 2.2(a) and (b) show that the filling factors exhibit a similar overall temperature dependence during heating and cooling. However, Fig. 2.2(c) reveals that laser irradiation significantly suppresses the hysteresis between the heating and cooling branches. After irradiation, the filling-factor curves for the two thermal paths nearly overlap, indicating that the film loses memory of its thermal history due to the laser perturbation.

This behavior can be understood in the context of first-order transition thermodynamics, where the system can occupy superheated or supercooled metastable states before completing the transition[99]. In V_2O_3, insulating regions may remain metastable above the equilibrium transition temperature during heating, while metallic regions can be supercooled below that temperature during cooling. Laser irradiation likely facilitates local relaxation out of these metastable states toward the thermodynamically stable phase appropriate for the given temperature, beyond any local heating effect. Complementary electrical transport measurements during controlled minor thermal cycles confirm that simple heating alone cannot account for the observed changes.

Finally, a phenomenological numerical model was employed that incorporates a laser-induced reduction of the energy barrier separating the metastable and equilibrium states, combined with Kirchhoff's laws and a first-order Landau free-energy framework. This model successfully reproduces the key experimental observations, including the evolution of the filling factor and the pronounced suppression of hysteresis under laser irradiation.

Contributions

This publication resulted from a collaborative effort involving the University of California San Diego, Université Paris-Saclay, and the Technion–Israel Institute of Technology in Haifa. The device fabrication was carried out by Y. Kalcheim, while the thermal minor-loop measurements were performed by A. Kronman. The numerical modeling was conducted by L. Fratino.

My contribution consisted of providing some ideas and performing the initial set of measurements that formed the basis of the reported results. Subsequently, T. Luibrand refined the experimental approach by improving the measurement setup and conducted the main part of the measurements. The imaging measurements were carried out under the supervision of S. Guénon. I also supported data analysis and paper writing. The preparation of the figures and the writing of the manuscript were carried out mainly by T. Luibrand and S. Guénon.

2.2 Publication 2: Nonvolatile multistate electrothermal resistive switching in a strongly correlated insulator thin-film device

This study investigates resistive switching devices, with a particular focus on nonvolatile devices capable of storing information persistently, analogous to synapses in biological neural networks. Among the candidate materials, strongly correlated insulating thin films have attracted significant attention due to their sharp temperature-dependent resistivity, which can trigger the formation of metallic filaments through electrothermal effects, typically resulting in volatile resistive switching[62,69,100,101]. However, in materials exhibiting pronounced hysteresis in the $R(T)$ curve, such as NNO, these filaments can remain stable, giving rise to nonvolatile behavior.

In this work, electrical and optical measurements were performed on a planar two-terminal NNO device using a wide-field optical microscope capable of simultaneous imaging and electrical transport measurements. Figure 2.3 presents the $R(T)$ curve obtained during thermal cycling, revealing a wide hysteresis that highlights the significant influence of thermal history on the electrical behavior of the device.

To characterize the switching behavior, electrical transport measurements were conducted at different temperatures within the hysteresis interval. Figure 2.4(a) illustrates the multistate nonvolatile switching process. The device was initially set to an insulating state by interrupting the thermal cycle at 167 K, followed by a series of current sweeps in which the maximum current was gradually increased from 1 mA to 2 mA in 25 μA increments. The resulting I–V curves show that, even near zero current, the resistance after each cycle remains lower than in the initial state, confirming persistent, nonvolatile switching. Furthermore, increasing the maximum current incrementally leads to higher conductance states, allowing multiple stable intermediate states to be created. While the experiment shown includes 40 sweeps, up to 100 intermediate states are achievable, demonstrating the potential for high-resolution analog information storage. These states remain stable as long as the temperature is maintained, and the pristine state can be fully restored by thermal cycling.

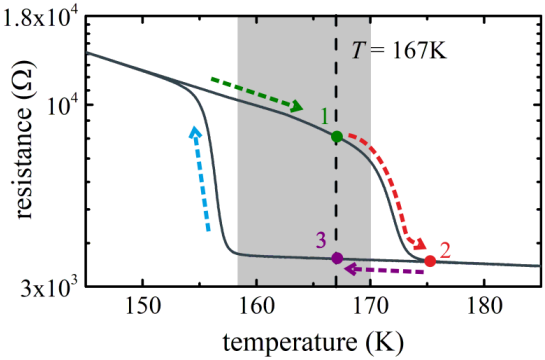


Figure 2.3: The $R(T)$ characteristic of the device was measured during thermal cycling under a constant current of $100\,\mu$A. The arrows show the progression of the temperature sweep. For subsequent electrical transport measurements, the temperature ramp was halted during the heating cycle at 167 K, as indicated by the vertical dashed line. Points 1, 2, and 3 correspond to the initial condition for the I–V measurements, the state under maximum applied current, and the zero-current condition during the down-sweep, respectively. Figure reprinted from appended publication 2. © 2025 American Physical Society.

Optical imaging of the device during switching further clarifies this process. Differential images reveal the formation of a metallic filament whose width increases as the device conductance grows across successive sweeps, as shown in Fig. 2.4(b). The dark region indicates the metallic channel.

The underlying mechanism of resistive switching is attributed to electrothermal instability. When the applied current exceeds a critical threshold, small variations in current density are amplified by localized Joule heating, which reduces the resistance of the nearby film. This effect concentrates the current into a narrow region, initiating resistive switching and forming a metallic filament between the electrodes. Most of the current then flows through the filament, generating intense localized heating that maintains the nearby material in the metallic phase above the IMT temperature.

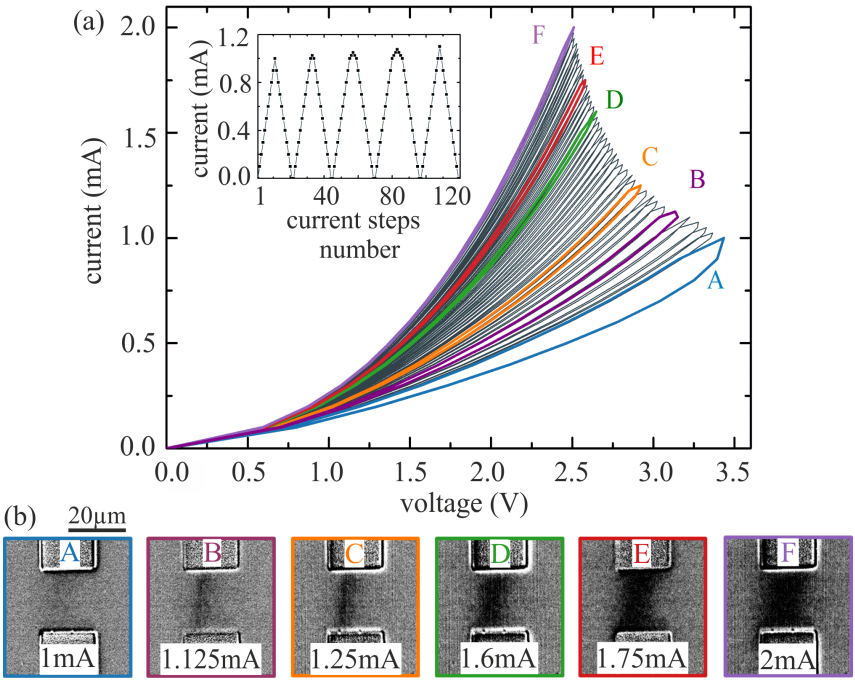


Figure 2.4: Nonvolatile multistate electrothermal resistive switching at $T = 167\,\mathrm{K}$. (a) Intermediate I–V loops obtained from triangular current sweeps. The inset shows the first five sweeps, in which the current is ramped from zero to $I_{\max}$ and back in $10\,\mu\mathrm{A}$ steps with a dwell time of 0.5 s. The maximum current, $I_{\max}$, is increased from 1.0 mA (loop A) to 2.0 mA (loop F) in increments of $25\,\mu\mathrm{A}$. (b) Differential images of the device recorded at $I = 0$ after completion of the corresponding I–V loops. Figure reprinted from appended publication 2. © 2025 American Physical Society.

Normally, the filament would widen or shrink depending on the current, but in NNO, thermal hysteresis traps the filament, allowing it to persist even when the current is reduced to zero.

Moreover, resistive switching was studied at various base temperatures after resetting the device. At lower temperatures (160–166 K), the first current sweep produced abrupt switching during the up-sweep, resulting in broad metallic filaments that spanned most of the electrode gap. This filamentary state was retained in the subsequent sweeps, whose I–V loops closely followed the down-sweep branch of the first loop, confirming the nonvolatile nature of the switching. At higher temperatures (165–167 K), switching during the first up-sweep was more gradual, and the filaments appeared narrower. These differences arise from electrothermal effects: at lower base temperatures, a larger amount of Joule heating is required to locally drive the NNO film into the metallic phase. In contrast, at higher base temperatures, enhanced thermal coupling to the electrodes and/or the nucleation of isolated metallic domains can redistribute the current over a larger device area. As a result, the transition proceeds more gradually and gives rise to narrower metallic filaments.

Contributions

This study was carried out as a collaboration between the University of Tübingen and the Max Planck Institute for Solid State Research in Stuttgart. The sample was provided by M. Hepting. C. Schmid contributed to the lithography and device structuring, while T. Luibrand developed a LabVIEW program for minor-loop measurements.

My contribution to this work included the design of the device layout, the execution of all electrical and optical measurements, and the analysis of the results. All figures presented in this work were prepared by me. The measurements were supervised by S. Guénon. In addition, I actively participated in scientific discussions and contributed to the development of the manuscript, which was written by S. Guénon.

2.3 Publication 3: Domain-wall-driven anomaly in hydrodynamic phonon transport in $SrTiO_3$

The paper explores how intrinsic structural features affect heat transport beyond the conventional diffusive regime. In crystalline solids, heat is carried by phonons, which typically scatter randomly[102,103]; however, in very pure materials, they can exhibit hydrodynamic phonon transport, where momentum-conserving interactions lead to collective, fluid-like behavior and enhanced thermal conductivity[77,104,105]. Studies on materials such as graphite[106] and black phosphorus[107] show that reducing sample size increases boundary scattering and suppresses this regime. These findings are important for thermal management in nanoelectronics and for designing advanced phononic devices.

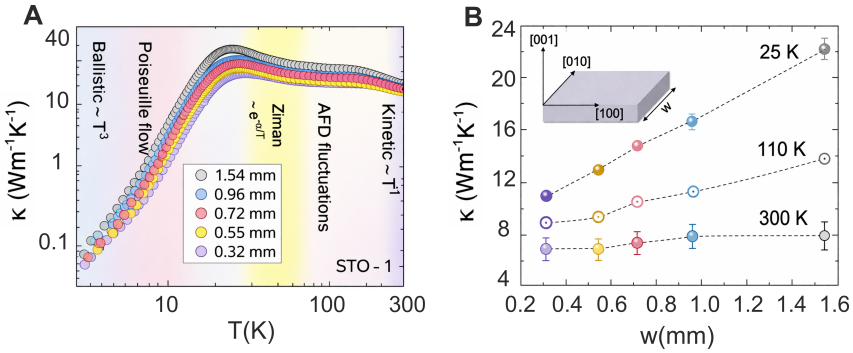


Figure 2.5: (A) Thermal conductivity of STO versus temperature for samples of different widths on a log–log scale. Shaded regions indicate the dominant phonon transport regimes: ballistic (blue), Poiseuille (red), Ziman (yellow), AFD fluctuations (orange), and kinetic (purple). (B) Thermal conductivity of STO at 300, 110, and 25 K as a function of sample width w. Inset: Schematic of STO single crystal with crystallographic orientation. Error bars indicate the uncertainty in the measured thermal conductivity κ. Figure Reprinted from appended publication 3, with permission from Elsevier.

STO provides an ideal platform for studying phonon hydrodynamics because of its high crystalline quality and its low-temperature cubic-to-tetragonal phase transition, which generates ferroelastic domains separated by domain walls. These domain walls interact with phonons and play a crucial role in determining the thermal transport behavior. Thermal conductivity measurements, shown in Fig. 2.5(A), reveal signatures of hydrodynamic phonon transport, including a pronounced peak and deviations from diffusive transport, indicating collective phonon flow. As shown in Fig. 2.5(B), the thermal conductivity is nearly independent of sample size in the cubic phase above 105 K, whereas a strong size dependence emerges in the tetragonal phase, particularly near 25 K, reflecting enhanced boundary scattering. This behavior is directly linked to the formation and evolution of domain structures, as shown in Fig. 2.6, where the temperature-dependent changes in domain size and density establish a clear connection between microscopic lattice features and macroscopic thermal transport. The photomicrographs show that reducing the sample width, w, increases the areal density of FDWs and concomitantly decreases the average domain-wall spacing, Λ. Furthermore, studies on microscale STO show that FDWs formed during the AFD transition act as internal boundaries, reducing the phonon mean free path from the sample size to the micron-scale domain size[77].

Furthermore, the width-dependent evolution of phonon transport in STO is analyzed by separating the thermal conductivity into intrinsic phonon contributions and thermal diffusivity, as shown in Fig. 2.7. Specific-heat measurements confirm the expected phononic behavior, while the extracted diffusivity reveals a hallmark of phonon Poiseuille flow: a nonmonotonic temperature dependence with a distinct Knudsen minimum followed by a maximum, indicating the crossover from ballistic to hydrodynamic transport. As shown in Fig. 2.7, decreasing the sample width progressively suppresses this nonmonotonic behavior and eventually eliminates it, while the Knudsen minimum shifts to higher temperatures, signaling the breakdown of hydrodynamic flow. Since the sample dimensions are much larger than the phonon mean free path, conventional boundary scattering cannot explain this effect.

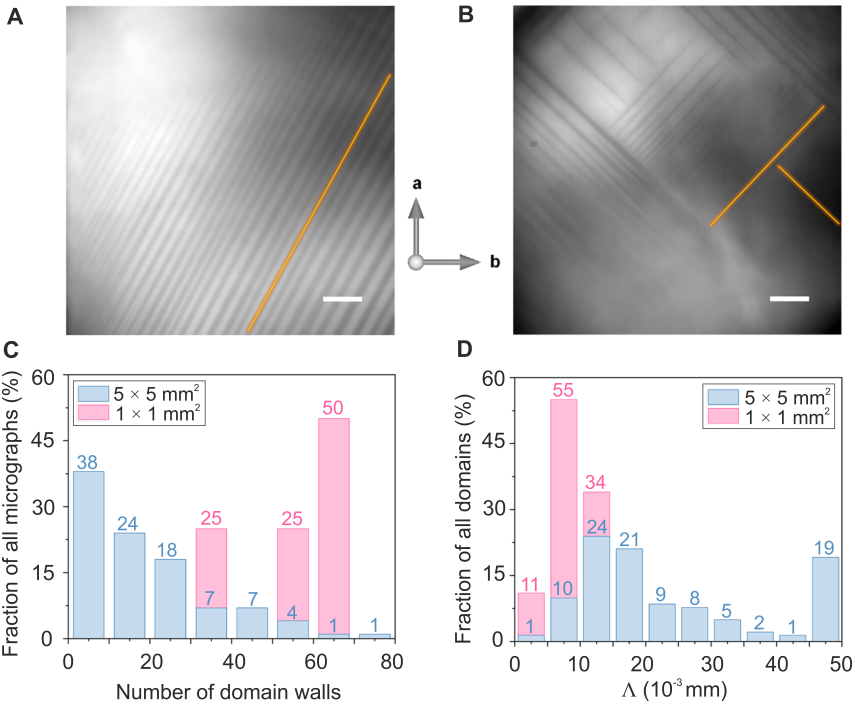


Figure 2.6: (A,B) Polarized-light micrographs of a (001)-oriented STO single crystal before and after mechanical polishing. Panel (A) shows the original $5 \times 5 \times 0.5$ mm^3 sample, while panel (B) shows the crystal after its lateral dimensions were reduced to 1×1 mm^2. Images were acquired at 50 K, below the AFD transition, with [100] (a axis) vertical and [010] (b axis) horizontal. FDWs appear as dark-gray stripes, with selected walls highlighted in yellow. Scale bar: 50 μm. (C) Distribution of FDW counts before and after polishing, identified within each 0.5×0.5 mm^2 micrographs. (D) Distribution of the spacing between neighboring FDWs before and after polishing. Figure reprinted from appended publication 3, with permission from Elsevier.

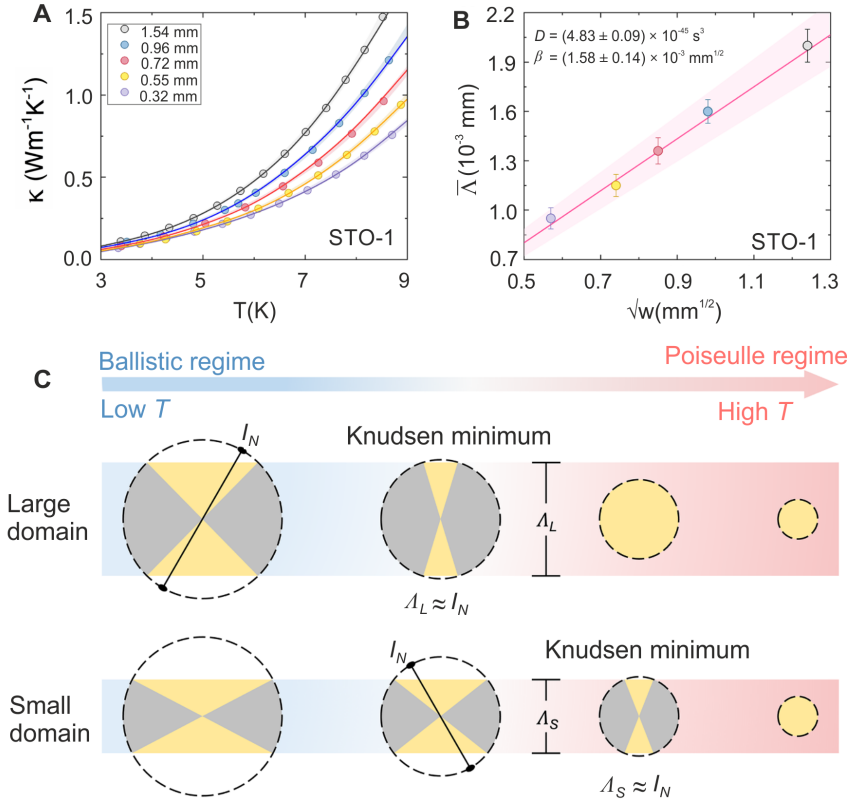


Figure 2.7: (A) Width-dependent thermal conductivity of STO measured between 3 and 9 K. The shaded regions indicate the experimental uncertainty in κ, and the solid lines correspond to fits obtained from the model. (B) Dependence of the extracted domain-wall spacing, Λ, on $\sqrt{w}$. The solid pink line shows the result of a least-squares linear regression, while the surrounding shaded region represents the corresponding confidence interval. The error bars indicate the estimated uncertainty in Λ. (C) Conceptual representation of the Knudsen minimum. Figure reprinted from appended publication 3, with permission from Elsevier.

Additional control experiments rule out impurities[108], oxygen vacancies[109], and surface damage[110], confirming that the observed size dependence originates from intrinsic scattering at FDWs formed below the structural phase transition.

To further investigate thermal transport in STO samples, a model based on first-principles calculations has been developed[111]. A comparison between experimental data and theoretical predictions for both diffusive and hydrodynamic regimes reveals clear deviations in the temperature range where domain walls are most prominent. Instead of following ideal hydrodynamic scaling, the thermal conductivity is suppressed or modified, indicating anomalous behavior. This demonstrates that the collective flow of phonons is disrupted by additional scattering mechanisms associated with the domain structure.

Overall, systematically reducing the width w of STO crystals— while keeping other dimensions constant— reveals a pronounced and unexpected size dependence even when w remains much larger than the phonon mean free path. As w decreases, the thermal conductivity peak is progressively suppressed, and the super-T^3 enhancement associated with phonon Poiseuille flow is weakened, eventually approaching and deviating below the T^3 behavior. In parallel, the thermal diffusivity evolves from a non-monotonic to a monotonic temperature dependence, with the Knudsen minimum shifting to higher temperatures, signaling the gradual breakdown of hydrodynamic transport. First-principles analysis further reveals that the domain size decreases with w following a $\sqrt{w}$ scaling, consistent with increased FDW density. These findings establish macroscopic geometry, mediated by domain walls, as a key parameter for tuning phonon hydrodynamics and thermal transport.

Contributions

This work was carried out in collaboration with the University of California, Riverside, the University of Pittsburgh, and the University of Texas, USA. The conceptual framework of the study was developed by S. Guo, who also performed the thermal conductivity measurements, analyzed the data, and prepared the figures and manuscript. J. Han contributed by developing a numerical model to support the interpretation of the experimental results. My main contribution to this work consisted of performing optical imaging on different samples and the subsequent analysis of the acquired data, conducted under the supervision of S. Guénon. I also provided some ideas and supported paper writing.

2.4 Publication 4: History-dependent filament configuration in multiterminal electrothermal memristors

This work investigates multiterminal electrothermal memristors (ETMs) based on vanadium dioxide, with emphasis on the formation, evolution, and collapse of electrically induced metallic filaments in a history-dependent manner. ETMs exploit the pronounced temperature-driven IMT in VO_2, where Joule heating induces abrupt and hysteretic resistance switching. While filament formation is well established in two-terminal devices[112–116], extending this concept to three-terminal geometries reveals reconfigurable and controllable filament networks.

The VO_2 thin-film device was fabricated epitaxially with patterned Ti/Au electrodes and characterized using simultaneous electrical transport measurements and wide-field polarization microscopy. This technique enables direct imaging of insulating and metallic regions with submicron resolution. By applying voltages between different terminal pairs, current redistribution can be monitored and the formation of conductive filaments between specific electrodes can be tracked under varying bias conditions.

In the two-terminal limit (Fig. 2.8(a) and (c)), the device behaves as a conventional VO_2 memristor: a single metallic filament forms abruptly at a threshold voltage and collapses at a lower return voltage, resulting in a hysteretic current–voltage response. The filament width increases with compliance current, consistent with established VO_2 switching behavior[117].

When the third terminal is engaged (Fig. 2.8(b) and (d)), the behavior changes fundamentally. In this regime (I), the current divides into multiple paths, enabling the simultaneous formation of two filaments (e.g., A–G and A–B). These filaments nucleate at comparable switching thresholds and collapse together, but differ in strength due to asymmetries in contact resistance and current distribution. This demonstrates that filament formation is not fixed, but strongly governed by current distribution across the terminals.

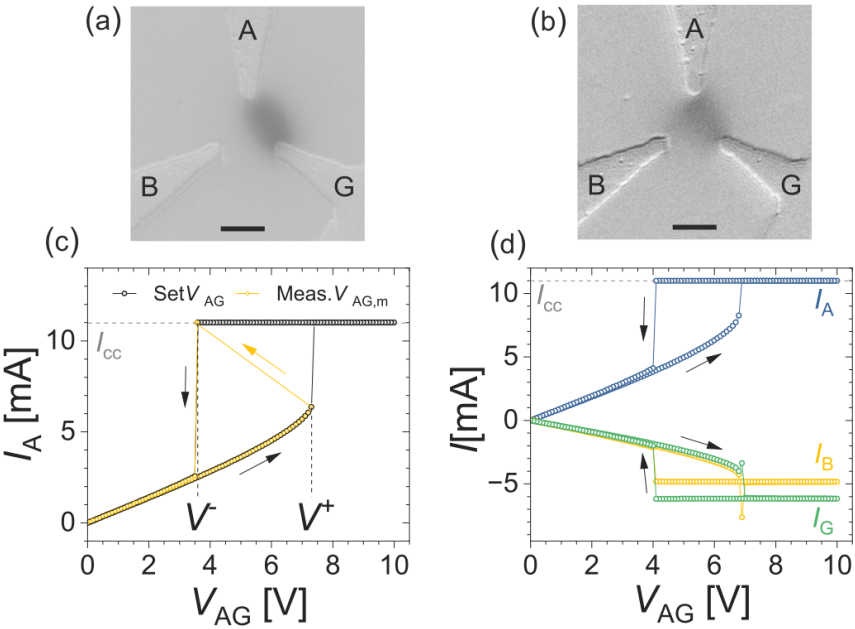


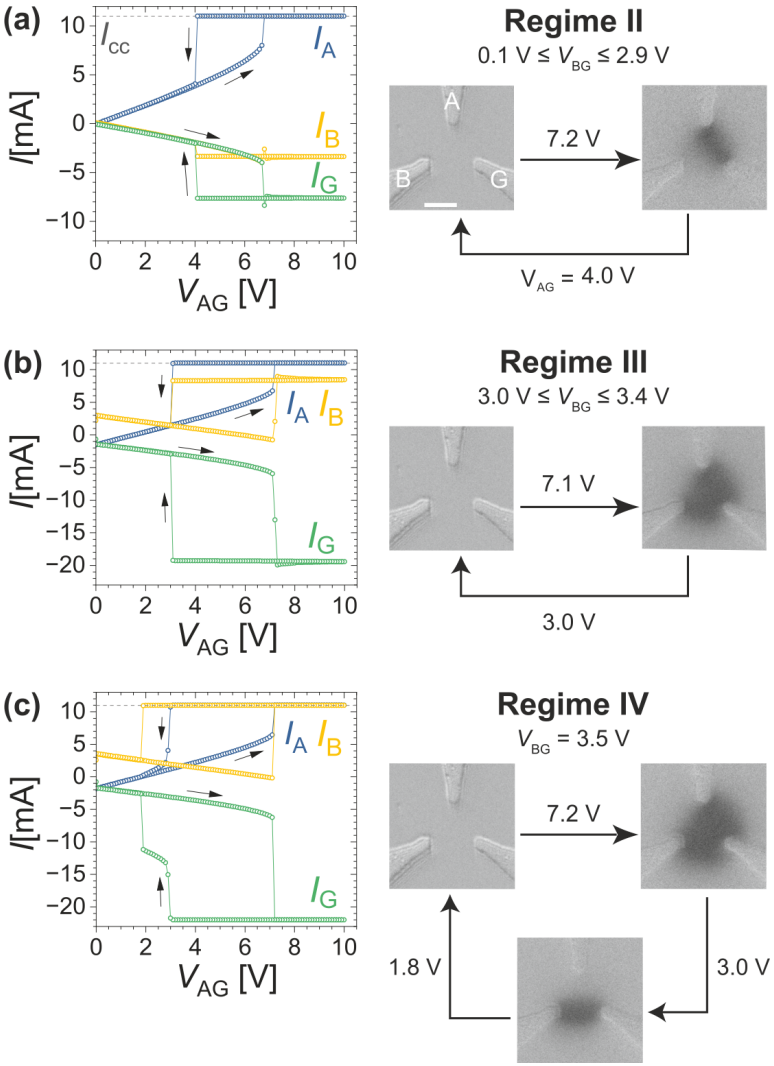
Figure 2.8: (a) WFPM differential image of a single metallic filament (dark region) at $V_{AG} = 10\,\mathrm{V}$ and $I_{cc} = 11\,\mathrm{mA}$; terminal B is unconnected. (b) WFPM image of multiple metallic filaments at $V_{AG} = 10\,\mathrm{V}$, $V_{BG} = 0\,\mathrm{V}$, and $I_{cc} = 11\,\mathrm{mA}$, with all terminals connected. (c) Current at terminal A (I_A) versus applied V_{AG} (black) and measured $V_{AG,m}$ (gold), corresponding to (a). (d) Currents I_A, I_B, and inferred $I_G = -I_A - I_B$ versus V_{AG} for the configuration in (b). Figure reprinted from appended publication 4. © 2026 AIP Publishing.

A key result is that applying a control voltage (V_{BG}) enables systematic tuning of filament formation, as shown in Fig. 2.9 Even small variations in V_{BG} modify the local electric field and Joule heating, thereby determining which electrode pairs support filament growth. Six distinct operational regimes are identified, ranging from single-filament formation

to coupled multi-filament states, as well as configurations where filaments extend across multiple terminals or persist independently. As V_{BG} increases, the system transitions smoothly between these regimes. These transitions are continuous, reproducible, and hysteretic, indicating that the device retains memory of its previous electrical state. The formation of each filament alters the local current distribution and thereby influences where subsequent filaments emerge, producing a conductive network that depends on the preceding electrical history.

The study further demonstrates that the three terminals are functionally interchangeable, as each can serve as an input, output, or control terminal depending on the applied bias conditions. This behavior contrasts with that of conventional transistors and highlights the potential of the device as a reconfigurable computing element. Moreover, the filament configuration and the corresponding current–voltage characteristics can be continuously tuned through the control voltage V_{BG}, thereby modifying the hysteresis loops and switching thresholds. Finally, scaling considerations indicate that reducing device dimensions decreases the filament volume, thereby lowering switching energy and latency. Engineering thermal coupling and device geometry is therefore essential for optimizing performance and enabling dense multiterminal networks.

Overall, the paper demonstrates that VO_2-based multiterminal ETMs exhibit controllable, history-dependent multi-filament switching governed by terminal biasing. This enables dynamically reconfigurable conductive pathways, making these devices promising candidates for future neuromorphic and reconfigurable computing systems.


(a)
I[mA]
V_{AG} [V]
I_{CC}
I_A
I_B
I_G
Regime II
0.1 V ≤ V_{BG} ≤ 2.9 V
A
B
G
7.2 V
V_{AG} = 4.0 V
(b)
Regime III
3.0 V ≤ V_{BG} ≤ 3.4 V
7.1 V
3.0 V
(c)
Regime IV
V_{BG} = 3.5 V
7.2 V
1.8 V
3.0 V

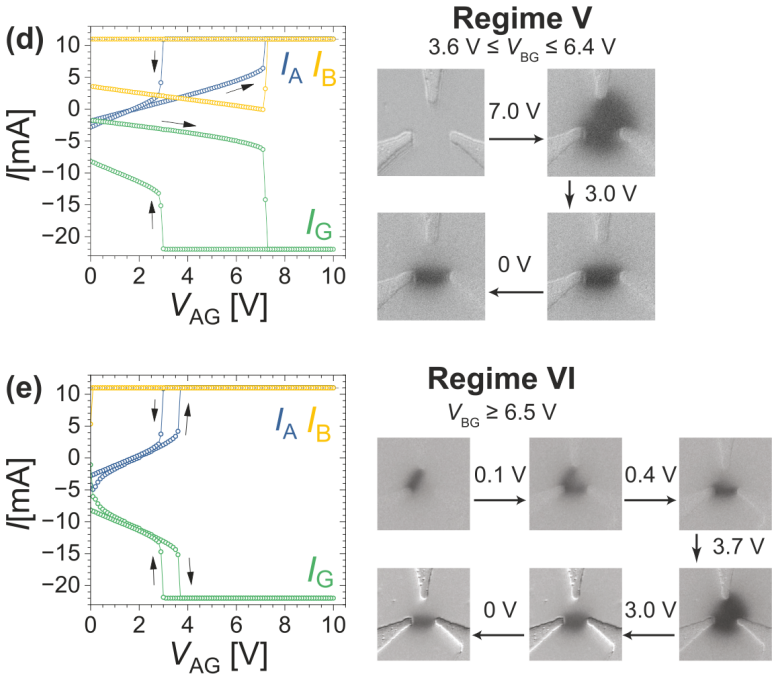


Figure 2.9: Voltage-dependent filament configuration. The currents I_A, I_B, and I_G, flowing into terminals A, B, and G, respectively, are shown as functions of the set voltage V_{AG} for a current compliance of $I_{cc} = 11\,\text{mA}$. The corresponding WFPM photomicrographs were acquired during the same voltage sweeps. Arrows mark transitions at selected values of V_{AG}, while the associated transport regimes are discussed in the main text. The data were recorded at the lower boundary of each regime for V_{BG} = (a) 0.1 V, (b) 3.0 V, (c) 3.5 V, (d) 3.6 V, and (e) 6.5 V. Scale bars: 10 μm. Figure reprinted from appended publication 4. © 2026 AIP Publishing.

Contributions

This work was carried out in collaboration with the University of Twente. The central concept of the study was developed by S. Smink. He and his colleagues were responsible for the fabrication and structuring of the sample and the initial electrical transport measurements. My contribution to this work was to perform optical imaging simultaneously with electrical transport measurements. All experimental data shown in the paper were acquired at the University of Tübingen. I further analyzed the optical images and prepared them for publication. The figures were generated by S. Smink, who also led the writing of the manuscript. In addition, I actively contributed to the development of the manuscript through discussions and feedback.

3 Conclusion

This thesis demonstrates the emergent properties and technological potential of transition metal oxides investigated by combining electrical transport measurements with advanced optical microscopy techniques. These materials exhibit a rich interplay between electronic, structural, thermal, and lattice degrees of freedom, leading to emergent phenomena such as metal–insulator transitions, phase coexistence, nonlinear transport, filament formation, and domain-mediated heat transport. Owing to these unique properties, transition metal oxides have attracted considerable attention as promising candidates for future electronic technologies beyond conventional semiconductor-based devices, which are increasingly challenged by limitations associated with device scaling, increasing power consumption, heat dissipation, and latency in information processing and storage.

In this context, oxide materials offer alternative concepts for electronic functionality based on intrinsic phase-transition physics rather than conventional charge-carrier control. In particular, nickelates and vanadates provide novel mechanisms for electrically driven switching and multistate memory behavior, while titanates enable controllable thermal transport through ferroelastic domain engineering. Therefore, understanding the microscopic mechanisms governing these functionalities is essential for the development of future oxide electronics and energy-efficient computing technologies.

A central aspect of this thesis is the use of multifunctional optical microscopy capable of simultaneously imaging devices while electrical transport measurements are performed. This integration enabled direct spatial visualization of microscopic processes such as conductive filament formation, phase coexistence, and ferroelastic domain evolution. These experimental approaches provide an important platform for correlating local microscopic behavior with macroscopic transport properties and allow direct

investigation of nonequilibrium phenomena in strongly correlated materials.

The first part of this thesis focused on laser-induced perturbation of correlated electronic states in V_2O_3, a prototypical Mott material exhibiting a first-order IMT. The results presented in **Publication 1** show that optical excitation can quench metastable phases and trigger transitions between insulating and metallic states during thermal cycling. These observations provide direct insight into the metastable nature of the first-order Mott transition in V_2O_3 and demonstrate that laser irradiation can drive supercooled and superheated states toward thermodynamic equilibrium. The ability to modify the stability of metastable phases by laser irradiation further demonstrates that optical excitation can be used as a controlled external perturbation to manipulate the phase transition dynamics in V_2O_3 without direct electrical biasing. Thus, such optically induced control of phase transitions represents a promising approach for future switching concepts and multifunctional oxide-electronic devices.

The second part of this thesis, published as **Publication 2**, focused on nonvolatile resistive switching in $NdNiO_3$ thin films. In these two-terminal devices, Joule-heating-induced electrothermal instability leads to the formation of stable metallic filaments within the insulating matrix. Due to the hysteretic nature of the metal–insulator transition, the filamentary states remain stable after reducing the applied current, resulting in reproducible nonvolatile resistance states. More than one hundred distinct resistance levels were achieved, demonstrating the potential of nickelates as memristive devices for analog memory and neuromorphic computing applications. In contrast to conventional resistive switching mechanisms based on ionic migration, the switching behavior in $NdNiO_3$ originates from intrinsic phase-transition physics, offering the prospect of enhanced endurance and improved energy efficiency.

Another important aspect of this thesis, discussed in **Publication 3**, was the investigation of ferroelastic domain walls in $SrTiO_3$ and their influence on heat transport. Using polarized optical microscopy combined with thermal transport measurements, the spatial configuration of ferroelastic domains was directly correlated with thermal conductivity behavior. The results showed that increasing the domain-wall density suppresses

collective phonon transport by introducing additional phonon scattering centers. Consequently, the thermal conductivity can be tuned through the domain-wall configuration and sample geometry. These findings establish ferroelastic domain walls as active elements for controlling heat transport in complex oxides and demonstrate the potential of domain engineering for future thermal-management technologies and phononic devices.

The final part of this thesis addressed electrically driven switching behavior in multiterminal VO_2 devices. As presented in **Publication 4**, simultaneous optical imaging and transport measurements revealed the formation and evolution of conductive filamentary pathways during operation. In multiterminal geometries, the filament configuration could be manipulated through the applied bias conditions, enabling controllable current pathways inside the device. These results demonstrate how correlated oxides can provide functionalities beyond conventional two-terminal switching devices. In particular, multiterminal architectures based on VO_2 offer promising opportunities for transistor-like operation, adaptive electronics, and unconventional computing concepts based on tunable phase coexistence and nonlinear transport.

Overall, this thesis demonstrates how multifunctional optical microscopy enables direct observation of microscopic processes governing the behavior of transition metel oxide devices during operation. The combination of spatial imaging with electrical and thermal transport characterization provides valuable insight into phase coexistence, filament dynamics, and domain-wall-mediated phenomena in strongly correlated materials. The results further highlight the broad technological potential of correlated oxides for future electronic, memory, neuromorphic, and thermal-management applications beyond the limits of conventional semiconductor technologies.

Declaration on the use of generative AI

I declare that I used artificial intelligence tools, namely ChatGPT by OpenAI and Gemini by Google, during the preparation of this thesis. These tools were used exclusively to support language editing, grammar correction, rephrasing, translation, and improvement of text clarity.

Bibliography

[1] G. E. Moore, "Cramming more components onto integrated circuits", *Electronics* 38 (1965), pp. 114–117.

[2] S. Das, A. Chen, and M. Marinella, "Beyond CMOS", *IEEE International Roadmap for Devices and Systems Outbriefs Conference*, (2021), pp. 1–129.

[3] R. H. Dennard, F. H. Gaensslen, H. N. Yu, V. L. Rideout, E. Bassous, and A. R. LeBlanc, "Design of ion-implanted MOSFET's with very small physical dimensions", *IEEE Journal of Solid-State Circuits* 9 (1974), pp. 256–268.

[4] D. A. Muller, T. Sorsch, S. Moccio, F. H. Baumann, K. Evans-Lutterodt, and G. Timp, "The electronic structure at the atomic scale of ultrathin gate oxides", *Nature* 399 (1999), pp. 758–761.

[5] D.J. Frank, R.H. Dennard, E. Nowak, P.M. Solomon, Y. Taur, and Hon-Sum Philip Wong, "Device scaling limits of Si MOSFETs and their application dependencies", *Proceedings of the IEEE* 89 (2001), pp. 259–288.

[6] S. H. Lo, D.A. Buchanan, Y. Taur, and W. Wang, "Quantum-mechanical modeling of electron tunneling current from the inversion layer of ultra-thin-oxide nMOSFET's", *IEEE Electron Device Letters* 18 (1997), pp. 209–211.

[7] A. Schenk and G. Heiser, "Modeling and simulation of tunneling through ultra-thin gate dielectrics", *Journal of Applied Physics* 81 (1997), pp. 7900–7908.

[8] S. Borkar, "Design challenges of technology scaling", *IEEE Micro* 19 (1999), pp. 23–29.

[9] M. M. Waldrop, "The chips are down for Moore's law", *Nature News* 530 (2016), pp. 144–147.

[10] P. S. Peercy, "The drive to miniaturization", *Nature* 406 (2000), pp. 1023–1026.

[11] S. Petrenko, "Limitations of von Neumann architecture. In: big data technologies for monitoring of computer security: A case study of the Russian Federation", *Springer International Publishing*, (2018), pp. 115–173.

[12] J. Mannhart and D. G. Schlom, "Oxide interfaces—An opportunity for electronics", *Science* 327 (2010), pp. 1607–1611.

[13] P. Zubko, S. Gariglio, M. Gabay, P. Ghosez, and J. M. Triscone, "Interface physics in complex oxide heterostructures", *Annual Review of Condensed Matter Physics* 2 (2011), pp. 141–165.

[14] J. H. Ngai, F. J. Walker, and C. H. Ahn, "Correlated oxide physics and electronics", *Annual Review of Materials Research* 44 (2014), pp. 1–17.

[15] Y. Zhou and S. Ramanathan, "Mott memory and neuromorphic devices", *Proceedings of the IEEE* 103 (2015), pp. 1289–1310.

[16] M. Imada, A. Fujimori, and Y. Tokura, "Metal-insulator transitions", *Reviews of Modern Physics* 70 (1998), pp. 1039–1263.

[17] Y. Tokura and N. Nagaosa, "Orbital physics in transition-metal oxides", *Science* 288 (2000), pp. 462–468.

[18] E. Dagotto, "Complexity in strongly correlated electronic systems", *Science* 309 (2005), pp. 257–262.

[19] Y. Tokura, "Correlated-electron physics in transition-metal oxides", *Physics Today* 56 (2003), pp. 50–55.

[20] Y. Zhou and S. Ramanathan, "Correlated electron materials and field effect transistors for logic: A review", *Critical Reviews in Solid State and Materials Sciences* 38 (2013), pp. 286–317.

[21] J. L. M. van Mechelen, D. van der Marel, C. Grimaldi, A. B. Kuzmenko, N. P. Armitage, N. Reyren, H. Hagemann, and I. I. Mazin, "Electron-phonon interaction and charge carrier mass enhancement in $SrTiO_3$", *Physical Review Letters* 100 (2008), p. 226403.

[22] A. Lanzara, P. V. Bogdanov, X. J. Zhou, S. A. Kellar, D. L. Feng, E. D. Lu, T. Yoshida, H. Eisaki, A. Fujimori, K. Kishio, J.-I. Shimoyama, T. Noda, S. Uchida, Z. Hussain, and Z.-X. Shen, "Evidence for ubiquitous strong electron–phonon coupling in high-temperature superconductors", *Nature* 412 (2001), pp. 510–514.

[23] A. J. Millis, "Lattice effects in magnetoresistive manganese perovskites", *Nature* 392 (1998), pp. 147–150.

[24] M. I. Díaz, J. E. Han, and C. Aron, "Electrically driven insulator-to-metal transition in a correlated insulator: Electronic mechanism and thermal description", *Physical Review B* 107 (2023), p. 195148.

[25] J. Jeong, N. Aetukuri, T. Graf, T. D. Schladt, M. G. Samant, and S. S. P. Parkin, "Suppression of metal-insulator transition in VO_2 by electric field–induced oxygen vacancy formation", *Science* 339 (2013), pp. 1402–1405.

[26] J. Liu, M. Kareev, B. Gray, J. W. Kim, P. Ryan, B. Dabrowski, J. W. Freeland, and J. Chakhalian, "Strain-mediated metal-insulator transition in epitaxial ultrathin films of $NdNiO_3$", *Applied Physics Letters* 96 (2010).

[27] S. Middey, J. Chakhalian, P. Mahadevan, J.W. Freeland, A.J. Millis, and D.D. Sarma, "Physics of ultrathin films and heterostructures of rare-earth nickelates", *Annual Review of Materials Research* 46 (2016), pp. 305–334.

[28] P. Homm, M. Menghini, J. W. Seo, S. Peters, and J. P. Locquet, "Room temperature Mott metal–insulator transition in V_2O_3 compounds induced via strain-engineering", *APL Materials* 9 (2021).

[29] J. K. Li, C. Ma, K. J. Jin, C. Ge, L. Gu, X. He, W. J. Zhou, Q. H. Zhang, H. B. Lu, and G. Z. Yang, "Temperature-dependent resistance switching in $SrTiO_3$", *Applied Physics Letters* 108 (2016).

[30] R. Waser and M. Aono, "Nanoionics-based resistive switching memories", *Nature Materials* 6 (2007), pp. 833–840.

[31] J. J. Yang, D. B. Strukov, and D. R. Stewart, "Memristive devices for computing", *Nature Nanotechnology* 8 (2012), pp. 13–24.

[32] D. Ielmini and H. S. P. Wong, "In-memory computing with resistive switching devices", *Nature Electronics* 1 (2018), pp. 333–343.

[33] J. Shi, S. D. Ha, Y. Zhou, F. Schoofs, and S. Ramanathan, "A correlated nickelate synaptic transistor", *Nature Communications* 4 (2013), p. 2676.

[34] N. F. Mott, "Review lecture: Metal–insulator transitions", *Proceedings of the Royal Society of London. A. Mathematical and Physical Sciences* 382 (1982), pp. 1–24.

[35] R. F. Milligan and G. A. Thomas, "The metal-insulator transition", *Annual review of physical chemistry* 36 (1985), pp. 139–158.

[36] S. Doniach, "The insulator-metal transition", *Advances in Physics* 18 (1969), pp. 819–848.

[37] F. J. Morin, "Oxides which show a metal-to-insulator transition at the neel temperature", *Physical Review Letters* 3 (1959), pp. 34–36.

[38] J. B. Goodenough, "The two components of the crystallographic transition in VO_2", *Journal of Solid State Chemistry* 3 (1971), pp. 490–500.

[39] J. Hubbard, "Electron correlations in narrow energy bands", *Proceedings of the Royal Society of London. Series A. Mathematical and Physical Sciences* 276 (1963), pp. 238–257.

[40] N. F. Mott, "The basis of the electron theory of metals, with special reference to the transition metals", *Proceedings of the Physical Society. Section A* 62 (1949), pp. 416–422.

[41] J. Zaanen, G. A. Sawatzky, and J. W. Allen, "Band gaps and electronic structure of transition-metal compounds", *Physical Review Letters* 55 (1985), pp. 418–421.

[42] J. P. Julien and R. C. Albers, "Extended recursion in operator space (EROS), a new impurity solver for the single impurity Anderson model", *arXiv:0810.3302* (2008).

[43] G. Kotliar and D. Vollhardt, "Strongly correlated materials: Insights from dynamical mean-field theory", *Physics Today* 57 (2004), pp. 53–59.

[44] A. Georges, G. Kotliar, W. Krauth, and M. J. Rozenberg, "Dynamical mean-field theory of strongly correlated fermion systems and the limit of infinite dimensions", *Reviews of Modern Physics* 68 (1996), pp. 13–125.

[45] M. Ganahl, M. Aichhorn, H. G. Evertz, P. Thunström, K. Held, and F. Verstraete, "Efficient DMFT impurity solver using real-time dynamics with matrix product states", *Physical Review B* 92 (2015), p. 155132.

[46] G. Kotliar, S. Y. Savrasov, K. Haule, V. S. Oudovenko, O. Parcollet, and C. A. Marianetti, "Electronic structure calculations with dynamical mean-field theory", *Reviews of Modern Physics* 78 (2006), pp. 865–951.

[47] A. Zylbersztejn and N. F. Mott, "Metal-insulator transition in vanadium dioxide", *Physical Review B* 11 (1975), pp. 4383–4395.

[48] R. M. Wentzcovitch, W. W. Schulz, and P. B. Allen, "VO_2: Peierls or Mott-Hubbard? A view from band theory", *Physical Review Letters* 72 (1994), pp. 3389–3392.

[49] Y. Oka, S. Sato, T. Yao, and N. Yamamoto, "Crystal structures and transition mechanism of VO_2 (A)", *Journal of Solid State Chemistry* 141 (1998), pp. 594–598.

[50] M. M. Qazilbash, M. Brehm, B. G. Chae, P. C. Ho, G. O. Andreev, B. J. Kim, S. J. Yun, A. V. Balatsky, M. B. Maple, F. Keilmann, and H. T. Kim, "Mott transition in VO_2 revealed by infrared spectroscopy and nano-imaging", *Science* 318 (2007), pp. 1750–1753.

[51] D. B. McWhan, A. Menth, J. P. Remeika, W. F. Brinkman, and T. M. Rice, "Metal-insulator transitions in pure and doped V_2O_3", *Physical Review B* 7 (1973), pp. 1920–1931.

[52] P. Limelette, A. Georges, D. Jérome, P. Wzietek, P. Metcalf, and J. M. Honig, "Universality and critical behavior at the Mott transition", *Science* 302 (2003), pp. 89–92.

[53] M. Caputo, J. Jandke, E. Cappelli, S. K. Chaluvadi, E. Bonini Guedes, M. Naamneh, G. Vinai, J. Fujii, P. Torelli, I. Vobornik, A. Goldoni, P. Orgiani, F. Baumberger, M. Radovic, and G. Panaccione, "Metal to insulator transition at the surface of V_2O_3 thin films: An in-situ view", *Applied Surface Science* 574 (2022), p. 151608.

[54] A. Kumar, "A review on the physics of phase transition in vanadium-sesquioxide thin-films and their synchrotron-based electronic structures", *Journal of Applied Physics* 138 (2025).

[55] J. Torrance, P. Lacorre, A. Nazzal, E. Ansaldo, and C. Niedermayer, "Systematic study of insulator-metal transitions in perovskites $RNiO_3$ (R = Pr, Nd, Sm, Eu) due to closing of charge-transfer gap", *Physical Review B* 45 (1992), pp. 8209–8212.

[56] M. L. Medarde, "Structural, magnetic and electronic properties of perovskites (R = rare earth)", *Journal of Physics: Condensed Matter* 9 (1997), pp. 1679–1707.

[57] G. Catalan, "Progress in perovskite nickelate research", *Phase Transitions* 81 (2008), pp. 729–749.

[58] A. Crunteanu, J. Givernaud, J. Leroy, D. Mardivirin, C. Champeaux, J. C. Orlianges, A. Catherinot, and P. Blondy, "Voltage- and current-activated metal–insulator transition in VO_2-based electrical switches: a lifetime operation analysis", *Science and Technology of Advanced Materials* 11 (2010), p. 065002.

[59] B. Wu, A. Zimmers, H. Aubin, R. Ghosh, Y. Liu, and R. Lopez, "Electric-field-driven phase transition in vanadium dioxide", *Physical Review B* 84 (2011), p. 241410.

[60] A. Zimmers, L. Aigouy, M. Mortier, A. Sharoni, S. Wang, K. G. West, J. G. Ramirez, and I. K. Schuller, "Role of thermal heating on the voltage induced insulator-metal transition in VO_2", *Physical Review Letters* 110 (2013), p. 056601.

[61] A. Rana, C. Li, G. Koster, and H. Hilgenkamp, "Resistive switching studies in VO_2 thin films", *Scientific Reports* 10 (2020).

[62] J. del Valle, R. Rocco, C. Domínguez, J. Fowlie, S. Gariglio, M. J. Rozenberg, and J. M. Triscone, "Dynamics of the electrically induced insulator-to-metal transition in rare-earth nickelates", *Physical Review B* 104 (2021), p. 165141.

[63] H. S. Choi, J. S. Ahn, J. H. Jung, T. W. Noh, and D. H. Kim, "Mid-infrared properties of a VO_2 film near the metal-insulator transition", *Physical Review B* 54 (1996), pp. 4621–4628.

[64] A. Pofelski, S. Valencia, Y. Kalcheim, A. Salev P.and Rivera, C. Huang, M. A. Mawass, F. Kronast, I. K. Schuller, Y. Zhu, and J. del Valle, "Domain nucleation across the metal-insulator transition of self-strained V_2O_3 films", *Physical Review Materials* 8 (2024), p. 035003.

[65] A. M. Alsaqqa, S. Singh, S. Middey, M. Kareev, J. Chakhalian, and G. Sambandamurthy, "Phase coexistence and dynamical behavior in $NdNiO_3$ ultrathin films", *Physical Review B* 95 (2017), p. 125132.

[66] R. S. Bisht, S. Samanta, and A. K. Raychaudhuri, "Phase coexistence near the metal-insulator transition in a compressively strained $NdNiO_3$: Scanning tunneling, noise, and impedance spectroscopy studies", *Physical Review B* 95 (2017), p. 115147.

[67] K. W. Post, A. S. McLeod, M. Hepting, M. Bluschke, Y. Wang, G. Cristiani, G. Logvenov, A. Charnukha, G. X. Ni, P. Radhakrishnan, M. Minola, A. Pasupathy, A. V. Boris, E. Benckiser, K. A. Dahmen, E. W. Carlson, B. Keimer, and D. N. Basov, "Coexisting first- and second-order electronic phase transitions in a correlated oxide", *Nature Physics* 14 (2018), pp. 1056–1061.

[68] H. Madan, M. Jerry, A. Pogrebnyakov, T. Mayer, and S. Datta, "Quantitative mapping of phase coexistence in Mott-Peierls insulator during electronic and thermally driven phase transition", *ACS Nano* 9 (2015), pp. 2009–2017.

[69] T. Luibrand, A. Bercher, R. Rocco, F. Tahouni-Bonab, L. Varbaro, C. W. Rischau, C. Domínguez, Y. Zhou, W. Luo, S. Bag, L. Fratino, R. Kleiner, S. Gariglio, D. Koelle, J. M. Triscone, M. J. Rozenberg, A. B. Kuzmenko, S. Guénon, and J. del Valle, "Characteristic length scales of the electrically induced insulator-to-metal transition", *Physical Review Research* 5 (2023), p. 013108.

[70] C. W. Rischau, S. Gariglio, J. M. Triscone, and J. del Valle, "Resistive switching of VO_2 films grown on a thermal insulator", *Physical Review Applied* 22 (2024), p. 014021.

[71] P. Stoliar, L. Cario, E. Janod, B. Corraze, C. Guillot-Deudon, S. Salmon-Bourmand, V. Guiot, J. Tranchant, and M. Rozenberg, "Universal electric-field-driven resistive transition in narrow-gap Mott insulators", *Advanced Materials* 25 (2013), pp. 3222–3226.

[72] D. J. Wouters, S. Menzel, J. A. J. Rupp, T. Hennen, and R. Waser, "On the universality of the I–V switching characteristics in non-volatile and volatile resistive switching oxides", *Faraday Discussions* 213 (2019), pp. 183–196.

[73] T. Driscoll, H. T. Kim, B. G. Chae, B. J. Kim, Y. W. Lee, N. M. Jokerst, S. Palit, D. R. Smith, M. Di Ventra, and D. N. Basov, "Memory metamaterials", *Science* 325 (2009), pp. 1518–1521.

[74] A. Chen, S. Haddad, Y. C. Wu, T. N. Fang, Z. Lan, S. Avanzino, S. Pangrle, M. Buynoski, M. Rathor, C. Wei, N. Tripsas, C. Bill, M. Van Buskirk, and M. Taguchi, "Non-volatile resistive switching for advanced memory applications", *IEEE International Electron Devices Meeting, IEDM Technical Digest.* 2005, pp. 746–749.

[75] S. Sahoo, H. S. Kunwar, S. Yadav, R. Rawat, V. Sathe, D. M. Phase, and R. J. Choudhary, "Memristive thermal switching in epitaxial V_2O_3 thin film", *Journal of Alloys and Compounds* 970 (2024), p. 172620.

[76] F. Tahouni, "Microscopic study of resistive switching in $NdNiO_3$ and $SmNiO_3$ planar thin film devices", *Master thesis, Universität Tübingen* (2022).

[77] V. Martelli, J. L. Jimenez, M. Continentino, E. Baggio-Saitovitch, and K. Behnia, "Thermal transport and phonon hydrodynamics in strontium titanate", *Physical Review Letters* 120 (2018), p. 125901.

[78] J. del Valle, P. Salev, F. Tesler, N. M. Vargas, Y. Kalcheim, P. Wang, J. Trastoy, M. H. Lee, G. Kassabian, J. G. Ramírez, M. J. Rozenberg, and I. K. Schuller, "Subthreshold firing in Mott nanodevices", *Nature* 569 (2019), pp. 388–392.

[79] M. D. Pickett, G. Medeiros-Ribeiro, and R. S. Williams, "A scalable neuristor built with Mott memristors", *Nature Materials* 12 (2012), pp. 114–117.

[80] N. Shukla, A. V. Thathachary, A. Agrawal, H. Paik, A. Aziz, D. G. Schlom, S. K. Gupta, R. Engel-Herbert, and S. Datta, "A steep-slope transistor based on abrupt electronic phase transition", *Nature Communications* 6 (2015).

[81] J. Seidel, L. W. Martin, Q. He, Q. Zhan, Y. H. Chu, A. Rother, M. E. Hawkridge, P. Maksymovych, P. Yu, M. Gajek, N. Balke, S. V. Kalinin, S. Gemming, F. Wang, G. Catalan, J. F. Scott, N. A. Spaldin, J. Orenstein, and R. Ramesh, "Conduction at domain walls in oxide multiferroics", *Nature Materials* 8 (2009), pp. 229–234.

[82] D. Meier, J. Seidel, A. Cano, K. Delaney, Y. Kumagai, M. Mostovoy, N. A. Spaldin, R. Ramesh, and M. Fiebig, "Anisotropic conductance at improper ferroelectric domain walls", *Nature Materials* 11 (2012), pp. 284–288.

[83] G. Catalan, J. Seidel, R. Ramesh, and J. F. Scott, "Domain wall nanoelectronics", *Reviews of Modern Physics* 84 (2012), pp. 119–156.

[84] E. K. H. Salje, "Multiferroic domain boundaries as active memory devices: trajectories towards domain boundary engineering", *ChemPhysChem* 11 (2010), pp. 940–950.

[85] G. Shirane and Y. Yamada, "Lattice-dynamical study of the 110 K phase transition in $SrTiO_3$", *Physical Review* 177 (1969), pp. 858–863.

[86] K. A. Mueller and H. Burkard, "$SrTiO_3$: An intrinsic quantum paraelectric below 4 K", *Physical Review B* 19 (1979), pp. 3593–3602.

[87] J. Yue, Y. Ayino, T. K. Truttmann, M. N. Gastiasoro, E. Persky, A. Khanukov, D. Lee, L. R. Thoutam, B. Kalisky, R. M. Fernandes, V. S. Pribiag, and B. Jalan, "Anomalous transport in high-mobility superconducting $SrTiO_3$ thin films", *Science Advances* 8 (2022).

[88] A. Ohtomo and H. Y. Hwang, "A high-mobility electron gas at the $LaAlO_3/SrTiO_3$ heterointerface", *Nature* 427 (2004), pp. 423–426.

[89] R. N. Gurzhi, "Hydrodynamic effects in solids at low temperature", *Soviet Physics Uspekhi* 11 (1968), pp. 255–270.

[90] M. Lange, S. Guenon, F. Lever, R. Kleiner, and D. Koelle, "A high-resolution combined scanning laser and widefield polarizing microscope for imaging at temperatures from 4 K to 300 K", *Review of Scientific Instruments* 88 (2017).

[91] M. Lange, S. Guenon, Y. Kalcheim, T. Luibrand, N. M. Vargas, D. Schwebius, R. Kleiner, I. K. Schuller, and D. Koelle, "Imaging of electrothermal filament formation in a Mott insulator", *Physical Review Applied* 16 (2021), p. 054027.

[92] H. J. H. Ma, S. Scharinger, S. W. Zeng, D. Kohlberger, M. Lange, A. Stoehr, X. R. Wang, T. Venkatesan, R. Kleiner, J. F. Scott, J. M. D. Coey, D. Koelle, and A. Ariando, "Local electrical imaging of tetragonal domains and field-induced ferroelectric twin walls in conducting $SrTiO_3$", *Physical Review Letters* 116 (2016), p. 257601.

[93] S. Guenon, S. Scharinger, S. Wang, J. G. Ramirez, D. Koelle, R. Kleiner, and I. K. Schuller, "Electrical breakdown in a V_2O_3 device at the insulator-to-metal transition", *Europhysics Letters* 101 (2013), p. 57003.

[94] A. S. McLeod, E. van Heumen, J. G. Ramirez, S. Wang, T. Saerbeck, S. Guenon, M. Goldflam, L. Anderegg, P. Kelly, A. Mueller, M. K. Liu, Ivan K. Schuller, and D. N. Basov, "Nanotextured phase coexistence in the correlated insulator V_2O_3", *Nature Physics* 13 (2016), pp. 80–86.

[95] D. Wegkamp and J. Stähler, "Ultrafast dynamics during the photoinduced phase transition in VO_2", *Progress in Surface Science* 90 (2015), pp. 464–502.

[96] A. Singer, J. G. Ramirez, I. Valmianski, D. Cela, N. Hua, R. Kukreja, J. Wingert, O. Kovalchuk, J. M. Glownia, M. Sikorski, M. Chollet, M. Holt, I. K. Schuller, and O. G. Shpyrko, "Nonequilibrium phase precursors during a photoexcited insulator-to-metal transition in V_2O_3", *Physical Review Letters* 120 (2018), p. 207601.

[97] A. Ronchi, P. Franceschini, A. De Poli, P. Homm, A. Fitzpatrick, F. Maccherozzi, G. Ferrini, F. Banfi, S. S. Dhesi, M. Menghini, M. Fabrizio, J. P. Locquet, and C. Giannetti, "Nanoscale self-organization and metastable non-thermal metallicity in Mott insulators", *Nature Communications* 13 (2022).

[98] Z. Tao, F. Zhou, T. R. T. Han, D. Torres, T. Wang, N. Sepulveda, K. Chang, M. Young, R. R. Lunt, and C. Y. Ruan, "The nature of photoinduced phase transition and metastable states in vanadium dioxide", *Scientific Reports* 6 (2016).

[99] T. Bar, S. K. Choudhary, M. A. Ashraf, K. S. Sujith, S. Puri, S. Raj, and B. Bansal, "Kinetic spinodal instabilities in the Mott transition in V_2O_3 : Evidence from hysteresis scaling and dissipative phase ordering", *Physical Review Letters* 121 (2018), p. 045701.

[100] O. D. Schneble, I. A. Leahy, J. D. Zimmerman, and M. B. Tellekamp, "Electrically-driven IMT and volatile memristor behavior in $NdNiO_3$ films", *Journal of Physics D: Applied Physics* 57 (2024), p. 485301.

[101] U. Khandelwal, Q. Guo, B. Noheda, P. Nukala, and S. Chandorkar, "Dynamics of voltage-driven self-sustained oscillations in $NdNiO_3$ neuristors", *ACS Applied Electronic Materials* 5 (2023), pp. 3859–3864.

[102] T. Klitsner and R. O. Pohl, "Phonon scattering at silicon crystal surfaces", *Physical Review B* 36 (1987), pp. 6551–6565.

[103] R. B. Peterson, "Direct simulation of phonon-mediated heat transfer in a Debye crystal", *Journal of Heat Transfer* 116 (1994), pp. 815–822.

[104] P. Torres, F. X. Alvarez, X. Cartoixà, and R. Rurali, "Thermal conductivity and phonon hydrodynamics in transition metal dichalcogenides from first-principles", *2D Materials* 6 (2019), p. 035002.

[105] K. Esfarjani and J. Shiomi, "Fundamentals and advances in thermal transport in thermoelectric materials", *MRS Bulletin* 50 (2025), pp. 935–944.

[106] Y. Machida, N. Matsumoto, T. Isono, and K. Behnia, "Phonon hydrodynamics and ultrahigh–room-temperature thermal conductivity in thin graphite", *Science* 367 (2020), pp. 309–312.

[107] Y. Machida, A. Subedi, K. Akiba, A. Miyake, M. Tokunaga, Y. Akahama, K. Izawa, and K. Behnia, "Observation of Poiseuille flow of phonons in black phosphorus", *Science Advances* 4 (2018).

[108] R. Ouillon, J. P. Pinan-Lucarre, P. Ranson, P. Pruzan, S. K. Mishra, R. Ranjan, and D. Pandey, "A Raman scattering study of the phase transitions in $SrTiO_3$ and in the mixed system $(Sr_{1-x}Ca_x)TiO_3$ at ambient pressure from $T = 300$ K down to 8 K", *Journal of Physics: Condensed Matter* 14 (2002), pp. 2079–2092.

[109] D. Chapron, F. Cordero, and M. D. Fontana, "Characterization of oxygen vacancies in $SrTiO_3$ by means of anelastic and Raman spectroscopy", *Journal of Applied Physics* 126 (2019).

[110] J. Ding, J. Zhang, J. Dong, K. Higuchi, A. Nakamura, W. Lu, B. Sun, and X. Fang, "Effective reduction in thermal conductivity by high-density dislocations in $SrTiO_3$", *Applied Physics Letters* 126 (2025).

[111] M. Zacharias, G. Volonakis, F. Giustino, and J. Even, "Anharmonic lattice dynamics via the special displacement method", *Physical Review B* 108 (2023), p. 035155.

[112] K. H. Shin, S. Jeong, J. Yoon, E. Kim, W. K. Hong, and J. I. Sohn, "Metallic filament domain dynamics-induced abrupt resistive switching characteristics with small hysteresis in two dimensional-crystalline VO_2 films", *Journal of Alloys and Compounds* 960 (2023), p. 171035.

[113] S. Cheng, M. H. Lee, X. Li, L. Fratino, F. Tesler, M. G. Han, J. del Valle, R. C. Dynes, M. J. Rozenberg, I. K. Schuller, and Y. Zhu, "*Operando* characterization of conductive filaments during resistive switching in Mott VO_2", *Proceedings of the National Academy of Sciences* 118 (2021).

[114] E. Kisiel, P. Salev, I. Poudyal, D. J. Alspaugh, F. Carneiro, E. Qiu, F. Rodolakis, Z. Zhang, O. G. Shpyrko, M. Rozenberg, I. K. Schuller, Z. Islam, and A. Frano, "High-resolution full-field structural microscopy of the voltage-induced filament formation in VO_2-based neuromorphic devices", *ACS Nano* 19 (2025), pp. 15385–15394.

[115] J. Yoon, G. Lee, C. Park, B. S. Mun, and H. Ju, "Investigation of length-dependent characteristics of the voltage-induced metal insulator transition in VO_2 film devices", *Applied Physics Letters* 105 (2014).

[116] I. Valmianski, P. Y. Wang, S. Wang, J. G. Ramirez, S. Guenon, and I. K. Schuller, "Origin of the current-driven breakdown in vanadium oxides: Thermal versus electronic", *Physical Review B* 98 (2018), p. 195144.

[117] S. Kumar, M. D. Pickett, J. P. Strachan, G. Gibson, Y. Nishi, and R. S. Williams, "Local temperature redistribution and structural transition during Joule-heating-driven conductance switching in VO_2", *Advanced Materials* 25 (2013), pp. 6128–6132.

Appended publications

Publication 1

Reproduced with permission from
T. Luibrand *et al.*, Phys. Rev. B **110**, L081108 (2024)
© 2024 American Physical Society

Letter | Editors' Suggestion

Laser-induced quenching of metastability at the Mott insulator to metal transition

Theodor Luibrand,[1] Lorenzo Fratino,[2,3,4] Farnaz Tahouni-Bonab,[1] Amihai Kronman,[5] Yoav Kalcheim,[4,5] Ivan K. Schuller,[4] Marcelo Rozenberg,[3,4] Reinhold Kleiner,[1] Dieter Koelle,[1] and Stefan Guénon[1,*]

[1]*Physikalisches Institut, Center for Quantum Science (CQ) and LISA⁺, Eberhard Karls Universität Tübingen, Auf der Morgenstelle 14, 72076 Tübingen, Germany*

[2]*CNRS Laboratoire de Physique Théorique et Modélisation, CY Cergy Paris Université, 95302 Cergy-Pontoise Cedex, France*

[3]*CNRS Laboratoire de Physique des Solides, Université Paris-Saclay, 91405 Orsay, France*

[4]*Center for Advanced Nanoscience, Department of Physics, University of California-San Diego, 9500 Gilman Drive, La Jolla, California 92093-0319, USA*

[5]*Department of Materials Science and Engineering, Technion–Israel Institute of Technology, Technion City, 32000 Haifa, Israel*

(Received 22 January 2024; revised 5 May 2024; accepted 23 July 2024; published 14 August 2024)

There is growing interest in strongly correlated insulator thin films because the intricate interplay of their intrinsic and extrinsic state variables causes memristive behavior that might be used for biomimetic devices in the emerging field of neuromorphic computing. In this study we find that laser irradiation tends to drive V_2O_3 from supercooled/superheated metastable states toward thermodynamic equilibrium, most likely in a nonthermal way. We study thin films of the prototypical Mott-insulator V_2O_3, which show spontaneous phase separation into metal-insulator herringbone domains during the Mott transition. Here, we use low-temperature microscopy to investigate how these metal-insulator domains can be modified by scanning a focused laser beam across the thin film surface. We find that the response depends on the thermal history: When the thin film is heated from below the Mott transition temperature, the laser beam predominantly induces metallic domains. On the contrary, when the thin film is cooled from a temperature above the transition, the laser beam predominantly induces insulating domains. Very likely, the V_2O_3 thin film is in a superheated or supercooled state, respectively, during the first-order phase transition, and the perturbation by a laser beam drives these metastable states into stable ones. This way, the thermal history is locally erased. Our findings are supported by a phenomenological model with a laser-induced lowering of the energy barrier between the metastable and equilibrium states.

DOI: 10.1103/PhysRevB.110.L081108

Strongly correlated insulator thin films are the subject of intensive research in the emerging field of neuromorphic computing [1–4]. If these materials are cooled to a temperature below the transition temperature, the charge carrier mobility is considerably reduced due to electron-electron correlation effects like the Mott-Hubbard interaction (e.g., V_2O_3 [5–9]), charge transfer (e.g., rare-earth nickelates [10,11]), or dimerization (e.g., VO_2) [12]. This reduction in charge carrier mobility results in a metal-to-insulator transition (MIT) [13]. An equivalent insulator-to-metal transition (IMT) is observed during heating. The electron-electron correlation effects cause an intricate interplay of intrinsic and extrinsic state variables that can be leveraged for engineering neuromorphic devices [14]. One way to influence strongly correlated insulator thin-film devices externally is through exposure to light. For instance, light is used to trigger resistive switching [15–18], to tune the resistive switching voltage thresholds [19], or to tune the frequency of relaxation oscillators [20] in VO_2 devices. Furthermore, because strongly correlated insulator thin-film neuromorphic devices are usually operated in a critical state at the onset of the IMT/MIT, their functionality is affected by thermodynamics of phase transitions. For instance, the hysteresis in resistance R vs temperature T curves due to the first-order MIT/IMT in VO_2 is leveraged for multistate resistive switching [21–23]. In V_2O_3, the MIT/IMT is accompanied by structural (corundum to monclinic) and magnetic (paramagnetic to antiferromagnetic) phase transitions, providing a complex interplay of many degrees of freedom [24–27].

It is widely recognized that the Mott transition in V_2O_3 is of first-order. However, the implication that the thermodynamic states must be metastable due to fundamental thermodynamics needs to be addressed. Here, we investigate how a laser induced local perturbation affects metastability in a V_2O_3 thin film. We recorded the laser light induced phase transitions at temperatures during the IMT/MIT by acquiring photomicrographs. While at the IMT, the metal phase is induced, the insulating phase is predominantly induced at the MIT. The latter is very intriguing, because one might expect the main effect of the laser irradiation to be heating, which is expected to drive the system toward a more metallic state. To study this phenomenon further, we investigated the filling factors of the insulating and metallic phases and found that after laser irradiation, the filling factors of the heating and cooling branches are almost identical. The behavior is reproduced in a phenomenological numerical model.

The sample under investigation is a continuous 300 nm thick rf-sputtered V_2O_3 film on an r-cut sapphire substrate

*Contact author: stefan.guenon@uni-tuebingen.de

 ©2024 American Physical Society

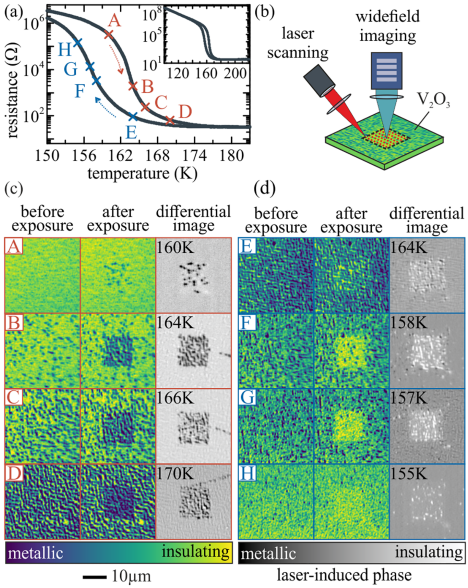


FIG. 1. (a) Zoom into the phase transition region of the $R(T)$ curve. The red and blue dashed arrows indicate the heating and cooling branch, respectively. Inset: Full $R(T)$ curve of the V_2O_3 thin film sample under investigation with same units as in the main graph. The capital letters mark the set temperatures in one thermal cycle, at which separated squares in the V_2O_3 thin film were irradiated using the laser scanning mode. (b) Simplified schematic of the measurement setup. Photomicrographs are acquired by widefield microscopy before and after laser scanning within the dashed square of pristine areas. (c) Photomicrograph series demonstrating the laser scanning irradiation effect acquired during one heating run. For the differential images, the image before laser irradiation was subtracted from the image after scanning. The image contrasts were optimized for every temperature. (d) Photomicrograph series acquired during cooling, analogous to (c).

with gold electrodes evaporated on top (see Ref. [28] for details); Figure 1(a) shows its $R(T)$ curve for both heating and cooling. The resistance change of four orders of magnitude at the phase transition is a sign of high film quality.

We used the same optical microscopy setup as in Lange *et al.* [29], where we have demonstrated that the change in reflectivity allows for imaging the separation of the insulating and metallic phases with 0.5 μm spatial resolution. As described in Refs. [30,31], the setup is a cryogenic combined widefield and laser scanning microscope. The sample is mounted in vacuum on the coldfinger of a liquid Helium continuous-flow cryostat. A sketch of the experimental setup is shown in Fig. 1(b), and a detailed description is given in Ref. [32] (Sec. I).

For this study, the photomicrographs are acquired in the widefield mode with a monochromatic (532 nm) LED illumination, and the laser scanning mode is used for exposing the sample under investigation to laser light from a 405 nm wavelength laser diode operated in the continuous wave mode. The theoretical laser spot diameter on the thin-film surface is 322 nm. We have measured the incident laser power on the sample surface by replacing the sample with a photodiode. The maximum laser power is 919 μW. However, different laser powers were chosen, throughout this study.

For exposure, the selected area is scanned line by line (line separation 100 nm) as depicted in Fig. 1(b). During each line scan, the laser spot stays at a position for 13 ms then it moves to the next position at a distance of 100 nm.

The procedure to investigate the effect of laser scanning irradiation is as follows:

(1) A photomicrograph (32×32 μm^2) of the thin film is acquired.

(2) A selected area (14×14 μm^2) is exposed to laser light.

(3) A second photomicrograph is acquired.

(4) For the differential image, the first photomicrograph is subtracted from the second.

With this procedure, the laser-induced changes from the metallic to the insulating and from the insulating to the metallic phases are mapped.

We have exposed a V_2O_3 thin film by laser light at different temperatures during the IMT/MIT (Fig. 1). The $R(T)$ curve shows a hysteresis of several Kelvins due to the first-order nature of the IMT/MIT [7]. During heating of the sample from 80 K to room temperature, the heating was interrupted four times during the IMT, and a pristine (unirradiated) 14×14 μm area was exposed with 0.1 mW laser power according to the procedure described above. The same procedure was chosen for cooling from room temperature to 80 K with 0.6 mW laser power. Note, that we chose different pristine areas on the sample for each scanning procedure.

The photomicrographs in Figs. 1(c) and 1(d) (in particular, D and E) show the characteristic herringbone domain pattern due to strain-induced separation of the metallic and insulating phases [29,33]. It is important to note that these domain patterns are static on the time scale of at least 15 minutes and do not change, if the thin film is left undisturbed at a fixed temperature. The key result of this study is that during heating, mostly metallic domains are induced [dark patches in the differential images in Figs. 1(c) and 1(d)], whereas during cooling, predominantly insulating domains are created by laser irradiation [bright patches in the differential images in Figs. 1(c) and 1(d)]. Furthermore, laser scanning irradiation does not smear or destroy the herringbone domain patterns but modifies them by changing the ratio of the metallic and insulating surface areas. If left undisturbed, the domains in the irradiated areas are static for at least ten minutes.

In an additional experiment on a patterned V_2O_3 thin film microbridge (see Fig. S2 in Ref. [32]), we show that indeed the laser-scanning-induced phase change has a significant effect on the film resistivity. Moreover, we observe that the size of the laser-induced domains is similar to the size of the domains of the temperature-driven phase transition without laser exposure. This indicates that domain walls permeate the whole film, and that the laser-induced phase transition is not only due to a surface effect.

We also modified the laser irradiation procedure to determine the power thresholds for laser-induced phase changes during heating and cooling (see Sec. III in Ref. [32] for details). It was found that laser irradiation already at relatively low power levels induces predominantly a metallic phase during heating (i.e., IMT), while during cooling (i.e., MIT), the required laser power for inducing predominantly an insulating phase is considerably larger. Moreover, the temperature range, in which a laser-induced phase change was observable, is larger during IMT, compared to MIT. Hence, the heating branch of the transition seems to be more sensitive to laser irradiation than the cooling branch.

For a quantitative analysis of the laser-induced phase changes, we investigated the filling factors, i.e., the ratio between the surface area of a particular phase and the total surface area of interest at a laser power of 460 μW. This laser power was chosen because it is far from the minimum and maximum threshold values for both cooling and heating (see Sec. III in Ref. [32]). As mentioned above, the metallic and insulating thin-film areas can be clearly distinguished by their brightness level in the photomicrographs (see Fig. 1 and [29]). However, these brightness levels change from micrograph to micrograph. Therefore, the following evaluation procedure was used for determining the filling factors. We visually inspected the (differential) micrographs in Fiji [34] and chose an upper and lower limit for the brightness that separates the particular two phases. A third brightness level was calculated by averaging the upper and lower limit. For these three brightness values, we calculated the filling factors, which correspond to the data points and the error bars in Fig. 2 using a Python routine.

Figures 2(a) and 2(b) show the temperature dependence of the filling factors of the laser-induced metallic and insulating phases during heating and cooling, respectively. Except for the fact that in the heating case, predominantly the metallic, and in the cooling case, predominantly the insulating phase is created, the overall behavior is very similar: the laser irradiation switches a considerable percentage of the thin-film area during the IMT from insulating to metallic (40% at 164 K) and during the MIT from metallic to insulating (28% at 162 K). Furthermore, in both cases, there is a temperature interval in which a smaller amount of the minor phase (insulating at the IMT and metallic at the MIT) is induced as well.

Figure 2(c) shows the filling factor of the insulating phase before and after laser irradiation. The error bars of the before-irradiation graphs are smaller compared to the after-irradiation graphs because a larger area was used for determining the filling factors before irradiation. Like the $R(T)$ curves shown in Fig. 1(a), the before-irradiation curves are hysteretic due to the first-order character of the IMT/MIT phase transitions. Most importantly, the after-irradiation curves (dashed lines) lay between the curves before irradiation and are almost identical for temperatures at 168 K and below (solid lines). This implies that after irradiation, it is no longer possible to decide (by means of the filling factor) whether the film was in the heating or cooling branch. In this sense, laser irradiation above the power threshold erases the thermal history of the V_2O_3 thin film.

The most intriguing result of this study is that laser irradiation predominantly induces insulating domains in large

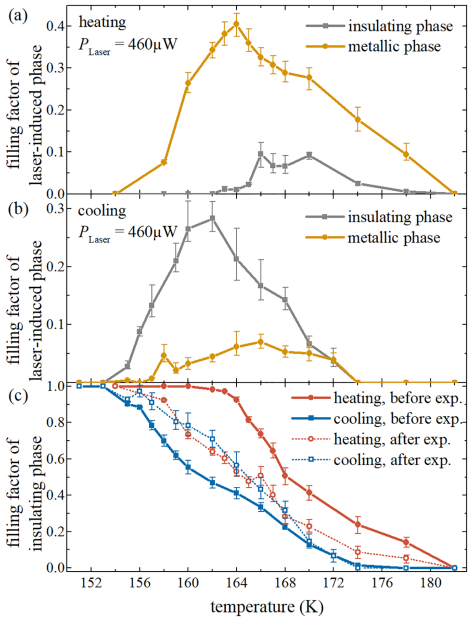


FIG. 2. Temperature dependence of metal and insulator filling factors affected by laser irradiation of 460 μW. (a) Filling factors of the metallic and insulating phases induced by laser irradiation during heating. (b) Same filling factors during cooling. (c) Filling factors of the insulating phase during one thermal cycle.

amounts during cooling. Considering the laser spot as a local heat source, it is not surprising that laser irradiation induces metallic domains since the metallic phase is the high-temperature phase of the Mott transition. Indeed, we observe this behavior during heating of the sample through the IMT. However, the predominant laser-induced creation of insulating domains during cooling is puzzling. In other words, why does the effect of laser irradiation depend on the thermal history? To answer this question, the thermodynamic nature of the MIT/IMT of the V_2O_3 thin film must be considered.

The thermodynamic description of V_2O_3 thin films is the subject of ongoing research [35–37]. The $R(T)$ hysteresis and the associated latent heat indicate a first-order phase transition. Moreover, it is recognized that at the MIT, three phase transitions are coupled: first, an electronic transition due to Mott-Hubbard charge carrier localization; second, a magnetic transition from a paramagnetic-to-antiferromagnetic state; and third, a structural transition from corundum to a monoclinic crystal structure. Simultaneous to the Mott transition, there is the spontaneous separation in the metallic and insulating phases forming herringbone domains [33].

As indicated in Ref. [29], these characteristic herringbone domain patterns resemble the solutions of the Cahn-Larché equation describing a phase separation due to spinodal

decomposition of an elastically stressed system [38]. Other studies also indicate that the IMT/MIT is associated with a spinodal instability [39,40].

Due to the fundamental thermodynamic characteristics of a first-order phase transition, the V_2O_3 thin film is in a metastable superheated state during the IMT, and it is in a metastable supercooled state during the MIT. The most likely interpretation of our results is that the perturbation releases the V_2O_3 thin film from its metastable state, and when the laser spot moves to a new position, the thin film relaxes locally into a stable state.

The general details on how the laser spot on the thin film surface affects the metastability of V_2O_3 are elusive. As discussed above, laser-induced heating needs to be considered. The V_2O_3 thin film is thermally coupled via the sapphire substrate to the cold finger of the cryostat fixed at the set temperature. The focused laser spot locally raises the film temperature. Because the sapphire substrate has a high thermal conductance, the coupling of the V_2O_3 film to the thermal bath is expected to be strong. Consequently, the temperature distribution relaxes in a new steady state on a fast time scale when the laser spot position changes during the scanning procedure.

As a further contribution to the open question of the laser perturbation mechanism, we measured electrical transport properties during minor thermal cycles to investigate how heating affects a V_2O_3 thin film in the critical state at the MIT. This procedure emulates a heat source that changes the temperature gradually on a large length scale. A detailed description and discussion of these additional experiments can be found in Ref. [32] (Sec. IV). Although we found that a minor heating cycle can indeed increase the resistance, the effect is not strong enough to account for what we observed in the laser irradiation experiment. Hence, additional effects might be at play, for instance, a photoinduced change of the $3d$-orbital occupation could trigger the formation of metallic nanodroplets in the IMT [41].

To elaborate on the matter of metastability, we discuss a phenomenological numerical model. In a two-dimensional (2D) resistor network, each site can either be metallic or insulating, depending on the local temperature, which is updated at every simulation step. Solving Kirchhoff's laws, currents, and voltages on each site are determined. A first-order Landau-type free energy functional provides stable and metastable states separated by a barrier. The laser irradiation is implemented in the model by decreasing the barrier height to drive transitions between insulating and metallic states. For each site, the escape from a metastable state was determined by comparing random numbers to Boltzmann factors with a constant number of iterations. If the escape criterion is fulfilled, the transition probability is given by a Boltzmann distribution; see Sec. V in Ref. [32] for details.

Our model reproduces the hysteresis in the $R(T)$ curves, as shown in Fig. 3(a). Figure 3(b) shows the evolution of the filling factor of the insulating phase at different laser intensities. With increasing laser intensity the hysteresis is diminished, and eventually it is completely suppressed, similarly to the experimental results in Fig. 2(c). In Fig. 3(c) we present a simulation series of selected network maps before and after laser exposure with moderate laser intensity ($\Gamma/k_B = 600$ K),

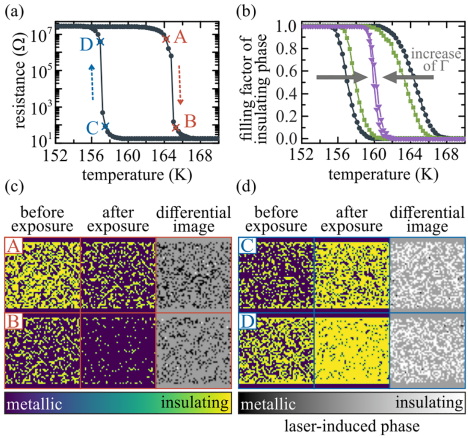


FIG. 3. Results of numerical simulations based on a 2D resistor network model. (a) $R(T)$ curves; arrows indicate heating (red) and cooling (blue) branches. (b) Filling factors of the insulating phase vs T, for various values of laser intensity $\Gamma/k_B = 0$ (gray circles), 600 K (green squares), and 1200 K (purple triangles). (c) Selected network maps before laser exposure, after laser exposure with $\Gamma/k_B = 600$ K, and their corresponding differential images for two temperature values in the heating branch, as indicated with capital letters in (a). (d) same as in (c) , for the cooling branch.

and their corresponding differential images. For heating, the laser induces predominantly metallic sites [Fig. 3(c)] for cooling insulating sites [Fig. 3(d)]. We note that during heating, the majority of sites goes into a metallic state (indicated by black squares in the differential maps), while a few sites revert back to an insulating state (indicated by white squares in the differential maps); this reproduces very well the experimental results. Moreover, this behavior reverses in the cooling branch [Fig. 3(d)], again in agreement with experimental observations. So, according to the simulations, the laser irradiation enhances the process of relaxing the system from a metastable state.

In conclusion, we can state that a V_2O_3 thin film in the metastable state at the IMT/MIT is highly susceptible to a local perturbation by a focused laser beam at the submicrometer scale. Whether the laser perturbation predominantly creates a metallic or insulating phase depends on whether the film is in the heating or cooling branch. Our observations tell that the laser beam brings the system from a supercooled/superheated state to the equilibrium one, provided that the laser power is sufficient to overcome corresponding energy barriers. This implies that laser scanning irradiation can be used to effectively erase thermal history and provides a method to reset memristive devices locally. Our experiments may also be considered as a clear indication that external stimuli on a strongly correlated thin film in a critical state can result in unexpected and presumably nonthermal effects. Nonthermal effects have been investigated in ultrafast pump-probe experiments on VO_2 and V_2O_3 [41–45]. In contrast, in our experiment we

have a quasistatic setting. The discoveries presented here invigorate the emerging field of neuromorphic computing and the research on strongly correlated materials out of equilibrium.

T.L. acknowledges support from the Cusanuswerk, Bischöfliche Studienförderung, F.T. acknowledges support from the Landesgraduiertenförderung Baden-Württemberg, and M.R. acknowledges support from the French ANR MoMA Project No. ANR-19-CE30-0020. Y.K. and A.K. acknowledge funding from the European Union's Horizon Europe Research and Innovation Program under Grant No. 101039986 - ERC - Mottswitch.

Views and opinions expressed are however those of the authors only and do not necessarily reflect those of the European union or the European research council. Work at University of California San Diego (UCSD) was supported through an Energy Frontier Research Center program funded by the U.S. Department of Energy (DOE), Office of Science, Basic Energy Sciences, under Grant No. DE-SC0019273.

[1] I. K. Schuller, R. Stevens, R. Pino, and M. Pechan, Neuromorphic computing: From materials to systems architecture, Report of a roundtable convened to consider neuromorphic computing basic research needs, Technical Report No. 1283147 (U.S. Department of Energy, USA, 2015), https://www.osti.gov/servlets/purl/1283147/.

[2] J. del Valle, J. G. Ramírez, M. J. Rozenberg, and I. K. Schuller, Challenges in materials and devices for resistive-switching-based neuromorphic computing, J. Appl. Phys. **124**, 211101 (2018).

[3] A. Hoffmann, S. Ramanathan, J. Grollier, A. D. Kent, M. J. Rozenberg, I. K. Schuller, O. G. Shpyrko, R. C. Dynes, Y. Fainman, A. Frano, E. E. Fullerton, G. Galli, V. Lomakin, S. P. Ong, A. K. Petford-Long, J. A. Schuller, M. D. Stiles, Y. Takamura, and Y. Zhu, Quantum materials for energy-efficient neuromorphic computing: Opportunities and challenges, APL Mater. **10**, 070904 (2022).

[4] T. J. Park, S. Deng, S. Manna, A. N. M. N. Islam, H. Yu, Y. Yuan, D. D. Fong, A. A. Chubykin, A. Sengupta, S. K. R. S. Sankaranarayanan, and S. Ramanathan, Complex oxides for braininspired computing: A review, Adv. Mater. **35**, 2203352 (2023).

[5] F. J. Morin, Oxides which show a metal-to-insulator transition at the neel temperature, Phys. Rev. Lett. **3**, 34 (1959).

[6] D. B. McWhan and J. P. Remeika, Metal-insulator transition in $(V_{1-x}Cr_x)_2O_3$, Phys. Rev. B **2**, 3734 (1970).

[7] D. B. McWhan, A. Menth, J. P. Remeika, W. F. Brinkman, and T. M. Rice, Metal-insulator transitions in pure and doped V_2O_3, Phys. Rev. B **7**, 1920 (1973).

[8] A. Georges, G. Kotliar, W. Krauth, and M. J. Rozenberg, Dynamical mean-field theory of strongly correlated fermion systems and the limit of infinite dimensions, Rev. Mod. Phys. **68**, 13 (1996).

[9] P. Limelette, A. Georges, D. Jerome, P. Wzietek, P. Metcalf, and J. M. Honig, Universality and critical behavior at the mott transition, Science **302**, 89 (2003).

[10] J. B. Torrance, P. Lacorre, A. I. Nazzal, E. J. Ansaldo, and C. Niedermayer, Systematic study of insulator-metal transitions in perovskites $RNiO_3$ (R = Pr, Nd, Sm, Eu) due to closing of charge-transfer gap, Phys. Rev. B **45**, 8209 (1992).

[11] S. Catalano, M. Gibert, J. Fowlie, J. Íñiguez, J.-M. Triscone, and J. Kreisel, Rare-earth nickelates $RNiO_3$: thin films and heterostructures, Rep. Prog. Phys. **81**, 046501 (2018).

[12] S. Biermann, A. Poteryaev, A. I. Lichtenstein, and A. Georges, Dynamical singlets and correlation-assisted peierls transition in VO_2, Phys. Rev. Lett. **94**, 026404 (2005).

[13] M. Imada, A. Fujimori, and Y. Tokura, Metal-insulator transitions, Rev. Mod. Phys. **70**, 1039 (1998).

[14] Y. Zhou and S. Ramanathan, Mott memory and neuromorphic devices, Proc. IEEE **103**, 1289 (2015).

[15] B.-J. Kim, G. Seo, and Y. W. Lee, Bidirectional laser triggering of planar device based on vanadium dioxide thin film, Opt. Express **22**, 9016 (2014).

[16] J. Kim, S. J. Jeong, B.-J. Kim, and Y. W. Lee, Laser-triggered current gating based on photothermal effect in VO_2 thin-film device using CO_2 laser, Appl. Phys. B **124**, 67 (2018).

[17] G. Seo, B.-J. Kim, Y. Wook Lee, and H.-T. Kim, Photo-assisted bistable switching using mott transition in two-terminal VO_2 device, Appl. Phys. Lett. **100**, 011908 (2012).

[18] G. Li, D. Xie, H. Zhong, Z. Zhang, X. Fu, Q. Zhou, Q. Li, H. Ni, J. Wang, E.-j. Guo, M. He, C. Wang, G. Yang, K. Jin, and C. Ge, Photo-induced non-volatile VO_2 phase transition for neuromorphic ultraviolet sensors, Nat. Commun. **13**, 1729 (2022).

[19] Y.-W. Lee, E.-S. Kim, B.-S. Shin, and S.-M. Lee, High-performance optical gating in junction device based on vanadium dioxide thin film grown by sol-gel method, J. Electr. Eng. Technol. **7**, 784 (2012).

[20] G. Seo, B.-J. Kim, H.-T. Kim, and Y. W. Lee, Photo-assisted electrical oscillation in two-terminal device based on vanadium dioxide thin film, J. Lightwave Technol. **30**, 2718 (2012).

[21] T. Driscoll, H.-T. Kim, B.-G. Chae, M. D. Ventra, and D. N. Basov, Phase-transition driven memristive system, Appl. Phys. Lett. **95**, 043503 (2009).

[22] A. Rana, C. Li, G. Koster, and H. Hilgenkamp, Resistive switching studies in VO_2 thin films, Sci. Rep. **10**, 3293 (2020).

[23] X. Gao, C. M. M. Rosário, and H. Hilgenkamp, Multi-level operation in VO_2-based resistive switching devices, AIP Adv. **12**, 015218 (2022).

[24] Y. Kalcheim, N. Butakov, N. M. Vargas, M.-H. Lee, J. del Valle, J. Trastoy, P. Salev, J. Schuller, and I. K. Schuller, Robust coupling between structural and electronic transitions in a mott material, Phys. Rev. Lett. **122**, 057601 (2019).

[25] B. A. Frandsen, Y. Kalcheim, I. Valmianski, A. S. McLeod, Z. Guguchia, S. C. Cheung, A. M. Hallas, M. N. Wilson, Y. Cai, G. M. Luke, Z. Salman, A. Suter, T. Prokscha, T. Murakami, H. Kageyama, D. N. Basov, I. K. Schuller, and Y. J. Uemura, Intertwined magnetic, structural, and electronic transitions in V_2O_3, Phys. Rev. B **100**, 235136 (2019).

[26] J. Trastoy, A. Camjayi, J. del Valle, Y. Kalcheim, J.-P. Crocombette, D. A. Gilbert, J. A. Borchers, J. E. Villegas, D. Ravelosona, M. J. Rozenberg, and I. K. Schuller, Magnetic

field frustration of the metal-insulator transition in V_2O_3, Phys. Rev. B **101**, 245109 (2020).

[27] E. Barazani, D. Das, C. Huang, A. Rakshit, C. Saguy, P. Salev, J. del Valle, M. C. Toroker, I. K. Schuller, and Y. Kalcheim, Positive and negative pressure regimes in anisotropically strained V_2O_3 films, Adv. Funct. Mater. **33**, 2211801 (2023).

[28] M. K. Stewart, D. Brownstead, S. Wang, K. G. West, J. G. Ramírez, M. M. Qazilbash, N. B. Perkins, I. K. Schuller, and D. N. Basov, Insulator-to-metal transition and correlated metallic state of V_2O_3 investigated by optical spectroscopy, Phys. Rev. B **85**, 205113 (2012).

[29] M. Lange, S. Guénon, Y. Kalcheim, T. Luibrand, N. M. Vargas, D. Schwebius, R. Kleiner, I. K. Schuller, and D. Koelle, Imaging of electrothermal filament formation in a mott insulator, Phys. Rev. Appl. **16**, 054027 (2021).

[30] M. M. Lange, S. Guénon, F. Lever, R. Kleiner, and D. Koelle, A high-resolution combined scanning laser and widefield polarizing microscope for imaging at temperatures from 4 K to 300 K, Rev. Sci. Instrum. **88**, 123705 (2017).

[31] M. M. Lange, A high-resolution polarizing microscope for cryogenic imaging: Development and application to investigations on twin walls in $SrTiO_3$ and the metal-insulator transition in V_2O_3, Ph.D. thesis, Universität Tübingen, 2018.

[32] See Supplemental Material at http://link.aps.org/supplemental/10.1103/PhysRevB.110.L081108 for details on the sample and measurement setup, a microbridge experiment, thresholds of laser scanning irradiation, analysis of thermal effects via minor loop measurements, and Mott resistor network simulation, which includes Refs. [46–48].

[33] A. S. McLeod, E. van Heumen, J. G. Ramírez, S. Wang, T. Saerbeck, S. Guénon, M. Goldflam, L. Anderegg, P. Kelly, A. Mueller, M. K. Liu, I. K. Schuller, and D. N. Basov, Nanotextured phase coexistence in the correlated insulator V_2O_3, Nat. Phys. **13**, 80 (2017).

[34] J. Schindelin, I. Arganda-Carreras, E. Frise, V. Kaynig, M. Longair, T. Pietzsch, S. Preibisch, C. Rueden, S. Saalfeld, B. Schmid, J.-Y. Tinevez, D. J. White, V. Hartenstein, K. Eliceiri, P. Tomancak, and A. Cardona, Fiji: an open-source platform for biological-image analysis, Nat. Methods **9**, 676 (2012).

[35] C. Castellani, C. DiCastro, D. Feinberg, and J. Ranninger, New model hamiltonian for the metal-insulator transition, Phys. Rev. Lett. **43**, 1957 (1979).

[36] G. Kotliar, E. Lange, and M. J. Rozenberg, Landau theory of the finite temperature mott transition, Phys. Rev. Lett. **84**, 5180 (2000).

[37] M. I. Díaz, J. E. Han, and C. Aron, Electrically driven insulator-to-metal transition in a correlated insulator: Electronic mechanism and thermal description, Phys. Rev. B **107**, 195148 (2023).

[38] H. Garcke and U. Weikard, Numerical approximation of the cahn-larché equation, Numer. Math. **100**, 639 (2005).

[39] T. Bar, S. K. Choudhary, M. A. Ashraf, K. S. Sujith, S. Puri, S. Raj, and B. Bansal, Kinetic spinodal instabilities in the mott transition in V_2O_3: Evidence from hysteresis scaling and dissipative phase ordering, Phys. Rev. Lett. **121**, 045701 (2018).

[40] S. Kundu, T. Bar, R. K. Nayak, and B. Bansal, Critical slowing down at the abrupt mott transition: When the first-order phase transition becomes zeroth order and looks like second order, Phys. Rev. Lett. **124**, 095703 (2020).

[41] A. Ronchi, P. Homm, M. Menghini, P. Franceschini, F. Maccherozzi, F. Banfi, G. Ferrini, F. Cilento, F. Parmigiani, S. S. Dhesi, M. Fabrizio, J.-P. Locquet, and C. Giannetti, Early-stage dynamics of metallic droplets embedded in the nanotextured mott insulating phase of V_2O_3, Phys. Rev. B **100**, 075111 (2019).

[42] F. Giorgianni, J. Sakai, and S. Lupi, Overcoming the thermal regime for the electric-field driven Mott transition in vanadium sesquioxide, Nat. Commun. **10**, 1159 (2019).

[43] A. Cavalleri, C. Toth, C. W. Siders, J. A. Squier, F. Raksi, P. Forget, and J. C. Kieffer, Femtosecond structural dynamics in VO_2 during an ultrafast solid-solid phase transition, Phys. Rev. Lett. **87**, 237401 (2001).

[44] S. Wall, S. Yang, L. Vidas, M. Chollet, J. M. Glownia, M. Kozina, T. Katayama, T. Henighan, M. Jiang, T. A. Miller, D. A. Reis, L. A. Boatner, O. Delaire, and M. Trigo, Ultrafast disordering of vanadium dimers in photoexcited VO_2, Science **362**, 572 (2018).

[45] M. R. Otto, L. P. René de Cotret, D. A. Valverde-Chavez, K. L. Tiwari, N. mond, M. Chaker, D. G. Cooke, and B. J. Siwick, How optical excitation controls the structure and properties of vanadium dioxide, Proc. Natl. Acad. Sci. USA **116**, 450 (2019).

[46] J. Trastoy, Y. Kalcheim, J. del Valle, I. Valmianski, and I. K. Schuller, Enhanced metal–insulator transition in V_2O_3 by thermal quenching after growth, J. Mat. Sci. **53**, 9131 (2018).

[47] J. del Valle, P. Salev, F. Tesler, N. M. Vargas, Y. Kalcheim, P. Wang, J. Trastoy, M.-H. Lee, G. Kassabian, J. G. Ramírez, M. J. Rozenberg, and I. K. Schuller, Subthreshold firing in Mott nanodevices, Nature **569**, 388 (2019).

[48] P. Stoliar, J. Tranchant, B. Corraze, E. Janod, M.-P. Besland, F. Tesler, M. Rozenberg, and L. Cario, A leaky-integrate-and-fire neuron analog realized with a Mott insulator, Advan. Funct. Mater. **27**, 1604740 (2017).

Publication 2

Reproduced with permission from
F. Tahouni-Bonab *et al.*, Phys. Rev. Appl. **24**, 034014 (2025)
© 2025 American Physical Society

Nonvolatile multistate electrothermal resistive switching in a strongly correlated insulator thin-film device

Farnaz Tahouni-Bonab,[1] Matthias Hepting,[2] Theodor Luibrand,[1] Georg Cristiani,[2] Christoph Schmid,[1] Gennady Logvenov,[2] Bernhard Keimer,[2] Reinhold Kleiner,[1,*] Dieter Koelle,[1] and Stefan Guénon[1,†]

[1] *Physikalisches Institut, Center for Quantum Science (CQ) and LISA+, Eberhard Karls Universität Tübingen, Auf der Morgenstelle 14, 72076 Tübingen, Germany*

[2] *Max Planck Institute for Solid State Research, Heisenbergstraße 1, 70569 Stuttgart, Germany*

(Received 28 October 2024; revised 14 April 2025; accepted 11 August 2025; published 5 September 2025)

Strongly correlated insulators, such as Mott or charge-transfer insulators, exhibit a strong temperature dependence in their resistivity. Consequently, self-heating effects can lead to electrothermal instabilities in planar thin-film devices of these materials. When the electrical bias current exceeds a device-specific threshold, the device can switch from a high- to a low-resistance state through the formation of metallic filaments. However, since the filaments are sustained by local Joule heating after they form, reducing the bias current below a second threshold causes them to disappear, returning the device to the high-resistance state. Hence, electrothermal resistive switching is usually volatile. Here, on the contrary, we report on nonvolatile resistive switching in a planar $NdNiO_3$ thin-film device. By combining electrical transport measurements with optical wide-field microscopy, we provide evidence for a metallic filament that persists even after returning the bias current to zero. We attribute this effect to the pronounced hysteresis between the cooling and heating branches in the resistance versus temperature dependence of the device. At least 100 intermediate resistance states can be prepared, which are persistent as long as the base temperature is kept constant. Further, the switching process is nondestructive, and thermal cycling can reset the device to its pristine state.

DOI: 10.1103/h98b-4438

I. INTRODUCTION

The emerging field of neuromorphic computing involves the research and development of hardware and computing paradigms that can effectively mimic the essentials of biological neural networks [1–4]. Resistive switching devices are particularly relevant because these simple two-terminal devices can emulate two central neuromorphic features due to their memristive behavior [5–9]. First, with volatile resistive switching devices, it is possible to mimic the threshold behavior of neurons [10–14]. Second, with nonvolatile resistive switching devices, it is possible to emulate the information storage capability of synapses [5,15–18]. Resistive switching devices abruptly change their intrinsic resistance if their electrical bias exceeds a device-specific threshold. While volatile resistive switching devices are restored to their original resistance state at low electrical bias, the resistance change in nonvolatile resistive switching devices is persistent.

Various material systems showing different resistive switching effects are currently being investigated [19–22]. The present work concerns strongly correlated insulator thin-film devices, which are gaining increasing attention in this research context. These materials, which show a pronounced increase in resistivity at low temperatures due to electron-electron interaction, include Mott [23] and charge-transfer insulators [24–26]. Strongly correlated insulator thin-film devices have a unique feature: the temperature dependence of the resistivity causes electrothermal instability, which can trigger resistive switching due to the formation of a metallic filament [27–34]. Because the electrothermal filament is sustained by local Joule heating, it should disappear at small bias currents. Hence, electrothermal resistive switching in strongly correlated insulator thin-film devices is expected to be volatile. Indeed, most studies on planar strongly correlated insulator thin-film devices demonstrate volatile resistive switching [32,34–37]. However, some studies report on nonvolatile resistive switching due to a hysteretic resistance versus temperature relation [38–50].

Here, we report on nonvolatile resistive switching in a planar two-terminal device based on $NdNiO_3$ (NNO).

*Contact author: kleiner@uni-tuebingen.de
†Contact author: stefan.guenon@uni-tuebingen.de

 © 2025 American Physical Society

NNO is a charge-transfer insulator that exhibits a concomitant metal-to-insulator, structural, and magnetic phase transition [51,52]. In NNO thin films, the transition temperature is highly sensitive to the degree of epitaxial strain between film and substrate as well as the crystallographic orientation of the substrate surface [53–55]. By combining electrical transport measurements with optical microscopy, we demonstrate that the nonvolatile resistive switching is accompanied by the formation of a metallic filament that persists even at zero currents. We argue that the filament formation process is nevertheless electrothermal and that the filament persists due to the pronounced hysteresis in the resistance versus temperature relation of the charge-transfer insulator device.

II. SAMPLE AND METHOD

The sample under investigation consists of planar, two-electrode NNO thin-film devices. Figure 1(a) shows a schematic of the device with its dimensions indicated. The 7-nm-thick NNO film was grown epitaxially via pulsed laser deposition from a stoichiometric NNO target on a (110)-oriented $NdGaO_3$ single crystalline substrate. The deposition temperature was 730°C, the oxygen partial pressure was 0.5 mbar, and the KrF excimer laser pulse rate was 2 Hz with an energy density of 1.6 J cm^{-2}. The film was annealed in a 1-bar oxygen atmosphere at 690°C for 30 min. As a result, the films show a sharp metal-to-insulator transition (MIT) with hysteretic behavior between approximately 155 and 175 K upon cooling and warming [56]. See the methods section and supplemental material of [56] for more details on the growth and physical properties of NNO thin films prepared by this growth procedure. The metal electrodes on the continuous NNO film were structured via optical lithography and a liftoff process. The Ti buffer layer and the Au layer were deposited by electron-beam evaporation with a total thickness of 110 nm.

This study used the wide-field mode of a high-resolution polarizing microscopy setup described in detail in [57,58]. A schematic of the setup is depicted in Fig. 1(b). The sample is mounted in a vacuum on the cold finger of a liquid helium continuous-flow cryostat with a temperature range of 4.2 to 300 K. The system facilitates simultaneous electrical transport measurements and imaging via wide-field microscopy. We used a Keithley 2400 Sourcemeter for the electrical transport measurements as a current source. The spatial resolution of the microscope is 0.48 μm with a 532-nm monochromatic LED illumination.

III. RESULTS

Figure 1(c) shows the resistance R versus temperature T curve of the device acquired during thermal cycling. This means that the sample was cooled from 200 K to 80 K and subsequently heated to 200 K. The strong resistance change between 158 K and 154 K in the cooling branch is indicative of an MIT of the NNO thin film, whereas the resistance change between 170 K and 175 K in the heating branch indicates an insulator-to-metal transition (IMT). The hysteresis between the MIT and IMT indicates a first-order thermodynamic phase transition, and the steep $R(T)$ curves at the MIT and IMT suggest high film quality [56]. Furthermore, there is a broad temperature interval for which the device is entirely metallic during cooling

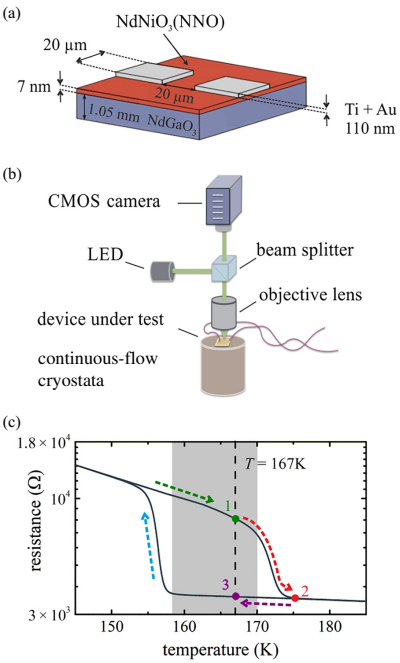


FIG. 1. (a) Schematic of the two-terminal planar device with metal electrodes on top of a continuous NNO thin film. (b) Schematic of the wide-field microscopy setup. (c) $R(T)$ curves of the device acquired with a current $I = 100$ μA during thermal cycling. The arrows indicate the sweep direction. The cooling branch is shifted from the heating branch to lower temperatures by approximately 15 K. For the electrical transport measurements, the thermal cycling was halted during heating at the targeted base temperature of 167 K indicated by a vertical dashed line. This procedure leaves the device in an insulating state on the heating branch (point 1). Heating the device above the insulator-to-metal transition temperature (point 2) and cooling it to the original base temperature puts it into a low-resistance, metallic state (point 3).

and insulating during heating (marked by the gray area in Fig. 1(c). The hysteretic $R(T)$ behavior implies that thermal history can significantly impact the electrical transport properties.

To demonstrate nonvolatile, multistate resistive switching, we halted the thermal cycle at 167 K during heating, leaving the device in an insulating state [see Fig. 1(c)]. Then we applied a sequence of triangular current sweeps, ramping the current I from zero to a maximum current I_{max} and back to zero [see the lower inset of Fig. 2(a)]. Within this sequence I_{max} was first set to 1 mA and subsequently increased in 25-μA steps up to 2 mA. Figure 2(a) shows the current I versus voltage V curves recorded throughout the entire sweep sequence. The zoomed-in $I(V)$ curves [upper inset in Fig. 2(a)] show that even at near-zero currents, the resistance after each cycle does not return to its initial state, confirming nonvolatile resistive switching.

Moreover, with increasing number of sweeps (increasing I_{max}), the conductance (slope of the $I(V)$ curves) monotonically increases. To illustrate this more quantitatively, Fig. 2(b) shows the dependence of the conductance I/V at small bias current $I = 100$ μA and at I_{max} as a function of I_{max} recorded on the return branch of each current sweep. This observation clearly shows that we can create multiple states by choosing different values for I_{max}.

In addition, we repeated the sweep sequence with a smaller step size of 10 μA for I_{max} [Fig. 2(c)]. As shown, 100 intermediate states can be prepared. This suggests that storing information in an analog state with high resolution in the device might be possible. Further, the intermediate states are stable if the base temperature remains unchanged, whereas these nonvolatile states can be erased through thermal cycling, restoring the device to its initial state.

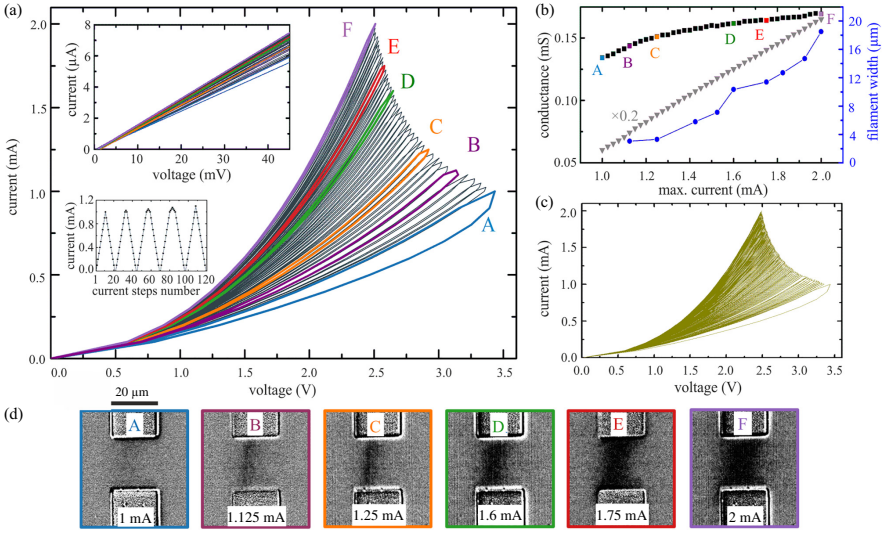


FIG. 2. Nonvolatile electrothermal resistive switching in an NNO two-terminal thin-film device initially prepared in the high-resistance state at $T = 167$ K [point 1 in Fig. 1(c)]. (a) Current-voltage loops measured by applying triangular current sweeps. The lower inset shows the first five sweeps, ramping I from zero to I_{max} and back in 100-μA steps with a 0.5-s time interval. The current interval was reduced to 25 μA for the highest current steps when this was necessary to meet the targeted I_{max}. I_{max} is consecutively increased from 1.0 mA (loop A) in 25 μA steps up to 2.0 mA (loop F). Note that the up-sweeps are almost congruent with the down-sweeps of the preceding loop, except in the small section before reaching the maximum current. The upper inset provides a zoomed-in view of the graph's origin. (b) Device conductance versus I_{max} of the preceding sweep. The black filled squares represent the device conductance at small bias currents (100 μA), while the gray filled triangles show the device conductance scaled by a factor of 0.2 at I_{max}. The blue filled dots show the corresponding filament width extracted from photomicrographs. (c) Series of current-voltage loops with I_{max} increased in 10-μA steps demonstrating the information storage capability of the device. (d) Photomicrographs (differential images) of the device at $I = 0$ after the corresponding current-voltage loops have been acquired. In B–F, the metallic filament is clearly visible. Bottom labels denote I_{max}.

To investigate the observed nonvolatile, multistate resistive switching further, we recorded wide-field photomicrographs of the device at the end of every single current sweep loop, that is, after returning to zero bias current. Figure 2(d) shows a series of photomicrographs taken after loops A–F. These are differential images, with the pristine device image [captured after preparing the device at point 1 in Fig. 1(c) and before initiating the current sweeps] subtracted to enhance contrast. The rectangles at the top and bottom are the metal electrodes of the two-terminal device. Understanding the photomicrographs requires recognizing that metallic and insulating regions of the NNO thin film have distinct reflectivity, with metallic areas appearing darker than insulating ones [34].

Clearly, Fig. 2(d) illustrates that a metallic (dark) filament connects the two electrodes and we find that even after returning the current to zero, this filament persists. Moreover, with increasing I_{max} the width of the filament increases. We estimated the filament width from the optical images and plotted it against I_{max} in Fig. 2(b). Because the filament is lacking clear demarcation, the estimate has an error of several micrometers. Notably, the monotonic increase in conductance correlates with a monotonic increase in filament width. The series of images shown in Fig. 2(d) can explain the observed nonvolatile, multistate resistive switching: We find that even after returning to $I = 0$ a metallic filament persists, which causes a slight increase in the overall conductance of the device, and the observed increase in filament width with increasing I_{max} accounts for the increase in conductance with increasing I_{max}, generating multiple resistive states.

IV. DISCUSSION

The high crystalline quality and phase purity of the NNO film lead to very steep changes in the resistance across the IMT and MIT, while the hysteretic temperature regime is broad, with an interval of at least 10 K, in which the thin film is in a high-resistivity insulating state during heating and a low-resistivity metallic state during cooling. It is this separation of the IMT and MIT that is responsible for the nonvolatile behavior as will be discussed in the following. Note that the base temperature for the electrical transport measurements [Fig. 1(c)] lies precisely in this interval.

We argue that the resistive switching and the filament formation result from electrothermal instability, driven by the steep decline in $R(T)$ due to the IMT, as reported in several studies [27,28,30,32,34]. At currents above a certain threshold, a uniform current distribution becomes unstable as small perturbations in current density are amplified by localized Joule heating, lowering the sheet resistance of the surrounding strongly correlated insulator thin film. This feedback mechanism funnels more and more current into a small section, causing resistive switching. At the end of the resistive switching event, a metallic filament is formed between the two electrodes of the device, reducing its resistance. The electrical current flows almost entirely through the metallic filament, which creates a considerable amount of Joule heating confined in a small area. The local excess temperature caused by the Joule heating is high enough to keep the strongly correlated insulator thin film above the IMT temperature in the metallic state [note points 1 and 2 in the $R(T)$ curve depicted in Fig. 1 (c)]. In this manner, Joule heating sustains and stabilizes the metallic filament. If the current is increased further after the device has switched to the low-resistance state, the Joule heating in the filament is increased, and as a result, the filament becomes wider. Equivalently, the filament width would scale down when the current is reduced. However, in case of the NNO device of this study, the metallic filament width cannot shrink because the NNO film is locally trapped in the metallic state due to the thermal hysteresis [consider point 3 in Fig. 1(c)], and this persists even at zero current.

Next, we address the case when the electrical current is increased from zero bias after a metallic filament already exists. Most of the current is confined to the filament. For small currents, the Joule heating is insufficient to raise the local temperature above the threshold of the IMT, and the filament does not change. Consequently, the up-sweep I-V curves in Fig. 2(a) are almost congruent with the down-sweep curves of the preceding loops. However, suppose the current is increased above the maximum value that was applied to form the filament before. In that case, the excess temperature created by Joule heating in its vicinity is high enough to metalize additional NNO film areas, and the filament width increases. With this mechanism, intermediate resistance states can be prepared [see Figs. 2(a) and 2(c)].

Figure 2(b) illustrates the relationship between the maximum current (I_{max}) and the filament width derived from photomicrographs. The filament width exhibits a monotonic increase with rising I_{max}, consistent with a Joule heating-driven electrothermal mechanism. This widening of the filament corresponds to an expansion of the metallic shunt, leading to enhanced device conductance, as depicted by the curve with gray filled triangles. When the current is reduced from a given I_{max} to a lower value, the filament width remains constant. However, the device conductance decreases due to the nonlinear current-voltage relation. Hence, the conductance values of the black square curve, representing conductance at low currents, are lower than those of the gray triangle curve.

In the photomicrograph showing the device after the first current-voltage loop with a nonvolatile resistance change [Fig. 2(d) A], no metallic filament is visible. This behavior aligns with findings from previous studies [39,43,46]. Driscoll *et al.* [39], in their survey of VO_2 devices, proposed that metallic puddles form at the nanoscale due to a localized increase in Joule heating, resulting from the percolative nature of the material.

We also explored resistive switching at a base temperature lower than that at 167 K discussed above. At 162 K and 160 K, we found that the resistive switching is abrupt rather than gradual, making it impossible to prepare intermediate states (see Appendix).

V. CONCLUSION

In conclusion, we have demonstrated nonvolatile electrothermal resistive switching due to the formation of a persistent metallic filament. Unlike an ion-migration forming process in electronic oxide resistive switching devices, the filament is created due to electrothermal instability. The filament configuration is spatially fixed due to the distinct separation of the heating and cooling branches in the resistance versus temperature relation. We have demonstrated that the device can be prepared in at least 100 states with different resistances, which are stable as long as the temperature is kept constant. The original pristine state can be restored by thermal cycling. Although the nonvolatile resistive switching is, in this sense, not permanent, electrothermal resistive switching devices offer considerably higher endurance than devices based on ion displacement, which makes them attractive candidates for applications where information needs to be stored and erased at high frequencies. Our report on a nonvolatile resistive switching device, which is based on electrothermal instability, not only underscores the potential of strongly correlated insulator thin-film devices but also opens up exciting possibilities for their application in neuromorphic systems, for example, using their information storage capacity for recording synaptic weights.

ACKNOWLEDGMENTS

We thank the instrument scientists Ronny Löffler and Markus Turad of the research and service facility LISA$^+$ for their support in patterning the sample. F.T. acknowledges support from the Landesgraduiertenförderung Baden-Württemberg. T.L acknowledges support from the Cusanuswerk, Bischöfliche Studienförderung.

DATA AVAILABILITY

The data supporting this study are publicly available in a Zenodo repository [59].

APPENDIX: RESISTIVE SWITCHING AT DIFFERENT BASE TEMPERATURES

In addition to studying resistive switching at the base temperature of 167 K (as discussed in the main text), we investigated resistive switching at lower temperatures by applying three consecutive current sweeps (at each base temperature) after the sample was brought into a pristine state via thermal cycling. All base temperatures fall in the bistable interval between the MIT and IMT [Fig. 3(a)]. Figure 3(b) depicts photomicrographs of the device at a bias current of 1.4 mA during the increasing current sweep of the first loop. All images are differential images, that is, the image of the pristine device was subtracted to enhance contrast. The current versus voltage curves are plotted in Figs. 3(c)–3(f).

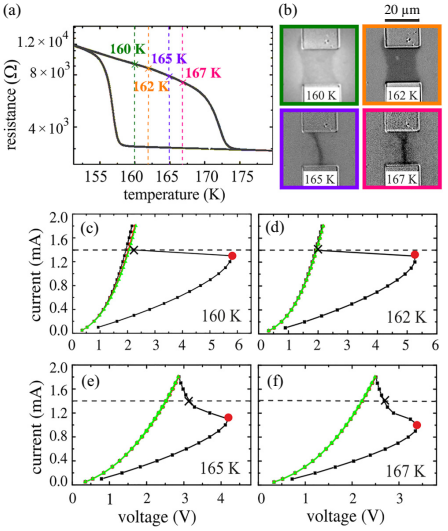


FIG. 3. Nonvolatile resistive switching at different base temperatures in an interval above the MIT and below the IMT. (a) $R(T)$ curves (cooling and heating branches) with $I = 100$ μA. The four base temperatures are indicated by vertical dashed lines. (b) Photomicrographs acquired at 1.4 mA bias current [the bias points during imaging are indicated by black crosses in (c)–(f)] after the device has switched into a low-resistance state. (c)–(f) Current versus voltage curves acquired during three consecutive current sweeps from zero to 1.8 mA bias current and back to zero after the device was brought into a pristine state via thermal cycling. Black curve: first current sweep. Red curve: second current sweep. Green curve: third current sweep. Red dots indicate the bias points at the breakdown voltage.

The I-V curves acquired at the two lower temperatures (160 and 166 K) both show abrupt resistive switching in the first loop, indicated by an almost horizontal line. The up- and down-sweep curves of the second and third loop lie precisely on top of the down-sweep curve of the first loop. Hence, the resistive switching is nonvolatile. The corresponding photomicrographs in Fig. 3(b) that were acquired immediately after the resistive switching event show a

broad metallic filament extending almost over the whole area between the electrodes.

In contrast, the current-voltage curves acquired at the two higher temperatures (165 and 167 K) do not show abrupt but gradual switching in the up-sweep of the first loop. Again, the down-sweep of the first loop and the up- and down-sweeps of the subsequent loops are congruent, indicating nonvolatile resistive switching. The corresponding photomicrographs in Fig. 3(b) show that the filaments are considerably narrower than the electrodes.

To explain the differences between resistive switching at different base temperatures, consider the bias point in the up-sweep of the first loop at the breakdown voltage (red dot in the I-V curve), that is, right before the first resistive switching event. First, note that the breakdown voltage becomes larger with lower base temperatures. Second, the current required to trigger resistive switching is noticeably increased in the case of the two lower base temperatures. Combining these two observations, we can conclude that decreasing temperature increases the electric power required to cause resistive switching. Considering that the resistive switching is due to an electrothermal effect, this makes sense. Since, at low temperatures, the excess temperature to reach the metallic state is large, more Joule heating is needed to bring the device into the electrical bias regime where the system becomes electrothermally unstable. The considerably broader filament at low temperatures is likely the result of an electrical current overshoot, caused either by a parasitic capacitance or by a lag in the control circuit of the current source. Due to this current overshoot, the section between the electrodes is temporarily heated above the IMT temperature; as in the main text, the pronounced hysteresis of the $R(T)$ curve freezes this state.

Regarding the gradual resistive switching observed at the two higher base temperatures ($T = 165$ K and $T = 167$ K), such an I-V shape in an electrothermal unstable device is not new and was, for instance, observed during electrothermal switching (hot spot formation) in $Bi_2Sr_2CaCu_2O_8$ terahertz emitters [60], where it can be attributed to the fact that the three-dimensional character and the boundaries of the system affect temperature redistribution. Similar effects could be at play in the case of the NNO device at base temperatures near the IMT. For instance, the metallic electrodes of the two-terminal device provide thermal cross-coupling, affecting the temperature distribution. Another explanation for the gradual resistive switching might be that the current and temperature redistribution mechanism responsible for filament formation is impeded by the creation of isolated metallic domains (smaller than the spatial resolution of the microscope) when the device is electrically biased for the first time after thermal cycling. This creates a network of percolation paths between the electrodes, which prevents the electrical current from being funneled exclusively in a small section of the device. Therefore, the resistive switching is gradual during the first current up-sweep. This might also explain why the filament cannot be observed in the photomicrograph acquired after loop A [Fig. 2(d)].

[1] C. Mead, *Analog VLSI and Neural Systems* (Addison-Wesley Longman, Reading, MA, 1989).

[2] I. K. Schuller, R. Stevens, R. Pino, and M. Pechan, Neuromorphic computing—from materials research to systems architecture roundtable, Tech. Rep. (2015).

[3] D. V. Christensen, *et al.*, 2022 Roadmap on neuromorphic computing and engineering, Neuromorphic Comput. Eng. **2**, 022501 (2022).

[4] M. Ziegler, T. Mussenbrock, and H. Kohlstedt, eds., *Bio-Inspired Information Pathways: From Neuroscience to Neurotronics*, Springer Series on Bio- and Neurosystems (Springer International Publishing, Cham, 2024), Vol. 16.

[5] D. Ielmini and H.-S. P. Wong, In-memory computing with resistive switching devices, Nat. Electron. **1**, 333 (2018).

[6] D. Ielmini, Brain-inspired computing with resistive switching memory (RRAM): Devices, synapses and neural networks, Microelectron. Eng. **190**, 44 (2018).

[7] M. Ziegler, Ch. Wenger, E. Chicca, and H. Kohlstedt, Tutorial: Concepts for closely mimicking biological learning with memristive devices: Principles to emulate cellular forms of learning, J. Appl. Phys. **124**, 152003 (2018).

[8] Y. Ran, Y. Pei, Z. Zhou, H. Wang, Y. Sun, Z. Wang, M. Hao, J. Zhao, J. Chen, and X. Yan, A review of Mott insulator in memristors: The materials, characteristics, applications for future computing systems and neuromorphic computing, Nano Res. **16**, 1165 (2023).

[9] G. Zhou, Z. Wang, B. Sun, F. Zhou, L. Sun, H. Zhao, X. Hu, X. Peng, J. Yan, H. Wang, W. Wang, J. Li, B. Yan, D. Kuang, Y. Wang, L. Wang, and S. Duan, Volatile and non-volatile memristive devices for neuromorphic computing, Adv. Electron. Mater. **8**, 2101127 (2022).

[10] M. D. Pickett, A scalable neuristor built with Mott memristors, Nat. Mater. **12**, 114 (2012).

[11] M. Ignatov, M. Ziegler, M. Hansen, A. Petraru, and H. Kohlstedt, A memristive spiking neuron with firing rate coding, Front. Neurosci. **9**, 376 (2015).

[12] P. Stoliar, J. Tranchant, B. Corraze, E. Janod, M. P. Besland, F. Tesler, M. Rozenberg, and L. Cario, A leaky-integrate-and-fire neuron analog realized with a Mott insulator, Adv. Funct. Mater. **27**, 1604740 (2017).

[13] W. Yi, K. K. Tsang, S. K. Lam, X. Bai, J. A. Crowell, and E. A. Flores, Biological plausibility and stochasticity in scalable VO_2 active memristor neurons, Nat. Commun. **9**, 4661 (2018).

[14] J. del Valle, P. Salev, Y. Kalcheim, and I. K. Schuller, A caloritronics-based Mott neuristor, Sci. Rep. **10**, 4292 (2020).

[15] M. Ziegler, C. Riggert, M. Hansen, T. Bartsch, and H. Kohlstedt, Memristive Hebbian plasticity model: Device requirements for the emulation of Hebbian plasticity based on memristive devices, IEEE Trans. Biomed. Circuits Syst. **9**, 197 (2015).

[16] M. Hansen, F. Zahari, M. Ziegler, and H. Kohlstedt, Double-barrier memristive devices for unsupervised learning and pattern recognition, Front. Neurosci. **11**, 91 (2017).

[17] G. W. Burr, R. M. Shelby, A. Sebastian, S. Kim, S. Kim, S. Sidler, K. Virwani, M. Ishii, P. Narayanan, A. Fumarola, L. L. Sanches, I. Boybat, M. Le Gallo, K. Moon, J. Woo, H. Hwang, and Y. Leblebici, Neuromorphic computing using non-volatile memory, Adv. Phys.: X **2**, 89 (2017).

[18] D. S. Jeong and C. S. Hwang, Nonvolatile memory materials for neuromorphic intelligent machines, Adv. Mater. **30**, 1704729 (2018).

[19] J. del Valle, J. G. Ramirez, M. J. Rozenberg, and I. K. Schuller, Challenges in materials and devices for resistive-switching-based neuromorphic computing, J. Appl. Phys. **124**, 211101 (2018).

[20] R. Dittmann, S. Menzel, and R. Waser, Nanoionic memristive phenomena in metal oxides: The valence change mechanism, Adv. Phys. **70**, 155 (2021).

[21] A. Hoffmann, S. Ramanathan, J. Grollier, A. D. Kent, M. J. Rozenberg, I. K. Schuller, O. G. Shpyrko, R. C. Dynes, Y. Fainman, A. Frano, E. E. Fullerton, G. Galli, V. Lomakin, S. P. Ong, A. K. Petford-Long, J. A. Schuller, M. D. Stiles, Y. Takamura, and Y. Zhu, Quantum materials for energy-efficient neuromorphic computing: Opportunities and challenges, APL Mater. **10**, 070904 (2022).

[22] U. S. Goteti, I. A. Zaluzhnyy, S. Ramanathan, R. C. Dynes, and A. Frano, Low-temperature emergent neuromorphic networks with correlated oxide devices, Proc. Natl. Acad. Sci. **118**, e2103934118 (2021).

[23] M. Imada, A. Fujimori, and Y. Tokura, Metal-insulator transitions, Rev. Mod. Phys. **70**, 1039 (1998).

[24] S. Catalano, M. Gibert, J. Fowlie, J. Íñiguez, J.-M. Triscone, and J. Kreisel, Rare-earth nickelates $RNiO_3$: Thin films and heterostructures, Rep. Progr. Phys. **81**, 046501 (2018).

[25] V. Bisogni, S. Catalano, R. J. Green, M. Gibert, R. Scherwitzl, Y. Huang, V. N. Strocov, P. Zubko, S. Balandeh, J.-M. Triscone, G. Sawatzky, and T. Schmitt, Ground-state oxygen holes and the metal–insulator transition in the negative charge-transfer rare-earth nickelates, Nat. Commun. **7**, 13017 (2016).

[26] S. Johnston, A. Mukherjee, I. Elfimov, M. Berciu, and G. A. Sawatzky, Charge disproportionation without charge transfer in the rare-earth-element nickelates as a possible mechanism for the metal-insulator transition, Phys. Rev. Lett. **112**, 106404 (2014).

[27] C. N. Berglund, Thermal filaments in vanadium dioxide, IEEE Trans. Electron Devices **16**, 432 (1969).

[28] A. Zimmers, L. Aigouy, M. Mortier, A. Sharoni, S. Wang, K. G. West, J. G. Ramírez, and I. K. Schuller, Role of thermal heating on the voltage induced insulator-metal transition in VO_2, Phys. Rev. Lett. **110**, 056601 (2013).

[29] S. Kumar, M. D. Pickett, J. P. Strachan, G. Gibson, Y. Nishi, and R. S. Williams, Local temperature redistribution and structural transition during Joule-heating-driven conductance switching in VO_2, Adv. Mater. **25**, 6128 (2013).

[30] S. Guénon, S. Scharinger, S. Wang, J. G. Ramírez, D. Koelle, R. Kleiner, and I. K. Schuller, Electrical breakdown in a V_2O_3 device at the insulator-to-metal transition, Europhys. Lett. (EPL) **101**, 57003 (2013).

[31] N. Manca, T. Kanki, H. Tanaka, D. Marré, and L. Pellegrino, Influence of thermal boundary conditions on the current-driven resistive transition in VO_2 microbridges, Appl. Phys. Lett. **107**, 143509 (2015).

[32] M. Lange, S. Guénon, Y. Kalcheim, T. Luibrand, N. M. Vargas, D. Schwebius, R. Kleiner, I. K. Schuller, and D. Koelle, Imaging of electrothermal filament formation in a Mott insulator, Phys. Rev. Appl. **16**, 054027 (2021).

[33] R. Rocco, J. del Valle, H. Navarro, P. Salev, I. K. Schuller, and M. Rozenberg, Exponential escape rate of filamentary incubation in Mott spiking neurons, Phys. Rev. Appl. **17**, 024028 (2022).

[34] T. Luibrand, A. Bercher, R. Rocco, F. Tahouni-Bonab, L. Varbaro, C. W. Rischau, C. Dominguez, Y. Zhou, W. Luo, S. Bag, L. Fratino, R. Kleiner, S. Gariglio, D. Koelle, J.-M. Triscone, M. J. Rozenberg, A. B. Kuzmenko, S. Guénon, and J. del Valle, Characteristic length scales of the electrically induced insulator-to-metal transition, Phys. Rev. Res. **5**, 013108 (2023).

[35] J. del Valle, P. Salev, F. Tesler, N. M. Vargas, Y. Kalcheim, P. Wang, J. Trastoy, M.-H. Lee, G. Kassabian, J. G. Ramírez, M. J. Rozenberg, and I. K. Schuller, Subthreshold firing in Mott nanodevices, Nature **569**, 388 (2019).

[36] C. Adda, M.-H. Lee, Y. Kalcheim, P. Salev, R. Rocco, N. M. Vargas, N. Ghazikhanian, C.-P. Li, G. Albright, M. Rozenberg, and I. K. Schuller, Direct observation of the electrically triggered insulator-metal transition in V_3O_5 far below the transition temperature, Phys. Rev. X **12**, 011025 (2022).

[37] S. K. Das, S. K. Nandi, C. V. Marquez, A. Rúa, M. Uenuma, E. Puyoo, S. K. Nath, D. Albertini, N. Baboux, T. Lu, Y. Liu, T. Haeger, R. Heiderhoff, T. Riedl, T. Ratcliff, and R. G. Elliman, Physical origin of negative differential resistance in V_3O_5 and its application as a solid-state oscillator, Adv. Mater. **35**, 2208477 (2023).

[38] M. J. Rozenberg, I. H. Inoue, and M. J. Sánchez, Nonvolatile memory with multilevel switching: A basic model, Phys. Rev. Lett. **92**, 178302 (2004).

[39] T. Driscoll, H.-T. Kim, B.-G. Chae, M. D. Ventra, and D. N. Basov, Phase-transition driven memristive system, Appl. Phys. Lett. **95**, 043503 (2009).

[40] H. Coy, R. Cabrera, N. Sepúlveda, and F. E. Fernández, Optoelectronic and all-optical multiple memory states in vanadium dioxide, J. Appl. Phys. **108**, 113115 (2010).

[41] S. D. Ha, G. H. Aydogdu, and S. Ramanathan, Metal-insulator transition and electrically driven memristive characteristics of $SmNiO_3$ thin films, Appl. Phys. Lett. **98**, 012105 (2011).

[42] B. Hu, Y. Zhang, W. Chen, C. Xu, and Z. L. Wang, Self-heating and External strain coupling induced phase transition of VO_2 nanobeam as single domain switch, Adv. Mater. **23**, 3536 (2011).

[43] L. Pellegrino, N. Manca, T. Kanki, H. Tanaka, M. Biasotti, E. Bellingeri, A. S. Siri, and D. Marré, Multistate memory devices based on free-standing VO_2/TiO_2 microstructures driven by Joule self-heating, Adv. Mater. **24**, 2929 (2012).

[44] K. Cai, Z. He, J. Sun, B. Li, and J. Zhou, Resistive switching in a negative temperature coefficient metal oxide memristive one-port, Appl. Phys. A **111**, 1045 (2013).

[45] J. Shi, S. D. Ha, Y. Zhou, F. Schoofs, and S. Ramanathan, A correlated nickelate synaptic transistor, Nat. Commun. **4**, 2676 (2013).

[46] G. Seo, B.-J. Kim, H.-T. Kim, and Y. W. Lee, Thermally- or optically-biased memristive switching in two-terminal VO_2 devices, Curr. Appl. Phys. **14**, 1251 (2014).

[47] T. Patel, J. Okamoto, T. Dekker, B. Yang, J. Gao, X. Luo, W. Lu, Y. Sun, and A. W. Tsen, Photocurrent imaging of multi-memristive charge density wave switching in two-dimensional 1T-TaS_2, Nano Lett. **20**, 7200 (2020).

[48] A. G. Shabalin, J. del Valle, N. Hua, M. J. Cherukara, M. V. Holt, I. K. Schuller, and O. G. Shpyrko, Nanoscale imaging and control of volatile and non-volatile resistive switching in VO_2, Small **16**, 2005439 (2020).

[49] Y. Ma, D. Wu, Y. Li, R. Chen, and C. Lu, Multiple non-volatile resistance states tuned by electric pulses in the hysteresis temperature range of 1T-TaS_2, Ann. Phys. **533**, 2000507 (2021).

[50] Y. Ma, G. Xiao, L. Du, A. Li, and D. Wu, Multiple resistance states induced by electric pulses and reset by Joule heating in the hysteresis temperature range of $(V_{0.99}Cr_{0.01})_2O_3$, Appl. Phys. Lett. **123**, 051901 (2023).

[51] G. Catalan, Progress in perovskite nickelate research, Phase Transitions **81**, 729 (2008).

[52] Y. Lu, A. Frano, M. Bluschke, M. Hepting, S. Macke, J. Strempfer, P. Wochner, G. Cristiani, G. Logvenov, H.-U. Habermeier, M. W. Haverkort, B. Keimer, and E. Benckiser, Quantitative determination of bond order and lattice distortions in nickel oxide heterostructures by resonant X-ray scattering, Phys. Rev. B **93**, 165121 (2016).

[53] J. Liu, M. Kargarian, M. Kareev, B. Gray, P. J. Ryan, A. Cruz, N. Tahir, Y.-D. Chuang, J. Guo, J. M. Rondinelli, J. W. Freeland, G. A. Fiete, and J. Chakhalian, Heterointerface engineered electronic and magnetic phases of $NdNiO_3$ thin films, Nat. Commun. **4**, 2714 (2013).

[54] S. Catalano, M. Gibert, V. Bisogni, F. He, R. Sutarto, M. Viret, P. Zubko, R. Scherwitzl, G. A. Sawatzky, T. Schmitt, and J.-M. Triscone, Tailoring the electronic transitions of $NdNiO_3$ films through $(111)_{pc}$ oriented interfaces, APL Mater. **3**, 062506 (2015).

[55] Y. E. Suyolcu, K. Fürsich, M. Hepting, Z. Zhong, Y. Lu, Y. Wang, G. Christiani, G. Logvenov, P. Hansmann, M. Minola, B. Keimer, P. A. van Aken, and E. Benckiser, Control of the metal-insulator transition in $NdNiO_3$ thin films through the interplay between structural and electronic properties, Phys. Rev. Mater. **5**, 045001 (2021).

[56] K. W. Post, A. S. McLeod, M. Hepting, M. Bluschke, Y. Wang, G. Cristiani, G. Logvenov, A. Charnukha, G. X. Ni, P. Radhakrishnan, M. Minola, A. Pasupathy, A. V. Boris, E. Benckiser, K. A. Dahmen, E. W. Carlson, B. Keimer, and D. N. Basov, Coexisting first- and second-order electronic phase transitions in a correlated oxide, Nat. Phys. **14**, 1056 (2018).

[57] M. M. Lange, S. Guénon, F. Lever, R. Kleiner, and D. Koelle, A high-resolution combined scanning laser and widefield polarizing microscope for imaging at temperatures from 4 K to 300 K, Rev. Sci. Instrum. **88**, 123705 (2017).

[58] M. M. Lange, A high-resolution polarizing microscope for cryogenic imaging: Development and application to investigations on twin walls in $SrTiO_3$ and the metal-insulator transition in V_2O_3, Ph.D. thesis, Universität Tübingen, 2018.

[59] S. Guénon, F. Tahouni-Bonab, T. Luibrand, G. Cristiani, C. Schmid, G. Logvenov, B. Keimer, R. Kleiner, and D. Koelle, Data for "Non-volatile multi-state electrothermal resistive switching in a strongly correlated insulator thin-film device", https://doi.org/10.5281/zenodo.16637405 (2025).

[60] B. Gross, S. Guénon, J. Yuan, M. Y. Li, J. Li, A. Ishii, R. G. Mints, T. Hatano, P. H. Wu, D. Koelle, H. B. Wang, and R. Kleiner, Hot-spot formation in stacks of intrinsic Josephson junctions in $Bi_2Sr_2CaCu_2O_8$, Phys. Rev. B **86**, 094524 (2012).

Publication 3

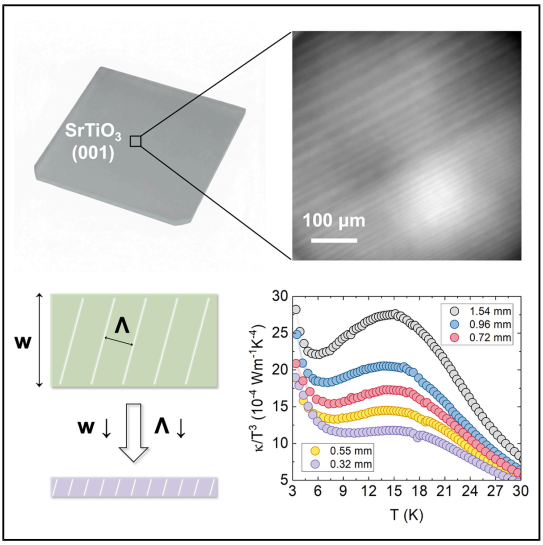
Reproduced from
S. Guo *et al.*, Newton **2**, 100407 (2026)
© 2026 The Author(s). Published by Elsevier Inc.

Newton

Article

Domain-wall-driven anomaly in hydrodynamic phonon transport in $SrTiO_3$

Graphical abstract



Highlights

- Millimeter-scale size-dependent hydrodynamic phonon transport is observed in $SrTiO_3$
- Ferroelastic domain walls act as dominant internal boundaries for phonon scattering
- Optical microscopy shows domain wall density increases as sample width decreases
- Domain wall engineering enables macroscopic control of viscous-like heat flow

Authors

Shucheng Guo, Farnaz Tahouni-Bonab, Jinchen Han, ..., Stefan Guénon, Sangyeop Lee, Xi Chen

Correspondence

sylee@pitt.edu (S.L.),
xichen@ucr.edu (X.C.)

In brief

Pronounced size effects in hydrodynamic phonon transport are typically confined to the micrometer scale. Guo et al. show that, in $SrTiO_3$, ferroelastic domain walls generate an anomalous millimeter-scale size dependence. By narrowing the sample width, they reveal that increased domain wall density progressively suppresses phonon Poiseuille flow, identifying domain wall engineering as a powerful strategy for tailoring hydrodynamic heat transport at cryogenic temperatures.

Guo et al., 2026, Newton 2, 100407
June 1, 2026 © 2026 The Author(s). Published by Elsevier Inc.
https://doi.org/10.1016/j.newton.2026.100407

CellPress

Please cite this article in press as: Guo et al., Domain-wall-driven anomaly in hydrodynamic phonon transport in $SrTiO_3$, Newton (2026), https://doi.org/10.1016/j.newton.2026.100407

Newton

CellPress
OPEN ACCESS

Article

Domain-wall-driven anomaly in hydrodynamic phonon transport in $SrTiO_3$

Shucheng Guo,[1,6] Farnaz Tahouni-Bonab,[2,6] Jinchen Han,[3,6] Jiaming He,[4] Thomas Hoke,[1] Dieter Koelle,[2] Reinhold Kleiner,[2] Jianshi Zhou,[4] Stefan Guénon,[2] Sangyeop Lee,[3,*] and Xi Chen[1,5,7,*]

[1]Department of Electrical and Computer Engineering, University of California, Riverside, Riverside, CA 92521, USA
[2]Physikalisches Institut, Center for Quantum Science (CQ) and LISA+, Eberhard Karls Universität Tübingen, Auf der Morgenstelle 14, 72076 Tübingen, Germany
[3]Department of Mechanical Engineering and Materials Science, University of Pittsburgh, Pittsburgh, PA 15261, USA
[4]Materials Science and Engineering Program, Department of Mechanical Engineering, University of Texas at Austin, Austin, TX 78712, USA
[5]Materials Science and Engineering Program, University of California, Riverside, Riverside, CA 92521, USA
[6]These authors contributed equally
[7]Lead contact
*Correspondence: sylee@pitt.edu (S.L.), xichen@ucr.edu (X.C.)
https://doi.org/10.1016/j.newton.2026.100407

ACCESSIBLE OVERVIEW Heat transport in insulating crystals is typically diffusive, dominated by random phonon scattering similar to gas molecules. However, a rare "hydrodynamic" regime exists where phonons flow collectively like a viscous fluid. While the size dependence of such fluid-like behavior is conventionally limited to micrometer scales, we demonstrate that high-purity $SrTiO_3$ breaks this expectation. By systematically reducing the crystal width from about 1.5 to 0.3 mm at fixed length and thickness, we observe a progressive suppression of key hydrodynamic signatures—specifically, the super-cubic upturn in thermal conductivity—in the 6- to 13-K window. This suggests that boundaries much smaller than the macroscopic crystal dimensions disrupt collective heat flow. Combining optical microscopy and first-principles calculations, we identify ferroelastic domain walls—internal boundaries formed below the antiferrodistortive transition—as the origin. As the crystal width decreases, these domain walls pack more densely, forming a dense internal network that scatters phonons and overrides the physical sample size as the dominant length scale. Our findings establish ferroelastic domain wall engineering as a composition-independent route to tailor collective heat flow, offering new approaches to control thermal transport in quantum materials.

SUMMARY

Hydrodynamic phonon transport, a collective viscous-like Poiseuille heat flow, is an intriguing regime in solids. Here we show that in quantum-paraelectric strontium titanate ($SrTiO_3$), this transport exhibits an anomalous millimeter-scale size dependence, unlike other materials where pronounced size effects appear only when sample dimensions approach the phonon mean free path. Narrowing high-purity crystals from 1.5 to 0.3 mm suppresses the super-cubic upturn in thermal conductivity and the Poiseuille shoulder in thermal diffusivity in the 6- to 13-K range, alongside a systematic shift of the Knudsen minimum to higher temperatures, signaling a hydrodynamic-to-ballistic crossover. Polarized optical microscopy, first-principles phonon calculations, and thermal transport analysis reveal ferroelastic domain walls—with average spacing following Kittel-Roitburd scaling—acting as dominant diffuse internal boundaries. These findings establish ferroelastic domain wall engineering as a knob for size-tailored hydrodynamic heat transport, enabling cryogenic thermal management and phononic device design.

INTRODUCTION

Phonon hydrodynamics describes a heat-transport regime where phonons move collectively like a fluid, driven by the predominance of momentum-conserving normal scattering events.[1–5] Its prototypical manifestation is phonon Poiseuille flow, which appears when the hierarchy

$$l_N \ll d \ll l_R \quad \text{(Equation 1)}$$

This is an open access article under the CC BY license (http://creativecommons.org/licenses/by/4.0/).

Please cite this article in press as: Guo et al., Domain-wall-driven anomaly in hydrodynamic phonon transport in $SrTiO_3$, Newton (2026), https://doi.org/10.1016/j.newton.2026.100407

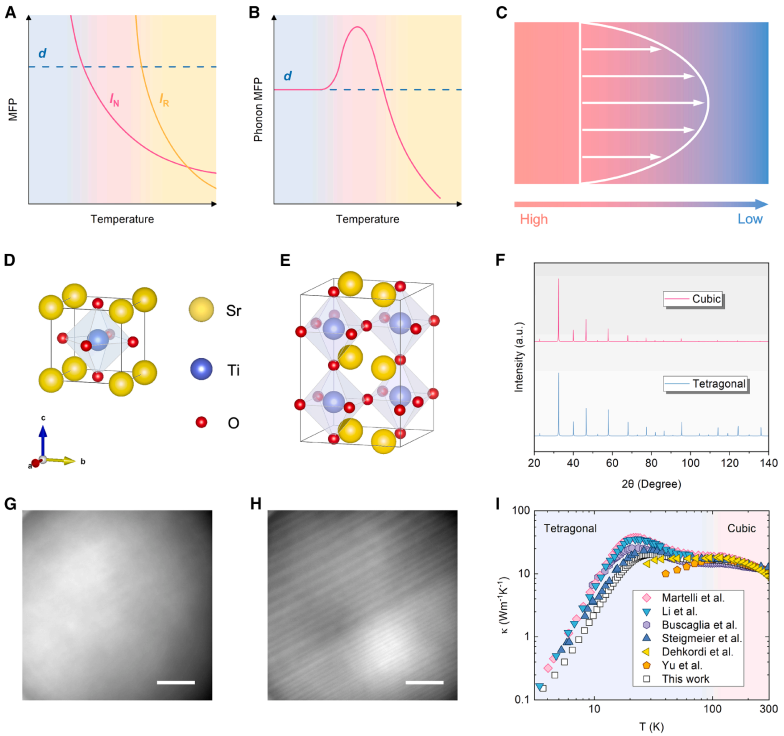


Figure 1. Overview of phonon hydrodynamics and the structural transition in $SrTiO_3$

(A) Temperature dependence of the phonon-phonon normal (l_N) and resistive Umklapp (l_R) scattering MFPs. Both increase as the temperature decreases, with l_N growing less rapidly. At sufficiently low temperatures, both exceed the sample dimension (d), indicated by the horizontal dashed line. Three transport regimes are illustrated. In the ballistic regime (blue), boundary scattering dominates. In the diffusive regime (green), Umklapp scattering dominates. In the hydrodynamic regime (red), normal scattering dominates, while boundary scattering is more frequent than Umklapp scattering.

(B) Schematic evolution of the effective phonon MFP (l_{ph}) as a function of temperature. In the hydrodynamic regime, l_{ph} can be larger than d.

(C) Steady-state heat flux profile in the hydrodynamic regime under a temperature gradient. The parabolic-like profile reflects the collective motion of phonons due to momentum-conserving normal scattering.

(D and E) Crystal structures of $SrTiO_3$ in the cubic phase (above 105 K) and tetragonal phase (below 105 K).

(F) Simulated powder XRD patterns derived from single-crystal XRD data collected at 180 K for the cubic phase and 80 K for the tetragonal phase.

(G and H) Polarized optical micrographs of the same region from a single-crystal $SrTiO_3$, taken before and after the AFD transition at 105 K. Scale bar: 100 μm.

(I) Temperature-dependent thermal conductivity of $SrTiO_3$, with the present measurements overlaid on literature-reported data.[14–19] The shaded region indicates the cubic-to-tetragonal structural transition at 105 K.

is satisfied, in which l_N is the phonon mean free path (MFP) associated with normal scattering, d denotes the characteristic sample dimension, and l_R represents the phonon MFP for resistive processes set by Umklapp and other momentum-destroying interactions (Figure 1A).[2] Within this window, normal collisions redistribute momentum among phonons more rapidly than it is dissipated into the lattice,[4–7] producing two hallmarks of phonon hydrodynamics: (1) a thermal conductivity (κ) that increases faster than the conventional cubic temperature (T^3) dependence observed in the ballistic regime[2–4] and (2) a non-monotonic effective phonon MFP (l_{ph}) whose peak value is expected to exceed d (Figure 1B).[8–11] Consequently, the heat flux profile is viscous and parabolic, directly analogous to laminar flow in classic hydrodynamics (Figure 1C).[3,12,13]

Experimental evidence of phonon hydrodynamics has been reported in several materials, ranging from graphite[20–22] and

Please cite this article in press as: Guo et al., Domain-wall-driven anomaly in hydrodynamic phonon transport in $SrTiO_3$, Newton (2026), https://doi.org/10.1016/j.newton.2026.100407

bismuth[8] to solid hydrogen[10] and helium isotopes (^{3}He and ^{4}He).[9,11] Size-dependent phonon Poiseuille flow has been detected in black phosphorus and graphite, where l_{ph} reaches hundreds of micrometers at cryogenic temperatures.[23,24] Reducing d from a scale of millimeters down to a scale of tens of micrometers significantly enhances boundary scattering and suppresses hydrodynamic phonon transport. Furthermore, by incorporating *ab initio* phonon dispersions and scattering rates into Callaway's dual relaxation time Boltzmann framework, Guo et al. demonstrated that, in the hydrodynamic regime, transverse confinement (sample width w) leads to $l_{ph} \simeq \frac{w^2}{l_N}$, whereas longitudinal confinement makes l_{ph} comparable to the sample length.[25] End-facet scattering suppresses the phonon Knudsen minimum predicted for an infinitely long graphite ribbon, and the minimum re-emerges only when the sample length exceeds w by about 5–10 times. These findings are essential for developing advanced thermal management strategies in micro- and nanoelectronics as well as for guiding the rational design of phononic devices such as thermal diodes, rectifiers, and heat-dissipating metamaterials.[26–28]

Strontium titanate ($SrTiO_3$) is a versatile platform for thermal and electronic technologies owing to its high melting point,[29] excellent thermal stability,[29] large dielectric constant,[30] and intrinsic photocatalytic activity.[31] These attributes enable its deployment in thermoelectric generators,[32] terahertz metamaterial substrates,[33] high-capacitance dielectrics,[34] and energy conversion catalysts.[35] Beyond its technological uses, $SrTiO_3$ is an ideal platform for investigating hydrodynamic phonon transport because its quantum-paraelectric lattice dynamics[36] naturally favor the required scattering hierarchy. It hosts two low-energy soft modes, a Γ-point ferroelectric transverse optical branch, and an R-point antiferrodistortive (AFD) branch and undergoes a cubic-to-tetragonal AFD transition near 105 K, where adjacent TiO_6 octahedra tilt in opposite directions (Figure 1D and 1E), breaking cubic symmetry.[37–39] These soft modes remain thermally populated to unusually low temperatures and strongly hybridize with acoustic branches, which enlarges the phase space for momentum-conserving normal scattering and shortens l_N, establishing the timescale ordering $\tau_N \ll \tau_B \ll \tau_R$ needed for hydrodynamic flow, where τ_N, τ_B, and τ_R represent the relaxation times for normal, boundary, and resistive scattering, respectively. In the vicinity of the AFD transition, the low-energy R-point branch provides an efficient Umklapp channel that sharpens the separation between ballistic, hydrodynamic, and kinetic regimes. Experimentally, low-temperature Brillouin scattering spectra revealed a doublet characteristic of second sound,[40,41] and thermal transport measurements showed a significant rise in κ surpassing the canonical T^3 dependence at low temperatures, clearly signaling the onset of phonon Poiseuille flow.[14]

Given that l_{ph} in $SrTiO_3$ is only a few microns at cryogenic temperatures,[14] its κ is expected to be largely insensitive to macroscopic variations in d. However, this presumed robustness limits the precision with which heat flux can be sculpted in hydrodynamic regimes. To date, no systematic, geometry-resolved study has quantified how phonon hydrodynamics in $SrTiO_3$ respond to deliberate changes in d. Addressing this gap is essential not only for clarifying the microscopic mechanics of momentum-conserving phonon flow in perovskite oxides but also for engineering mesoscopic architectures and quantum paraelectric devices that exploit size-tunable hydrodynamic heat transport for thermal management and energy routing.

In this work, we reveal an unconventional millimeter-scale size dependence of hydrodynamic phonon transport in $SrTiO_3$ single crystals, finding pronounced dimensional effects that persist even when d exceeds l_{ph} by several orders of magnitude. We attribute this unexpected dimensional sensitivity to ferroelastic domain wall (FDW) engineering. By systematically reducing w in the millimeter range, we observe the progressive suppression and eventual disappearance of phonon Poiseuille flow. Polarized optical microscopy shows that the average FDW spacing (average domain size, $\overline{\Lambda}$) decreases as w is reduced. Furthermore, first-principles calculations of the full phonon dispersion, combined with theoretical analysis of low-temperature ballistic transport, reveal that $\overline{\Lambda}$ follows the Kittel-Roitburd relation, $\overline{\Lambda} \propto \sqrt{w}$. Together with a w-dependent evaluation of the Umklapp activation energy in the Ziman regime, these observations are consistent with a scenario in which diffuse boundary scattering at FDWs provides the dominant resistive channel responsible for this unanticipated size effect. Our findings thus establish a direct, quantitative relationship between macroscopic crystal geometry and microscopic phonon hydrodynamics, highlighting domain wall engineering as a powerful strategy for tailoring thermal transport in quantum-paraelectric oxides.

RESULTS

To investigate the size dependence of hydrodynamic phonon transport in $SrTiO_3$, we systematically measured κ of (001)-oriented single crystals sourced from three commercial suppliers. Single-crystal X-ray diffraction (XRD) conducted at 180 and 80 K verified the cubic-to-tetragonal AFD transition (Figure 1F; Table S1). In the tetragonal phase below 105 K, polarized optical microscopy revealed multiple ferroelastic domains, typically only a few microns across (Figure 1G and 1H), consistent with previous reports.[42,43] A detailed temperature-dependent evolution of tetragonal domains from 110 to 10 K is presented in Figure S1. Figure 1F shows the measured κ of our crystal in comparison with literature data.[14–19] Previous studies by Martelli et al.,[14] Dehkordi et al.[18] and Yu et al.[19] demonstrated that even trace impurities can significantly disrupt the temperature dependence of κ in $SrTiO_3$. Thus, the close agreement between our measurements and literature data confirms the high crystalline quality of our samples.

To specifically isolate the influence of sample dimensions on thermal transport, we maintained constant effective length and thickness for each sample while systematically reducing w through mechanical polishing. Details of the sample parameters (Table S2), measurement procedures, and uncertainty analysis are provided in the supplemental information. This approach ensures that any variation in κ reflects w-dependent effects rather than other geometric factors or sample-specific inconsistencies. As shown in Figure 2A, samples with different w derived from the same parent crystal exhibit a similar temperature dependence of κ. The w-dependent κ values for two additional single crystals are presented in Figure S2. Interestingly, in the

Please cite this article in press as: Guo et al., Domain-wall-driven anomaly in hydrodynamic phonon transport in $SrTiO_3$, Newton (2026), https://doi.org/10.1016/j.newton.2026.100407

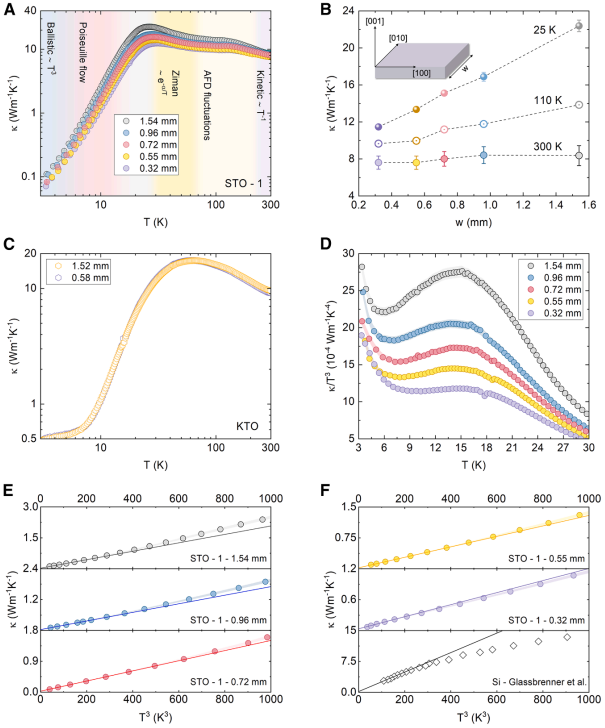


Figure 2. Suppression of hydrodynamic phonon transport driven by transverse dimensional confinement

(A) Temperature-dependent thermal conductivity of $SrTiO_3$ for samples with varying widths, plotted on a log-log scale. Distinct phonon transport regimes—ballistic (blue), Poiseuille flow (red), Ziman (yellow), AFD fluctuations (orange), and kinetic (purple)—are identified by background shading.[2,6,7]

(B) Thermal conductivity of $SrTiO_3$ at 300, 110, and 25 K as a function of w. Inset: schematic of an $SrTiO_3$ single crystal with crystallographic orientation. Error bars denote the measurement uncertainty of κ.

(C) Temperature-dependent thermal conductivity of $KTaO_3$ for samples with varying widths, plotted on a log-log scale.

(D) Thermal conductivity normalized by T^3 as a function of temperature. The shaded areas denote the estimated uncertainty of κ/T^3.

(E and F) Thermal conductivity plotted against T^3, with silicon data reported by Glassbrenner et al. used as a reference.[45] The upward deviation of thermal conductivity from linearity indicates the onset of hydrodynamic behavior. The solid lines represent linear fits to data below 6 K (ballistic regime) and are extrapolated to 10 K. These fits follow the relation $\kappa \propto T^3$. The shaded areas denote the measurement uncertainty of κ.

cubic phase (above 105 K), κ remains largely invariant across w (Figure 2B). However, upon cooling below 105 K into the tetragonal phase, a pronounced w dependence emerges, especially near 25 K (Figure 2B), accompanied by a noticeable peak shift (Figure S3). Such behavior is typically indicative of enhanced phonon-boundary scattering.[44] To eliminate experimental artifacts, we also measured κ for $KTaO_3$, a perovskite crystal without an AFD transition, and observed similar κ over the entire temperature range for two samples with different w (Figure 2C).

Below the peak temperature, a noticeable shoulder feature appears in the $\frac{\kappa}{T^3}$ plots (Figures 2D and S4). Within the narrow window between 6 and 13 K, previously identified as the Poiseuille regime in $SrTiO_3$,[14] $\frac{\kappa}{T^3}$ exhibits an upturn. This indicates that κ grows faster than T^3, a hallmark of phonon hydrodynamics.[2–4] As w decreases, this shoulder is progressively suppressed and eventually vanishes. To explicitly visualize hydrodynamic phonon behavior, we plot κ against T^3 below 10 K for samples with different w (Figures 2E and S5). In wider samples, κ rises faster than T^3, indicative of phonon Poiseuille flow. As w narrows, the scaling exponent gradually approaches the ballistic limit ($\kappa \propto T^3$) and ultimately falls below that trend at still smaller w (Figure 2F). This downward deviation mirrors the non-hydrodynamic transport reported for silicon,[45] suggesting that dimensional confinement suppresses phonon hydrodynamics in $SrTiO_3$.

To elucidate this w-dependent phenomenon, we measured the specific heat (C) of $SrTiO_3$, which closely matches reported data below 50 K (Figure S6) and evolves faster than T^3 in the Poiseuille regime (Figure 3A). Because $SrTiO_3$ is an insulator, κ is primarily governed by phonons, expressed as[46]

$$\kappa = \frac{1}{3} C \langle v \rangle l_{ph}, \qquad \text{(Equation 2)}$$

where $\langle v \rangle$ denotes the average phonon velocity (details are provided in the supplemental information). To isolate the intrinsic phonon transport characteristics from the impact of C, thermal diffusivity D_{th} was calculated as

$$D_{th} = \frac{\kappa}{C\rho}, \qquad \text{(Equation 3)}$$

where ρ is the mass density of $SrTiO_3$. Figures 3B and S7 reveal that D_{th} exhibits a non-monotonic temperature dependence, another hallmark of phonon Poiseuille flow.[8–11] Specifically, it features a pronounced local minimum, known as the Knudsen minimum, which delineates the transition from ballistic to Poiseuille transport and is followed by a distinct maximum. Notably, as w

Please cite this article in press as: Guo et al., Domain-wall-driven anomaly in hydrodynamic phonon transport in $SrTiO_3$, Newton (2026), https://doi.org/10.1016/j.newton.2026.100407

CellPress
OPEN ACCESS

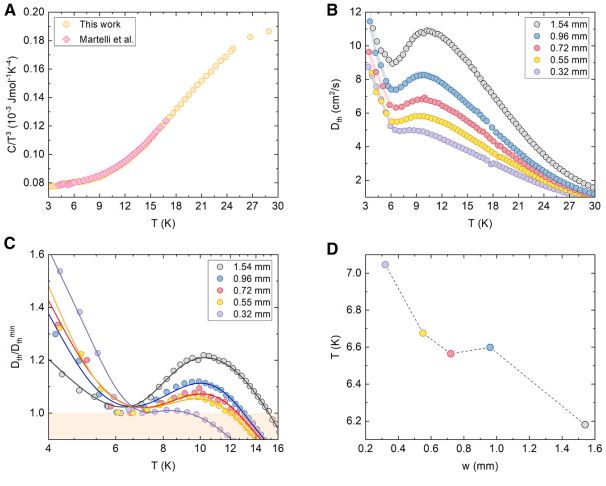


Figure 3. Evolution of thermal diffusivity and the Knudsen minimum across the hydrodynamic-to-ballistic crossover

(A) Specific heat normalized by T^3 as a function of temperature, showing excellent agreement with literature data from Martelli et al.[14]

(B) Thermal diffusivity as a function of temperature, with a local maximum serving as a hallmark of Poiseuille heat transport. The shaded areas denote the estimated uncertainty of D_{th}.

(C) Thermal diffusivity normalized by its minimum value (the Knudsen minimum) for samples with varying widths. The solid lines represent the variation trends.

(D) Temperature corresponding to the Knudsen minimum as a function of w.

decreases, this non-monotonic behavior gradually weakens, transitioning into a purely monotonic decline that signifies the suppression and eventual disappearance of phonon Poiseuille flow.

To further illustrate this evolution, Figures 3C and S8 present D_{th} normalized by its minimum value D_{th}^{min}. The resulting curves clearly show a progressive suppression of the non-monotonic temperature profile with decreasing w. Simultaneously, the Knudsen minimum shifts systematically toward higher temperatures as w narrows (Figure 3D). Similar behavior has been reported in black phosphorus and bismuth, attributed to the competition between enhanced diffuse boundary scattering, arising from the reduced characteristic d and momentum-conserving normal scattering.[8,23] However, in those studies, d ranged from approximately 0.5 mm down to tens of micrometers, values comparable to l_{ph}, making boundary scattering significant. In contrast, l_{ph} in $SrTiO_3$ is only a few micrometers,[14] whereas our samples span hundreds of micrometers. This significant scale disparity suggests that boundary effects should, in principle, be negligible; yet, pronounced dimension-dependent changes in phonon heat transport are still observed.

Initially, impurity incorporation and the redox-driven formation of oxygen vacancies introduced during mechanical polishing were considered as potential artifacts. These perturbations disrupt the centrosymmetric cubic lattice of $SrTiO_3$, thereby activating forbidden Raman modes and inducing strain-mediated frequency shifts and spectral broadening.[47–49] Concurrently, visible-light absorption by Ti^{3+} polarons and d-d transitions of multivalent dopants (e.g., Fe, Mn, Co, and Ni) can tint an otherwise colorless crystal from pale blue to yellow-brown or even black.[50,51] However, Raman spectroscopy indicates no discernible differences between unpolished and polished samples, and all crystals retain their intrinsic optical transparency with no noticeable color change after polishing (Figures S9A and S9B). Consistent with this, the measured Seebeck coefficient is indistinguishable between unpolished and polished samples (Figure S9C), whereas any substantial polishing-induced change in bulk oxygen-vacancy or aliovalent-impurity concentration would be expected to modify the carrier concentration and, hence, this quantity. Furthermore, prior studies have demonstrated that even ultra-low levels of impurities completely eliminate the characteristic κ peak near 25 K and the anomaly associated with AFD fluctuations around 100 K.[14,18,19] In our samples, XRD confirms single-phase $SrTiO_3$ with no additional peaks or detectable broadening after polishing (Figure S9D), and all κ curves retain a pronounced low-temperature peak and clear AFD-related features (Figures 2A and S2). Thus, a dominant bulk-doping scenario is strongly disfavored.

In addition, Ding et al. showed that dislocations introduced by mechanical processing in single-crystal $SrTiO_3$ are generally confined to a near-surface damage layer with a thickness of around 3 μm.[52] These near-surface defects can strongly affect surface-sensitive techniques such as time-domain thermoreflectance (TDTR) and can suppress κ by more than 50% over a broad temperature range of 80–400 K rather than only at low temperatures. However, these dislocations are not expected to have a significant impact on bulk measurements on millimeter-scale crystals. In our measurements, a pronounced size effect is observed only at low temperatures below the AFD transition, whereas at higher temperatures, the κ values for samples with different w are nearly identical (Figures 2A, 2B, and S2). Such strong dislocation-induced scattering is therefore not evident in our samples. Moreover, the control experiment on $KTaO_3$ also indicates that mechanical polishing alone does not induce a size-dependent κ (Figure 2C). Taken together, these results strongly support the conclusion that the observed size-dependent hydrodynamic phonon transport in $SrTiO_3$ originates from the formation of micron-scale tetragonal domains below the AFD transition at 105 K rather than from polishing-induced defects.

We therefore measured the FDW spacing (domain size, Λ) in two $SrTiO_3$ single crystals using low-temperature polarized optical

Please cite this article in press as: Guo et al., Domain-wall-driven anomaly in hydrodynamic phonon transport in $SrTiO_3$, Newton (2026), https://doi.org/10.1016/j.newton.2026.100407

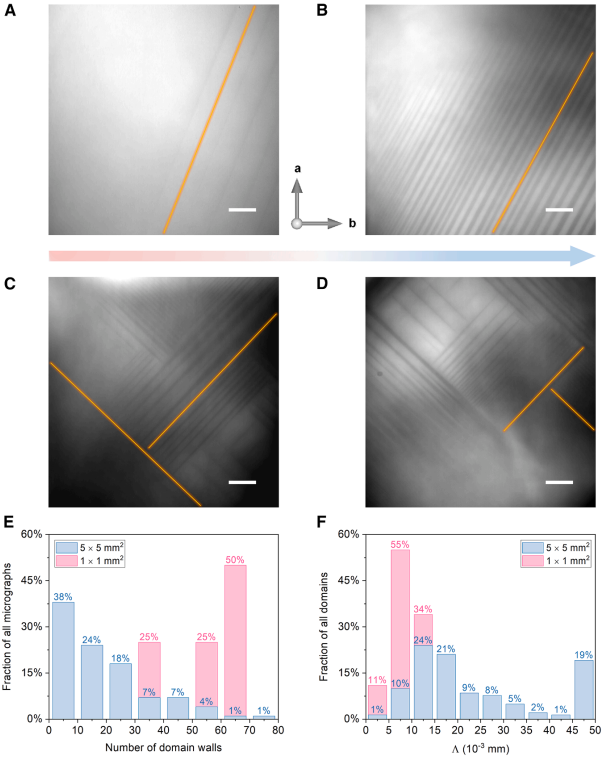


Figure 4. Microscopic visualization of FDW scaling with sample width

(A–D) Polarized optical micrographs of a 5 × 5 × 0.5 mm^3 (001)-oriented $SrTiO_3$ single crystal at two representative regions (A and B) and after mechanically polishing to 1 × 1 × 0.5 mm^3 (C and D). Scale bar: 50 μm. All micrographs were acquired at 50 K below the AFD transition, with up along [100] (*a*-axis) and right along [010] (*b*-axis). FDWs appear as dark-gray stripes. Representative walls are traced in yellow for clarity. The horizontal red-to-blue arrow indicates the direction of phonon heat transport.

(E) Distribution of FDW counts before and after polishing. The *x*-axis shows the number of domain walls per 0.5 × 0.5 mm^2 micrograph. The *y* axis shows the fraction of micrographs with that count.

(F) Distribution of FDW spacing before and after polishing.

microscopy, first in the 5 × 5 × 0.5 mm^3 geometry and then in the 1 × 1 × 0.5 mm^3 form obtained by mechanically polishing the original crystal. The crystal is (001) oriented with edges along [100] and [010] (inset in Figure 2B). Because *a* and *b* axes remain equivalent across the transition (Table S1), changes in in-plane length and width are equivalent. In the 5 × 5 × 0.5 mm^3 geometry, Λ exhibits substantial spatial heterogeneity, varying by more than an order of magnitude across the sample (Figures 4A, 4B, S10, and S11); Λ is approximately 50 μm in Figure 4A but decreases to around 8 μm in Figure 4B. Quantitatively, more than 60% of micrographs contain fewer than 20 FDWs (areal density ≈95 mm^{-2}), and about 50% of Λ values exceed 20 μm, while 20% exceed 50 μm, giving an average spacing $\overline{\Lambda} \approx$ 20 μm (Figure 4E and 4F). In the 1 × 1 × 0.5 mm^3 form, the FDWs become much denser and more uniformly spaced: the typical Λ is around 5 μm, and most neighboring walls are only 2–4 μm apart (Figures 4C, 4D, and S12). Approximately 75% of micrographs contain more than 50 FDWs (areal density ≈225 mm^{-2}), and about 70% of Λ values are below 10 μm, yielding $\overline{\Lambda} \approx$ 8 μm, roughly 1/4 of the pre-polishing value (Figure 4E and 4F). Notably, FDW traces are almost parallel to the <110> directions, consistent with previous theoretical[53] and experimental[43] studies; accordingly, phonon heat transport along [010] is oriented at ≈45° to the walls. These results establish a positive correlation between *w* and $\overline{\Lambda}$ in $SrTiO_3$; reducing *w* increases the FDW areal density and concomitantly decreases $\overline{\Lambda}$. Furthermore, thermal-cycling tests confirm that FDW formation in $SrTiO_3$ lacks spatial memory (Figure S13), consistent with previous studies,[54–56] ruling out polishing-induced removal of regions with unusually low domain wall density as the origin of the observed size dependence.

This correlation arises from the competition between the long-range elastic energy, which is associated with the spontaneous shear strains and is essentially determined by the intrinsic material properties ($E_{el} \propto \overline{\Lambda}$), and the interfacial energy of FDWs, which is governed by the in-plane dimension normal to the walls ($E_{int} \propto \frac{w}{\Lambda}$).[57,58] Minimizing the total energy, $E_{tot} = E_{el} + E_{int}$, with $\frac{\partial E_{tot}}{\partial \Lambda} = 0$ leads to the canonical Kittel-Roitburd scaling $\overline{\Lambda} \propto \sqrt{w}$.[57–59] In practice, domain wall pinning and residual strain introduce a geometry-independent offset length ($\gamma > 0$); therefore, we adopt the relation

$$\overline{\Lambda} = \beta\sqrt{w} + \gamma, \qquad \text{(Equation 4)}$$

where β is a material-dependent coefficient. Consequently, a reduction in *w* promotes finer domain patterns. Moreover, polishing exposes lateral free surfaces that relieve external clamping; it also amplifies geometry-induced strain inhomogeneity and introduces surface defects that act as pinning sites for highly

Please cite this article in press as: Guo et al., Domain-wall-driven anomaly in hydrodynamic phonon transport in $SrTiO_3$, Newton (2026), https://doi.org/10.1016/j.newton.2026.100407

CellPress
OPEN ACCESS

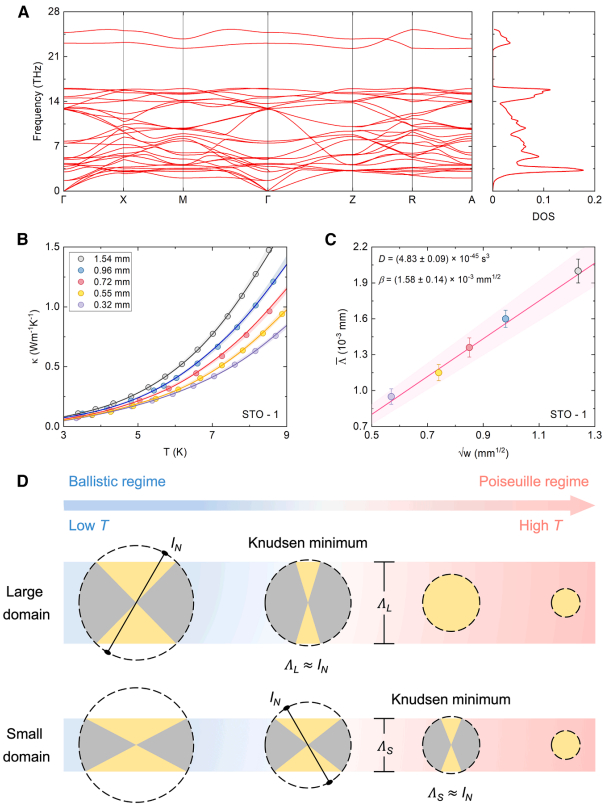


Figure 5. Phonon dispersion and transport modeling of domain wall limited hydrodynamic transport

(A) Calculated phonon dispersion curves and density of states (DOS) for $SrTiO_3$ in the tetragonal phase.

(B) Thermal conductivity of $SrTiO_3$ for samples with varying widths from 3 to 9 K. The shaded areas denote the measurement uncertainty of κ. The solid curves are the model fits.

(C) Extracted $\overline{\Lambda}$ as a function of $\sqrt{w}$. The solid pink line represents a least-squares linear fit. The shaded band is the confidence interval of the fit. Error bars denote the estimated uncertainty of $\overline{\Lambda}$.

(D) Schematic of the Knudsen minimum. When l_N (shown as dashed circles) becomes comparable to $\overline{\Lambda}$, enhanced momentum-conserving scattering leads to a local suppression of l_{ph}. This produces the Knudsen minimum in thermal diffusivity. Larger $\overline{\Lambda}$ results in a greater fraction of phonons undergoing multiple successive normal scatterings (green region), shifting the minimum to lower temperatures.

mobile domain walls.[60–62] These collective effects drive $\overline{\Lambda}$ to lower values.

To assess the impact of sample thickness, we measured the same $SrTiO_3$ single crystal with width and length held fixed, first at a thickness of 0.5 mm and then after uniform polishing to 0.18 mm. As shown in Figure S14, the κ curves remain essentially unchanged over the entire measured temperature range, which is consistent with a prior study.[14] This thickness insensitivity can be attributed to the geometry of the ferroelastic domains in (001)-oriented $SrTiO_3$; domain wall traces on the (001) surface run approximately parallel to the <110> directions, while the walls themselves are {110}-type planes that traverse the sample thickness. Polishing along the [010] width direction therefore reduces the in-plane dimension normal to the walls and perturbs the Kittel-Roitburd balance, decreasing $\overline{\Lambda}$, whereas polishing along the [001] thickness direction leaves the in-plane dimensions unchanged and has little effect on the domain configuration. Consequently, finite thickness does not set the limiting size for phonon Poiseuille flow, which is consistent with our conclusion that mechanical polishing does not, by itself, generate size-dependent hydrodynamic behavior.

Although FDWs in $SrTiO_3$ are crystallographically coherent, previous experimental and theoretical studies indicate that they are not acoustically transparent. FDWs host large strain gradients and octahedral tilt variations and can become polar at low temperatures, leading to enhanced acoustic damping and elastic softening.[63,64] Such strain and order parameter gradients are expected to provide channels for mode conversion and dephasing, so heat-carrying phonons experience FDWs as effective internal interfaces with partially diffuse reflection rather than perfectly specular mirrors. Similar behavior has been reported in other ferroic materials, such as $BiFeO_3$ and $ErMnO_3$, where coherent walls exhibit high thermal resistance.[65,66] Furthermore, prior hydrodynamic and transport studies on millimeter-scale $SrTiO_3$ single crystals indicate that FDWs play a central role in limiting phonon transport. Martelli et al. stated that the AFD transition in $SrTiO_3$ produces micrometer-scale ferroelastic domains whose walls act as internal boundaries and thereby reduce the ballistic l_{ph} from the macroscopic sample dimension to the micron-scale domain size.[14] Li et al. reported that AFD-induced domains play a crucial role in the phonon thermal Hall effect.[15] A more detailed discussion is provided in the supplemental information.

To analyze the thermal transport in $SrTiO_3$, we first obtained the full phonon dispersion (Figure 5A) from first-principles

calculations (see supplemental information for details).[67] Using the resulting phonon frequencies (ω) and mode-resolved group velocities (Table S3), we fitted κ below the Knudsen minimum with a Debye-Callaway model for phonon transport:[68,69]

$$\kappa = \frac{k_B}{2\pi^2\langle v\rangle}\left(\frac{k_B T}{\hbar}\right)^3 \int_0^{\theta_D/T} \frac{x^4 e^x}{\tau_{ph}^{-1}(e^x-1)^2}\,dx, \quad \text{(Equation 5)}$$

where $x = \frac{\hbar\omega}{k_B T}$, k_B is the Boltzmann constant, $\hbar$ denotes the reduced Planck constant, and θ_D represents the Debye temperature (Table S3). The total phonon relaxation rate is modeled as[69–71]

$$\tau_{ph}^{-1} = \tau_D^{-1} + \tau_U^{-1} + \tau_B^{-1}, \quad \text{(Equation 6)}$$

$$\tau_D^{-1} = D\omega^4, \quad \text{(Equation 7)}$$

$$\tau_B^{-1} = \frac{\langle v\rangle}{w} + \frac{\langle v\rangle}{\overline{\Lambda}}. \quad \text{(Equation 8)}$$

Here, D is a fitting parameter for point defect scattering, τ_D^{-1} denotes the defect scattering rate, τ_U^{-1} is the Umklapp scattering rate, and τ_B^{-1} accounts for scattering from both external surfaces and internal FDWs. At low temperatures, especially below 10 K, boundary scattering dominates, whereas the Umklapp scattering is essentially frozen out and can therefore be neglected (Figure S15). Figures 5B and S16 demonstrate excellent agreement between the fitted curves and the experimental data. The obtained fitting parameter $D = (4.83 \pm 0.09) \times 10^{-45}\ s^3$ is invariant with respect to w, further indicating that mechanical polishing preserves crystal quality. Moreover, $\overline{\Lambda}$ extracted from the fits systematically decreases with decreasing w, and the fitted $\beta_{STO\text{-}1} = (1.58 \pm 0.14) \times 10^{-3}\ mm^{1/2}$ (Figures 5C and S16). Together, these results corroborate the important role of FDW-induced boundary scattering in driving size-dependent hydrodynamic phonon transport in $SrTiO_3$.

Therefore, the non-monotonic behavior of D_{th} and the w dependence of the Knudsen minimum originate from the interplay between $\overline{\Lambda}$ and l_N. In the Poiseuille flow regime, phonon propagation resembles viscous fluid flow and the hydrodynamic phonon MFP follows:[23]

$$l_{ph} \simeq \frac{\overline{\Lambda}^2}{l_N}. \quad \text{(Equation 9)}$$

Narrower samples with smaller $\overline{\Lambda}$ force phonons to traverse shorter distances between successive diffuse events with FDWs, thereby lowering l_{ph} and D_{th}. As temperature rises, momentum-conserving normal scattering events become increasingly frequent, facilitating efficient momentum exchange among phonons. This enhanced phonon momentum exchange reduces l_N[6,13,72,73] and, thus, effectively increases l_{ph} and D_{th} until resistive mechanisms, such as Umklapp scattering, begin to dominate over boundary scattering.[6,13,59,60] Conversely, upon cooling, normal scattering diminishes and l_N increases. When l_N becomes comparable to $\overline{\Lambda}$, the flow transitions from Poiseuille to Knudsen-type ballistic transport.[74] At this crossover, illustrated as the Knudsen minimum in Figures 3B and 3C, phonons are no longer efficiently thermalized by normal scattering and increasingly experience boundary scattering. As illustrated in Figure 5D, the critical condition $\frac{\overline{\Lambda}}{l_N} = 1$ is satisfied at lower temperatures for large $\overline{\Lambda}$, causing the Knudsen minimum to shift upward as $\overline{\Lambda}$ decreases. In addition, due to the formation of FDWs, our measurements of κ do not exhibit super-ballistic w scaling as reported in other materials[20] (see supplemental information for details).

To further corroborate our findings, we examined the temperature dependence of κ in the Ziman regime, the narrow window between 33 and 66 K where normal collisions still dominate while Umklapp scattering begins to exceed boundary scattering:[2,23]

$$l_N \ll l_R \ll d. \quad \text{(Equation 10)}$$

In this regime, κ is expected to decay exponentially with temperature:[75]

$$\kappa \propto e^{-\alpha/T}, \quad \text{(Equation 11)}$$

where α is an effective activation temperature associated with the "freezing out" of Umklapp scattering.[4] As shown in Figures 6A and S18, the natural logarithm of the thermal conductivity, $ln\kappa$, exhibits nearly perfect linear dependence on T^{-1} across all samples, consistent with the predicted exponential form. This behavior confirms that Umklapp scattering serves as the dominant resistive mechanism within this temperature range. Intriguingly, the fitted α decreases progressively as w is reduced (Figures 6B and S18). To explain this anomalous w-dependent behavior, it is essential to identify the origins of Umklapp scattering in $SrTiO_3$.

Figure 6C and 6D present first-principles calculations of acoustic phonon dispersion in the tetragonal phase, including both longitudinal (LA) and transverse (TA) modes. Within the first Brillouin zone (BZ) of the I4/mcm space group, the in-plane wave vectors k_a and k_b are symmetry equivalent and follow the Γ-X direction, while the out-of-plane component k_c lies along Γ-M. At the upper bound of the Ziman regime (66 K), the typical $k_{a/b}$ of LA phonons reaches only approximately 15% of the BZ width. Since Umklapp scattering requires the creation of a phonon with a $k_{a/b}$ exceeding half the BZ width, the two initially interacting phonons must, on average, each carry at least 25% of the BZ width. Under such conditions, only a small subset of TA phonons marginally satisfies this requirement, rendering Umklapp collisions exceedingly rare. The situation is even more restrictive along the out-of-plane direction, in which virtually all acoustic branches remain below the Umklapp threshold throughout the Ziman regime, fundamentally limiting Umklapp scattering events.

Another source of Umklapp scattering arises from the AFD transition, driven by the soft transverse optic phonon mode located at the BZ corner (R point).[76–78] The frequency of this mode collapses to roughly 2 meV (20 K), making such Umklapp processes energetically accessible even at low temperatures, well below the Debye temperature.[37,79,80] Consistent with this interpretation, the fitted α values cluster around 20 K, which is comparable to the energy scale of the R-point soft mode and suggests that this mode provides the dominant microscopic channel for Umklapp collisions within the Ziman regime. Nonetheless, because this mechanism is inherently size-independent, reconciling it with the observed correlation between w and α remains challenging.

Please cite this article in press as: Guo et al., Domain-wall-driven anomaly in hydrodynamic phonon transport in $SrTiO_3$, Newton (2026), https://doi.org/10.1016/j.newton.2026.100407

CellPress
OPEN ACCESS

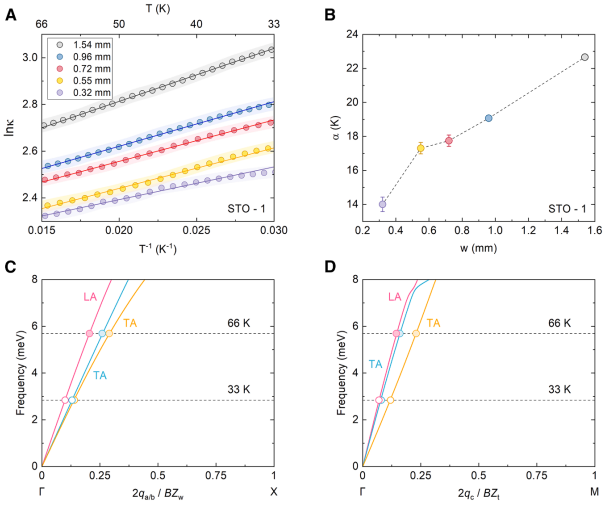


Figure 6. Impact of domain wall scattering on the Ziman regime and effective Umklapp processes

(A) Natural logarithm of thermal conductivity, $ln\kappa$, plotted as a function of T^{-1}. The solid lines represent exponential fits in the Ziman regime, following the relation $\kappa \propto e^{-\alpha/T}$. The shaded areas denote the estimated uncertainty of $ln\kappa$.

(B) Exponential fitting parameter α as a function of w, showing a clear increase with increasing w. Error bars denote the estimated uncertainty of α.

(C and D) Calculated acoustic phonon dispersions along the Γ-X and Γ-M directions in the tetragonal phase.

This apparent discrepancy can be reconciled by hypothesizing that w directly correlates with $\overline{\Lambda}$ induced by the AFD transition. Narrower samples contain a higher density of domain walls that behave as diffuse, temperature-independent scatterers, leading to smaller $\overline{\Lambda}$. These boundaries introduce an additional resistive scattering channel that, combined with Umklapp scattering, determines the effective l_R through Matthiessen's rule:[71]

$$\frac{1}{l_R} = \frac{1}{l_U} + \frac{1}{\overline{\Lambda}}, \qquad \text{(Equation 12)}$$

where l_U is the phonon MFP for Umklapp scattering. Consequently, the temperature dependence of κ becomes weaker, which is reflected in a reduced slope in the $ln\kappa$ versus T^{-1} plot, resulting in systematically smaller fitted effective activation temperatures. Therefore, as w decreases and FDW-induced boundary scattering becomes more important, the extracted α should be viewed as an effective parameter that encodes the combined influence of Umklapp and temperature-insensitive diffuse boundary scattering. It is worth noting that normal collisions, while not themselves resistive, can redistribute small-wavevector acoustic phonons into regions of the BZ where Umklapp scattering is allowed, thereby enhancing the effective Umklapp contribution.[81] A more detailed *ab initio* treatment of the interplay between normal and Umklapp processes and their relation to α would be an interesting direction for future work.

DISCUSSION

Our systematic investigation reveals a pronounced, millimeter-scale size dependence of hydrodynamic phonon transport in $SrTiO_3$ single crystals, attributable to FDW engineering. By gradually narrowing the crystals in w while maintaining constant length and thickness, we uncover an unexpected regime wherein significant size effects persist even though w remains several orders of magnitude greater than l_{ph} within the tetragonal phase. Decreasing w progressively suppresses the peak κ and quenches the Poiseuille flow-induced super-T^3 enhancement, driving κ toward a pure T^3 scaling and ultimately causing deviations below this trend. Concurrently, the characteristic non-monotonic temperature profile of D_{th} gradually transitions into monotonic decay, accompanied by a shift of the Knudsen minimum toward higher temperatures. This evolution clearly illustrates the gradual suppression and eventual disappearance of phonon Poiseuille flow.

Furthermore, a combined analysis using first-principles phonon dispersion calculations and thermal transport modeling of low-temperature ballistic transport confirms that $\overline{\Lambda}$ systematically diminishes as w is reduced, following the Kittel-Roitburd relation, $\overline{\Lambda} \propto \sqrt{w}$. This relationship arises from the competition between long-range elastic energy and domain wall interfacial energy. These results indicate that the interplay between $\overline{\Lambda}$ and l_N drives the upward shift of the Knudsen minimum, which marks the transition from Poiseuille flow to Knudsen-type ballistic transport.

Collectively, our findings establish macroscopic geometry, mediated through FDW density, as a critical control parameter for tuning hydrodynamic phonon transport. Exploiting the hydrodynamic-to-kinetic crossover via strategic domain-wall engineering thus provides promising pathways for designing advanced phononic devices and enabling precise thermal management in next-generation cryogenic quantum-paraelectric platforms.

METHODS

Material and mechanical polishing

$SrTiO_3$ single crystals were obtained from SurfaceNet, MTI, and MSE Supplies. Their widths were systematically reduced by sequential mechanical polishing while maintaining their effective length and thickness. Polishing was performed using diamond lapping films (Ted Pella) with grit sizes of 30 and 15 μm for initial

coarse thinning, followed by progressively finer grit sizes of 6, 3, 1, and 0.5 μm to achieve a smooth, defect-minimized lateral surface. A micrometer-controlled lapping fixture (Ted Pella) was employed to precisely control dimensional accuracy. Throughout each polishing step, crystals were continuously flushed with anhydrous isopropanol (IPA) of ≥99.9% purity to minimize surface oxidation and effectively remove polishing debris.

Material characterization

Single-crystal XRD was employed to probe the structural transition of $SrTiO_3$. Diffraction data were collected on a Bruker D8 Venture diffractometer equipped with a Photon III detector and an IμS microfocus Mo Kα source (λ = 0.71073 Å). A block-shaped crystal was mounted on a MiTeGen pin. Unit-cell parameters were determined at temperatures ranging from 80 to 273 K with 1 s frame exposures and a detector distance of 50 mm. Raman measurements were performed at 300 K using a Horiba LabRam equipped with a 532 nm laser. Phase purity was analyzed using a PANalytical Empyrean Series 2 X-ray diffractometer (Malvern Panalytical, Malvern, UK) equipped with Cu Kα radiation (λ = 1.54 Å).

Low-temperature polarized optical microscopy was performed at the University of Tübingen to characterize FDWs in $SrTiO_3$ single crystals with dimensions of $5 \times 5 \times 0.5$ mm^3 and $1 \times 1 \times 0.5$ mm^3.[82] The evolution of ferroelastic domain structures across the AFD transition was monitored within a 0.5×0.5 mm^2 field of view by cooling the specimen to 10 K and subsequently warming it in 10 K increments up to 110 K. In addition, at a constant imaging temperature of 50 K, the intact crystal surface was scanned under near-crossed polarizers (0° and 90°) by sequentially imaging contiguous sub-areas, each measuring 0.5×0.5 mm^2. In each micrograph, FDWs were first identified using a Fourier-based stripe-analysis pipeline, and Λ was then obtained by computing the line-normal distances between neighboring walls. Representative micrographs and additional details on FDW quantification are provided in the supplemental information.

The thermal conductivity, specific heat, and Seebeck coefficient of $SrTiO_3$ single crystals were measured using a quantum design physical property measurement system (PPMS) over the temperature range of 3–300 K. Further information is available in the supplemental information.

First-principles calculations and thermal transport analysis

Full phonon dispersion of tetragonal $SrTiO_3$ was computed using first-principles calculations, and the resulting phonon frequencies and group velocities were used for thermal transport analysis of low-temperature thermal conductivity. Details are provided in the supplemental information.

RESOURCE AVAILABILITY

Lead contact

Requests for further information and resources should be directed to and will be fulfilled by the lead contact, Xi Chen (xichen@ucr.edu).

Materials availability

This study did not generate new unique materials.

Data and code availability

The raw data that support the findings of this study are available from the corresponding author upon request.

ACKNOWLEDGMENTS

This work was supported by the National Science Foundation (grant 2144328). J.H. and S.L. thank Dr. Jie Sun (University of Tokyo) and Dr. Marios Zacharias (The Cyprus Institute) for helpful discussions on phonon calculations and acknowledge support from the National Science Foundation (grant 1943807). Computational resources were provided by the University of Pittsburgh Center for Research Computing and Data (RRID:SCR_022735), including the H2P cluster supported by the National Science Foundation (award OAC-2117681).

AUTHOR CONTRIBUTIONS

S. Guo and X.C. conceived the project and designed the experiments. S. Guo, J. He, J.Z., and X.C. undertook thermal conductivity and specific heat measurements. F.T-.B., D.K., R.K., T.H., and S. Guénon conducted low-temperature polarized optical microscopy studies. J. Han and S.L. performed the theoretical calculations. S. Guo, T.H., J. Han, and X.C. wrote the manuscript with input from all authors, and X.C. supervised the project.

DECLARATION OF INTERESTS

The authors declare no competing interests.

SUPPLEMENTAL INFORMATION

Supplemental information can be found online at https://doi.org/10.1016/j.newton.2026.100407.

Received: August 1, 2025
Revised: December 10, 2025
Accepted: January 20, 2026

REFERENCES

1. Cepellotti, A., Fugallo, G., Paulatto, L., Lazzeri, M., Mauri, F., and Marzari, N. (2015). Phonon Hydrodynamics in Two-Dimensional Materials. Nat. Commun. *6*, 6400. https://doi.org/10.1038/ncomms7400.
2. Beck, H., Meier, P.F., and Thellung, A. (1974). Phonon Hydrodynamics in Solids. Phys. Stat. Sol. *24*, 11–63. https://doi.org/10.1002/pssa.2210240102.
3. Lee, S., and Li, X. (2020). Hydrodynamic Phonon Transport: Past, Present and Prospects. In Nanoscale Energy Transport (IOP Publishing), pp. 1–26. https://doi.org/10.1088/978-0-7503-1738-2ch1.
4. Machida, Y., Martelli, V., Jaoui, A., Fauqué, B., and Behnia, K. (2024). Phonon Hydrodynamics in Bulk Insulators and Semimetals. Low. Temp. Phys *50*, 574–583. https://doi.org/10.1063/10.0026323.
5. Ghosh, K., Kusiak, A., and Battaglia, J.L. (2022). Phonon Hydrodynamics in Crystalline Materials. J. Phys. Condens. Matter *34*, 323001. https://doi.org/10.1088/1361-648X/ac718a.
6. Lee, S., Broido, D., Esfarjani, K., and Chen, G. (2015). Hydrodynamic Phonon Transport in Suspended Graphene. Nat. Commun. *6*, 6290. https://doi.org/10.1038/ncomms7290.
7. Guyer, R.A., and Krumhansl, J.A. (1966). Thermal Conductivity, Second Sound, and Phonon Hydrodynamic Phenomena in Nonmetallic Crystals. Phys. Rev. *148*, 778–788. https://doi.org/10.1103/PhysRev.148.778.
8. Kopylov, V.N., and Mezhov-Deglin, L.P. (1974). Investigation of the Kinetic Coefficients of Bismuth at Helium Temperatures. Sov. Phys. JETP *38*, 357–361.

Please cite this article in press as: Guo et al., Domain-wall-driven anomaly in hydrodynamic phonon transport in $SrTiO_3$, Newton (2026), https://doi.org/10.1016/j.newton.2026.100407

9. Mezhov-Deglin, L.P. (1966). Measurement of the Thermal Conductivity of Crystalline He^4. Sov. Phys. JETP *22*, 47–56.
10. Zholonko, N.N. (2006). Poiseuille Flow of Phonons in Solid Hydrogen. Phys. Solid State *48*, 1678–1680. https://doi.org/10.1134/S1063783406090083.
11. Thomlinson, W.C. (1969). Evidence for Anomalous Phonon Excitations in Solid He^3. Phys. Rev. Lett. *23*, 1330–1332. https://doi.org/10.1103/PhysRevLett.23.1330.
12. Gurzhi, R.N. (1968). Hydrodynamic Effects in Solids at Low Temperature. Sov. Phys. Usp. *11*, 255–270. https://doi.org/10.1070/PU1968v011n02ABEH003815.
13. Li, X., and Lee, S. (2018). Role of Hydrodynamic Viscosity on Phonon Transport in Suspended Graphene. Phys. Rev. B *97*, 094309. https://doi.org/10.1103/PhysRevB.97.094309.
14. Martelli, V., Jiménez, J.L., Continentino, M., Baggio-Saitovitch, E., and Behnia, K. (2018). Thermal Transport and Phonon Hydrodynamics in Strontium Titanate. Phys. Rev. Lett. *120*, 125901. https://doi.org/10.1103/PhysRevLett.120.125901.
15. Li, X., Fauqué, B., Zhu, Z., and Behnia, K. (2020). Phonon Thermal Hall Effect in Strontium Titanate. Phys. Rev. Lett. *124*, 105901. https://doi.org/10.1103/PhysRevLett.124.105901.
16. Buscaglia, M.T., Maglia, F., Anselmi-Tamburini, U., Marré, D., Pallecchi, I., Ianculescu, A., Canu, G., Viviani, M., Fabrizio, M., and Buscaglia, V. (2014). Effect of Nanostructure on the Thermal Conductivity of La-Doped $SrTiO_3$ Ceramics. J. Eur. Ceram. Soc. *34*, 307–316. https://doi.org/10.1016/j.jeurceramsoc.2013.08.009.
17. Steigmeier, E.F. (1968). Field Effect on the Cochran Modes in $SrTiO_3$ and $KTaO_3$. Phys. Rev. *168*, 523–530. https://doi.org/10.1103/PhysRev.168.523.
18. Dehkordi, A.M., Bhattacharya, S., Darroudi, T., Karakaya, M., Kucera, C., Ballato, J., Adebisi, R., Gladden, J.R., Podila, R., Rao, A.M., et al. (2018). Optimizing Thermal Conduction in Bulk Polycrystalline $SrTiO_{3-\delta}$ Ceramics via Oxygen Non-Stoichiometry. MRS Commun. *8*, 1470–1476. https://doi.org/10.1557/mrc.2018.220.
19. Yu, C., Scullin, M.L., Huijben, M., Ramesh, R., and Majumdar, A. (2008). Thermal Conductivity Reduction in Oxygen-Deficient Strontium Titanates. Appl. Phys. Lett. *92*, 191911. https://doi.org/10.1063/1.2930679.
20. Huang, X., Guo, Y., Wu, Y., Masubuchi, S., Watanabe, K., Taniguchi, T., Zhang, Z., Volz, S., Machida, T., and Nomura, M. (2023). Observation of Phonon Poiseuille Flow in Isotopically Purified Graphite Ribbons. Nat. Commun. *14*, 2044. https://doi.org/10.1038/s41467-023-37380-5.
21. Ding, Z., Chen, K., Song, B., Shin, J., Maznev, A.A., Nelson, K.A., and Chen, G. (2022). Observation of Second Sound in Graphite over 200 K. Nat. Commun. *13*, 285. https://doi.org/10.1038/s41467-021-27907-z.
22. Jeong, J., Li, X., Lee, S., Shi, L., and Wang, Y. (2021). Transient Hydrodynamic Lattice Cooling by Picosecond Laser Irradiation of Graphite. Phys. Rev. Lett. *127*, 085901. https://doi.org/10.1103/PhysRevLett.127.085901.
23. Machida, Y., Subedi, A., Akiba, K., Miyake, A., Tokunaga, M., Akahama, Y., Izawa, K., and Behnia, K. (2018). Observation of Poiseuille Flow of Phonons in Black Phosphorus. Sci. Adv. *4*, eaat3374. https://doi.org/10.1126/sciadv.aat3374.
24. Machida, Y., Matsumoto, N., Isono, T., and Behnia, K. (2020). Phonon Hydrodynamics and Ultrahigh–Room-Temperature Thermal Conductivity in Thin Graphite. Science *367*, 309–312. https://doi.org/10.1126/science.aaz8043.
25. Guo, Y., Zhang, Z., Bescond, M., Xiong, S., Wang, M., Nomura, M., and Volz, S. (2021). Size Effect on Phonon Hydrodynamics in Graphite Microstructures and Nanostructures. Phys. Rev. B *104*, 075450. https://doi.org/10.1103/PhysRevB.104.075450.
26. Li, X., Lee, H., Ou, E., Lee, S., and Shi, L. (2022). Reexamination of Hydrodynamic Phonon Transport in Thin Graphite. J. Appl. Phys. *131*, 075104. https://doi.org/10.1063/5.0078772.
27. Huang, X., Anufriev, R., Jalabert, L., Watanabe, K., Taniguchi, T., Guo, Y., Ni, Y., Volz, S., and Nomura, M. (2024). A Graphite Thermal Tesla Valve Driven by Hydrodynamic Phonon Transport. Nature *634*, 1086–1090. https://doi.org/10.1038/s41586-024-08052-1.
28. Guo, Y., and Wang, M. (2015). Phonon Hydrodynamics and Its Applications in Nanoscale Heat Transport. Phys. Rep. *595*, 1–44. https://doi.org/10.1016/j.physrep.2015.07.003.
29. Shi, X.L., Wu, H., Liu, Q., Zhou, W., Lu, S., Shao, Z., Dargusch, M., and Chen, Z.G. (2020). $SrTiO_3$-Based Thermoelectrics: Progress and Challenges. Nano Energy *78*, 105195. https://doi.org/10.1016/j.nanoen.2020.105195.
30. Pontes, F.M., Lee, E.J.H., Leite, E.R., Longo, E., and Varela, J.A. (2000). High Dielectric Constant of $SrTiO_3$ Thin Films Prepared by Chemical Process. J. Mater. Sci. *35*, 4783–4787. https://doi.org/10.1023/A:1004816611050.
31. Xian, T., Yang, H., Di, L., Ma, J., Zhang, H., and Dai, J. (2014). Photocatalytic Reduction Synthesis of $SrTiO_3$-Graphene Nanocomposites and Their Enhanced Photocatalytic Activity. Nanoscale Res. Lett. *9*, 327. https://doi.org/10.1186/1556-276X-9-327.
32. Srivastava, D., Norman, C., Azough, F., Schäfer, M.C., Guilmeau, E., and Freer, R. (2018). Improving the Thermoelectric Properties of $SrTiO_3$-Based Ceramics with Metallic Inclusions. J. Alloys Compd. *731*, 723–730. https://doi.org/10.1016/j.jallcom.2017.10.033.
33. Dupas, C., Guillemet-Fritsch, S., Geffroy, P.M., Chartier, T., Baillergeau, M., Mangeney, J., Roux, J.F., Ganne, J.P., Marcellin, S., Degiron, A., and Akmansoy, É. (2018). High Permittivity Processed $SrTiO_3$ for Metamaterials Applications at Terahertz Frequencies. Sci. Rep. *8*, 15275. https://doi.org/10.1038/s41598-018-33251-y.
34. Ang, C., and Yu, Z. (2007). High Capacitance-Temperature Sensitivity and "Giant" Dielectric Constant in $SrTiO_3$. Appl. Phys. Lett. *90*, 202903. https://doi.org/10.1063/1.2736298.
35. Zhang, Y., Wu, X., Wang, Z.H., Peng, Y., Liu, Y., Yang, S., Sun, C., Xu, X., Zhang, X., Kang, J., et al. (2024). Crystal Facet Engineering on $SrTiO_3$ Enhances Photocatalytic Overall Water Splitting. J. Am. Chem. Soc. *146*, 6618–6627. https://doi.org/10.1021/jacs.3c12062.
36. Müller, K.A., and Burkard, H. (1979). $SrTiO_3$: An Intrinsic Quantum Paraelectric below 4 K. Phys. Rev. B *19*, 3593–3602. https://doi.org/10.1103/PhysRevB.19.3593.
37. Shirane, G., and Yamada, Y. (1969). Lattice-Dynamical Study of the 110°K Phase Transition in $SrTiO_3$. Phys. Rev. *177*, 858–863. https://doi.org/10.1103/PhysRev.177.858.
38. Hayward, S.A., and Salje, E.K.H. (1999). Cubic-Tetragonal Phase Transition in $SrTiO_3$ Revisited: Landau Theory and Transition Mechanism. Phase. Transit *68*, 501–522. https://doi.org/10.1080/01411599908224530.
39. Koga, T., Lu, Z., Munakata, K., Hatakeyama, M., Soejima, Y., and Okazaki, A. (1995). Domain Population in $SrTiO_3$ below the Cubic-to-Tetragonal Phase Transition. Phase. Transit *54*, 109–116. https://doi.org/10.1080/01411599508213221.
40. Koreeda, A., Takano, R., and Saikan, S. (2007). Second Sound in $SrTiO_3$. Phys. Rev. Lett. *99*, 265502. https://doi.org/10.1103/PhysRevLett.99.265502.
41. Hehlen, B., Pérou, A.L., Courtens, E., and Vacher, R. (1995). Observation of a Doublet in the Quasielastic Central Peak of Quantum-Paraelectric $SrTiO_3$. Phys. Rev. Lett. *75*, 2416–2419. https://doi.org/10.1103/PhysRevLett.75.2416.
42. Tao, Q., Loret, B., Xu, B., Yang, X., Rischau, C.W., Lin, X., Fauqué, B., Verstraete, M.J., and Behnia, K. (2016). Nonmonotonic Anisotropy in Charge Conduction Induced by Antiferrodistortive Transition in Metallic $SrTiO_3$. Phys. Rev. B *94*, 035111. https://doi.org/10.1103/PhysRevB.94.035111.
43. Buckley, A., Rivera, J.P., and Salje, E.K.H. (1999). Twin Structures in Tetragonal $SrTiO_3$: The Ferroelastic Phase Transition and the Formation of Needle Domains. J. Appl. Phys. *86*, 1653–1656. https://doi.org/10.1063/1.370942.

44. Thacher, P.D. (1967). Effect of Boundaries and Isotopes on the Thermal Conductivity of LiF. Phys. Rev. *156*, 975–988. https://doi.org/10.1103/PhysRev.156.975.

45. Glassbrenner, C.J., and Slack, G.A. (1964). Thermal Conductivity of Silicon and Germanium from 3°K to the Melting Point. Phys. Rev. *134*, A1058–A1069. https://doi.org/10.1103/PhysRev.134.A1058.

46. Maxwell, J.C. (1867). IV. On the Dynamical Theory of Gases. Philos. Trans. R. Soc. Lond. *157*, 49–88. https://doi.org/10.1098/rstl.1867.0004.

47. Chapron, D., Cordero, F., and Fontana, M.D. (2019). Characterization of Oxygen Vacancies in $SrTiO_3$ by Means of Anelastic and Raman Spectroscopy. J. Appl. Phys. *126*, 154101. https://doi.org/10.1063/1.5115106.

48. Tenne, D.A., Gonenli, I.E., Soukiassian, A., Schlom, D.G., Nakhmanson, S.M., Rabe, K.M., and Xi, X.X. (2007). Raman Study of Oxygen Reduced and Re-Oxidized Strontium Titanate. Phys. Rev. B *76*, 024303. https://doi.org/10.1103/PhysRevB.76.024303.

49. Dwij, V., De, B.K., Tyagi, S., Sharma, G., and Sathe, V. (2021). Fano Resonance and Relaxor Behavior in Pr Doped $SrTiO_3$: A Raman Spectroscopic Investigation. Physica. B. Condens. Matter *620*, 413265. https://doi.org/10.1016/j.physb.2021.413265.

50. Reinders, N., Luxová, J., Hroch, J., Dohnalová, Ž., and Šulcová, P. (2025). Advanced NIR-Reflective Taupe Pigments from 3d-Metal-Doped $SrTiO_3$ Ceramic Systems. Ceram. Int. *51*, 30502–30511. https://doi.org/10.1016/j.ceramint.2025.04.244.

51. Viernstein, A., Kubicek, M., Morgenbesser, M., Walch, G., Brunauer, G.C., and Fleig, J. (2019). High-Temperature Photochromism of Fe-Doped $SrTiO_3$ Caused by UV-Induced Bulk Stoichiometry Changes. Adv. Funct. Mater. *29*, 1900196. https://doi.org/10.1002/adfm.201900196.

52. Ding, J., Zhang, J., Dong, J., Higuchi, K., Nakamura, A., Lu, W., Sun, B., and Fang, X. (2025). Effective Reduction in Thermal Conductivity by High-Density Dislocations in $SrTiO_3$. Appl. Phys. Lett. *126*, 253301. https://doi.org/10.1063/5.0271392.

53. Sapriel, J. (1975). Domain-Wall Orientations in Ferroelastics. Phys. Rev. B *12*, 5128–5140. https://doi.org/10.1103/PhysRevB.12.5128.

54. Kalisky, B., Spanton, E.M., Noad, H., Kirtley, J.R., Nowack, K.C., Bell, C., Sato, H.K., Hosoda, M., Xie, Y., Hikita, Y., et al. (2013). Locally Enhanced Conductivity Due to the Tetragonal Domain Structure in $LaAlO_3/SrTiO_3$ Heterointerfaces. Nat. Mater. *12*, 1091–1095. https://doi.org/10.1038/nmat3753.

55. Frenkel, Y., Haham, N., Shperber, Y., Bell, C., Xie, Y., Chen, Z., Hikita, Y., Hwang, H.Y., Salje, E.K.H., and Kalisky, B. (2017). Imaging and Tuning Polarity at $SrTiO_3$ Domain Walls. Nat. Mater. *16*, 1203–1208. https://doi.org/10.1038/nmat4966.

56. Ma, H.J.H., Scharinger, S., Zeng, S.W., Kohlberger, D., Lange, M., Stöhr, A., Wang, X.R., Venkatesan, T., Kleiner, R., Scott, J.F., et al. (2016). Local Electrical Imaging of Tetragonal Domains and Field-Induced Ferroelectric Twin Walls in Conducting $SrTiO_3$. Phys. Rev. Lett. *116*, 257601. https://doi.org/10.1103/PhysRevLett.116.257601.

57. Roitburd, A.L. (1976). Equilibrium Structure of Epitaxial Layers. Phys. Stat. Sol. *37*, 329–339. https://doi.org/10.1002/pssa.2210370141.

58. Kittel, C. (1946). Theory of the Structure of Ferromagnetic Domains in Films and Small Particles. Phys. Rev. *70*, 965–971. https://doi.org/10.1103/PhysRev.70.965.

59. Landau, L., and Lifshitz, E. (1935). On The Theory of The Dispersion of Magnetic Permeability in Ferromagnetic Bodies. Phys. Z. Sowjetunion *8*, 153–169.

60. Pramanick, A., Prewitt, A.D., Forrester, J.S., and Jones, J.L. (2012). Domains, Domain Walls and Defects in Perovskite Ferroelectric Oxides: A Review of Present Understanding and Recent Contributions. Crit. Rev. Solid State Mater. Sci. *37*, 243–275. https://doi.org/10.1080/10408436.2012.686891.

61. Damjanovic, D. (1998). Ferroelectric, Dielectric and Piezoelectric Properties of Ferroelectric Thin Films and Ceramics. Rep. Prog. Phys. *61*, 1267–1324. https://doi.org/10.1088/0034-4885/61/9/002.

62. Prokhorenko, S., and Pertsev, N.A. (2011). Free-Standing Ferroelectric Multilayers: Crossover from Thin-Film to Bulk Behavior. J. Appl. Phys. *110*, 074116. https://doi.org/10.1063/1.3647585.

63. Schranz, W., Tröster, A., and Rychetsky, I. (2022). Signatures of Polarity in Ferroelastic Domain Walls and Antiphase Boundaries of $SrTiO_3$ and Other Perovskites. J. Alloys Compd. *890*, 161775. https://doi.org/10.1016/j.jallcom.2021.161775.

64. Scott, J.F., Salje, E.K.H., and Carpenter, M.A. (2012). Domain Wall Damping and Elastic Softening in $SrTiO_3$: Evidence for Polar Twin Walls. Phys. Rev. Lett. *109*, 187601. https://doi.org/10.1103/PhysRevLett.109.187601.

65. Hopkins, P.E., Adamo, C., Ye, L., Huey, B.D., Lee, S.R., Schlom, D.G., and Ihlefeld, J.F. (2013). Effects of Coherent Ferroelastic Domain Walls on the Thermal Conductivity and Kapitza Conductance in Bismuth Ferrite. Appl. Phys. Lett. *102*, 121903. https://doi.org/10.1063/1.4798497.

66. Belrhiti-Nejjar, R., Zahn, M., Limelette, P., Haas, M., Féger, L., Monot-Laffez, I., Horny, N., Meier, D., Giovannelli, F., Schultheiß, J., et al. (2025). Domain-Wall Driven Suppression of Thermal Conductivity in a Ferroelectric Polycrystal. Adv. Sci *12*, e06931. https://doi.org/10.1002/advs.202506931.

67. Zacharias, M., Volonakis, G., Giustino, F., and Even, J. (2023). Anharmonic Lattice Dynamics via the Special Displacement Method. Phys. Rev. B *108*, 035155. https://doi.org/10.1103/PhysRevB.108.035155.

68. Sologubenko, A.V., Giannó, K., Ott, H.R., Ammerahl, U., and Revcolevschi, A. (2000). Thermal Conductivity of the Hole-Doped Spin Ladder System $Sr_{14-x}Ca_xCu_{24}O_{41}$. Phys. Rev. Lett. *84*, 2714–2717. https://doi.org/10.1103/PhysRevLett.84.2714.

69. Callaway, J. (1959). Model for Lattice Thermal Conductivity at Low Temperatures. Phys. Rev. *113*, 1046–1051. https://doi.org/10.1103/PhysRev.113.1046.

70. Yang, J. (2004). Theory of Thermal Conductivity. In Thermal Conductivity, T.M. Tritt, ed. (Springer), pp. 1–20. https://doi.org/10.1007/0-387-26017-X_1.

71. Blatt, F.J. (2020). Matthiessen's Rule (McGraw Hill's AccessScience). https://doi.org/10.1036/1097-8542.410800.

72. Rahbar, M., Li, B., Hunter, N., Al Keyyam, I., Wang, T., Shi, E., and Wang, X. (2023). Observing Grain Boundary-Induced Phonons Mean Free Path in Highly Aligned SWCNT Bundles by Low-Momentum Phonon Scattering. Cell Rep. Phys. Sci. *4*, 101688. https://doi.org/10.1016/j.xcrp.2023.101688.

73. Regner, K.T., Sellan, D.P., Su, Z., Amon, C.H., McGaughey, A.J.H., and Malen, J.A. (2013). Broadband Phonon Mean Free Path Contributions to Thermal Conductivity Measured Using Frequency Domain Thermoreflectance. Nat. Commun. *4*, 1640. https://doi.org/10.1038/ncomms2630.

74. Mezhov-Deglin, L.P., Kopylov, V.N., and Medvedev, E.S. (1975). Contributions of Various Phonon Relaxation Mechanisms to the Thermal Resistance of the Crystal Lattice of Bismuth at Temperatures below 2°K. Sov. Phys. JETP *40*, 557–563.

75. Ziman, J.M. (2001). Electrons and Phonons: The Theory of Transport Phenomena in Solids (Oxford University Press). https://doi.org/10.1093/acprof:oso/9780198507796.001.0001.

76. Dapor, M. (2023). Scattering Mechanisms. Scattering Mechanisms. in: Transport of Energetic Electrons in Solids, *290* (Springer Tracts in Modern Physics), pp. 29–82. https://doi.org/10.1007/978-3-031-37242-1_4.

77. Rudin, S.P. (2018). Generalization of Soft Phonon Modes. Phys. Rev. B *97*, 134114. https://doi.org/10.1103/PhysRevB.97.134114.

78. Yang, R., Yue, S., and Liao, B. (2019). Hydrodynamic Phonon Transport Perpendicular to Diffuse-Gray Boundaries. Nanoscale Microscale Thermophys. Eng. *23*, 25–35. https://doi.org/10.1080/15567265.2018.1551449.

79. Vogt, H. (1995). Refined Treatment of the Model of Linearly Coupled Anharmonic Oscillators and Its Application to the Temperature Dependence of the Zone-Center Soft-Mode Frequencies of $KTaO_3$ and $SrTiO_3$. Phys. Rev. B *51*, 8046–8059. https://doi.org/10.1103/PhysRevB.51.8046.

Please cite this article in press as: Guo et al., Domain-wall-driven anomaly in hydrodynamic phonon transport in $SrTiO_3$, Newton (2026), https://doi.org/10.1016/j.newton.2026.100407

CellPress
OPEN ACCESS

80. Hehlen, B., Arzel, L., Tagantsev, A.K., Courtens, E., Inaba, Y., Yamanaka, A., and Inoue, K. (1999). Observation of the Coupling between TA and TO Modes in $SrTiO_3$ by Brillouin Scattering. Physica. B. Condens. Matter *263–264*, 627–631. https://doi.org/10.1016/S0921-4526(98)01265-4.

81. Lindsay, L., Broido, D.A., and Mingo, N. (2009). Lattice Thermal Conductivity of Single-Walled Carbon Nanotubes: Beyond the Relaxation Time Approximation and Phonon-Phonon Scattering Selection Rules. Phys. Rev. B *80*, 125407. https://doi.org/10.1103/PhysRevB.80.125407.

82. Lange, M., Guénon, S., Lever, F., Kleiner, R., and Koelle, D. (2017). A High-Resolution Combined Scanning Laser and Widefield Polarizing Microscope for Imaging at Temperatures from 4 K to 300 K. Rev. Sci. Instrum. *88*, 123705. https://doi.org/10.1063/1.5009529.

Publication 4

Reproduced from
S. Smink *et al.*, Appl. Phys. Lett. **128**, 243501 (2026)
with the permission of AIP Publishing

Applied Physics Letters

RESEARCH ARTICLE | JUNE 15 2026

History-dependent filament configuration in multiterminal electrothermal memristors

Sander Smink ✉ ; Farnaz Tahouni-Bonab ; Wander Schmitz; Daniel Janse van Rensburg ; Julian van Putten ; Lennart Cool ; Colin Evers ; Stefan Guénon ; Reinhold Kleiner ; Dieter Koelle ; Carlos M. M. Rosário ; Hans Hilgenkamp

Check for updates

Appl. Phys. Lett. 128, 243501 (2026)
https://doi.org/10.1063/5.0334989

View Online
Export Citation

Articles You May Be Interested In

Self-switching of branched multiterminal junctions: a ballistic half-adder

Appl. Phys. Lett. (September 2003)

Multipath-switching device utilizing a GaAs-based multiterminal nanowire junction with size-controlled dual Schottky wrap gates

Appl. Phys. Lett. (May 2007)

Temperature-dependent *N*-type negative differential resistance in planar $LaNiO_3/SmNiO_3/LaNiO_3$ heterojunctions

Appl. Phys. Lett. (December 2025)

15 June 2026 07:11:00



AIP Publishing

Applied Physics Letters ARTICLE pubs.aip.org/aip/apl

History-dependent filament configuration in multiterminal electrothermal memristors

Cite as: Appl. Phys. Lett. **128**, 243501 (2026); doi: 10.1063/5.0334989
Submitted: 21 March 2026 · Accepted: 18 May 2026 ·
Published Online: 15 June 2026

View Online Export Citation CrossMark

Sander Smink,[1,a] Farnaz Tahouni-Bonab,[2] Wander Schmitz,[1] Daniel Jan se van Rensburg,[1] Julian van Putten,[1] Lennart Cool,[1] Colin Evers,[1] Stefan Guénon,[2] Reinhold Kleiner,[2] Dieter Koelle,[2] Carlos M. M. Rosário,[1] and Hans Hilgenkamp[1]

AFFILIATIONS

[1]MESA+ Institute and Faculty of Science and Technology, University of Twente, P.O. Box 217, 7500 AE Enschede, The Netherlands
[2]Physikalisches Institut, Center for Quantum Science (CQ) and LISA+, Eberhard Karls Universität Tübingen, Auf der Morgenstelle 14, 72076 Tübingen, Germany

[a]Author to whom correspondence should be addressed: s.smink@utwente.nl

ABSTRACT

Electrothermal memristors operate by a resistive switching mechanism based on Joule heating. During the switching process, metallic filaments form between the electrical contacts in a highly reversible and reproducible manner. Our experiments on planar VO_2-based devices show that multiple filaments can form when several electronic terminals are involved. The configuration, position, and size of the filaments depend sensitively on the applied inputs and on their history. Because of this history dependence and the interchangeability of the terminals, these devices are promising building blocks for programmable networks with built-in local memory.

© 2026 Author(s). All article content, except where otherwise noted, is licensed under a Creative Commons Attribution (CC BY) license (https://creativecommons.org/licenses/by/4.0/). https://doi.org/10.1063/5.0334989

15 June 2026 07:11:00

The memristive effect entails a change in resistance by an input voltage or current.[1] In an electrothermal memristor (ETM), this resistance change is mediated by temperature.[2–4] Vanadium dioxide (VO_2) is the archetype of materials for ETMs[5] owing to its insulator-to-metal transition (IMT) just above room temperature.[6,7] Across the IMT, the resistance changes by up to four orders of magnitude. Applying a voltage or current causes Joule heating,[8,9] which allows switching between the insulating and the metallic states and a distribution of states in between.[10,11] Devices thus exhibit current–voltage hysteresis[12] and negative differential resistance.[13] These properties are of interest for realizing computing-in-memory devices,[12,14,15] as well as high-frequency relaxation oscillators[13,16–18] and artificial neurons.[19,20]

The electrically induced resistive switching is an avalanche process,[14,21–24] during which filaments of the metallic state are formed.[8,24–31] Such filaments are observed ubiquitously in ETMs based on various materials with an IMT.[23,24,32–34] Contrary to filaments formed by ion migration,[35,36] in ETMs, filaments form by locally exceeding the IMT temperature through Joule heating and a subsequent attraction of current to the switched (low-resistance) region. This forming process is fast (sub-ns),[37,38] local (sub-μm),[8,29] and hysteretic.[31,39] Depending on device inputs and material parameters, multiple filaments can form geometric patterns.[23,39,40] Although the origin may differ, such filament patterns are also observed after avalanche breakdown in semiconductor devices at low temperatures.[41] Adding a third electric terminal to these semiconductor devices allows creating filament-based switches, memories, and logic gates,[42] controlled by external magnetic fields.

Here, we study VO_2-based electrothermal memristors with three electric terminals. By combining optical filament imaging and electric transport measurements, we demonstrate that multiple filaments form (and collapse) between separate electrodes. Biasing two terminals tunes the configuration and strength of the filaments in a smooth, reproducible, and hysteretic manner. We anticipate that the history dependence of the filament configuration can be leveraged in emerging network architectures with built-in local memory.

We study devices based on nominally 40-nm-thick epitaxial VO_2 films grown at the University of Twente by pulsed laser deposition (PLD) on ultrasonically cleaned Al_2O_3 $(1\bar{1}02)$ substrates ($5 \times 5 \times 0.5\,mm^3$, CrysTec, GmbH). An excimer KrF laser ($\lambda = 248$ nm) ablated a sintered V_2O_3 target with a repetition frequency of 10 Hz, a fluence of $1.3 J cm^{-2}$, and a circular spot of $1.76\,mm^2$. During deposition, the substrates were kept at 400 °C in an O_2 process pressure of 1×10^{-2} mbar at ∼45 mm from the target.

© Author(s) 2026

Reflection high-energy electron diffraction (RHEED, *in situ*) and x-ray diffraction (XRD, *ex situ*) measurements reveal film growth in the $[101]_R$—or equivalently, $[001]_M$—direction, in accordance with literature.[43] Patterned Ti (4.5 nm)/Au (100 nm) contact pads were sputtered on the as-deposited films as described in Ref. 11.

The devices were imaged using a custom-built wide-field polarization microscope (WFPM), which allows simultaneous optical imaging and electrical transport measurements.[44] The setup distinguishes different sample phases through reflectivity contrast and provides an optical resolution of approximately 0.5 μm.[32–34,39,44] The photomicrographs shown were acquired during a voltage sweep and represent differential images, obtained by averaging 20 raw images (200 ms exposure time each) and subtracting the pristine-state reflectivity at each voltage point. In the images, bright regions correspond to the insulating state, while darker regions indicate the metallic phase.

Voltages and currents were applied and measured using Keithley 2400 source-measure units (SMUs), either in the WFPM or in a Janis probe station. Figure 1(a) shows the measurement configuration. The

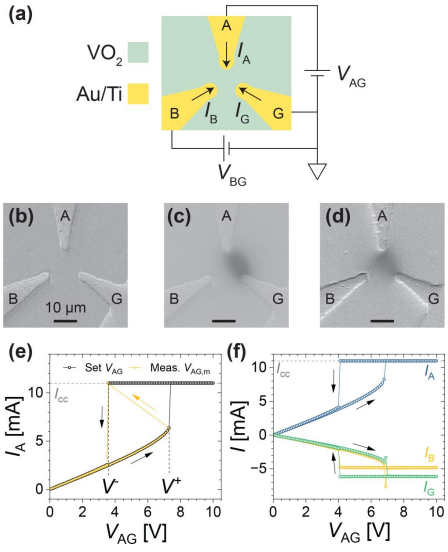


FIG. 1. Filament formation in multiterminal VO_2 devices. (a) Three-terminal device schematic with indications of material placement and electrical connections as described in the text. (b) WFPM image of a three-terminal device in its insulating state. (c) WFPM image of a metallic filament (dark region) with set $V_{AG} = 10$ V and compliance current $I_{cc} = 11$ mA. Terminal B was not connected. (d) WFPM image of multiple metallic filaments, with $V_{AG} = 10$ V, $V_{BG} = 0$ V, and $I_{cc} = 11$ mA. (e) Current through terminal A I_A measured as a function of set voltage V_{AG} (black) and of measured voltage $V_{AG,m}$ (gold) in the configuration of panel (c). The horizontal dashed line represents I_{cc}. (f) Measured I_A, I_B and inferred $I_G = -I_A - I_B$ as a function of set voltage V_{AG} for the configuration of panel (d).

SMUs were connected to terminals A and B, with setpoint voltages V_{AG} and V_{BG} defined with respect to the ground terminal G. The SMUs measured the current flowing into terminal A I_A and into terminal B I_B; the current flowing into terminal G I_G was inferred by Kirchhoff's current law $I_A + I_B + I_G = 0$. Negative values for the current reflect current flowing out of that respective terminal. A compliance current I_{cc}—equal for both SMUs—was used to limit the current flowing through the device. In compliance, the voltage across the device is adjusted accordingly and may differ from the set voltage of the SMU. Measured voltages $V_{AG,m}$ and $V_{BG,m}$ in control experiments deviated by less than 10 mV from the set value if the current was less than compliance, as shown in Fig. 1(e). All measurements were performed at room temperature. We discuss below measurements on one device, 3T12, with three terminals and an electrode spacing of 12 μm; control experiments on different devices with the same or different dimensions yielded similar results.

Figure 1(b) shows a WFPM image of the device with no voltages applied. In Fig. 1(c), a metallic filament has formed between terminals A and G while sweeping the voltage V_{AG} with terminal B disconnected. The corresponding I_A (V_{AG}) curves for upsweep and downsweep of V_{AG} are shown in Fig. 1(e). This sweep shows a nearly Ohmic behavior up to a switching voltage $V^+ = 7.3$ V, where the current jumps to compliance. Upon reducing V_{AG}, the current jumps down at another switching voltage $V^- = 3.6$ V. In compliance, the SMU maintains the actual output voltage $V_{AG,m}$ close to V^-. From Fig. 1(c), we extract a full width at half maximum of the filament $W \approx 7$ μm, which increases with compliance current. These observations compare well to the extensive literature on filament formation in two-terminal VO_2 devices.[8,24,26–31]

Connecting terminal B to ground—i.e., setting $V_{BG} = 0$ V—creates a second current channel in the device. Figure 1(f) shows that I_A is distributed almost evenly across I_B and I_G in the insulating state of the device. At V^+, two metallic filaments form simultaneously as imaged in Fig. 1(d). This formation is accompanied by concurrent jumps in the currents I_A, I_B, and I_G shown in Fig. 1(f). Both filaments, which we refer to as AG and AB after their connecting terminals, persist down to V^-, where they collapse simultaneously. In compliance, $I_G \approx -6$ mA and $I_B \approx -5$ mA, which causes the AG filament to appear wider than the AB filament in Fig. 1(d). We observe this difference consistently for repeated switching and attribute it to a contact resistance difference between terminals B and G.

Figure 2 shows how applying a nonzero V_{BG} changes the device response to a sweep of V_{AG}. V_{BG} was set to 0 V between subsequent measurements, which were taken with intervals in V_{BG} of 0.1 V. We observed six qualitatively different responses in different regimes of set V_{BG}. In regime I, where $V_{BG} = 0$ V, two filaments form and collapse simultaneously, as discussed above and shown in Figs. 1(d) and 1(f).

Regime II spans from $V_{BG} = 0.1$ to 2.9 V, in which the device responds as shown in Fig. 2(a). Initially, this situation (depicted: $V_{BG} = 0.1$ V) is similar to that discussed above for $V_{BG} = 0$ V. The magnitude of the currents and the WFPM image show that the entire device is in the insulating state. At the switching voltage $V^+ = 7.2$ V, we observe that only an AG filament has formed. This observation implies that applying a small V_{BG} prevents forming an AB filament by sweeping V_{AG}. A finite V_{BG} lowers the potential difference between terminals A and B $V_{AB} = V_{AG} - V_{BG}$ and accordingly, the current flowing

15 June 2026 07:11:00

© Author(s) 2026

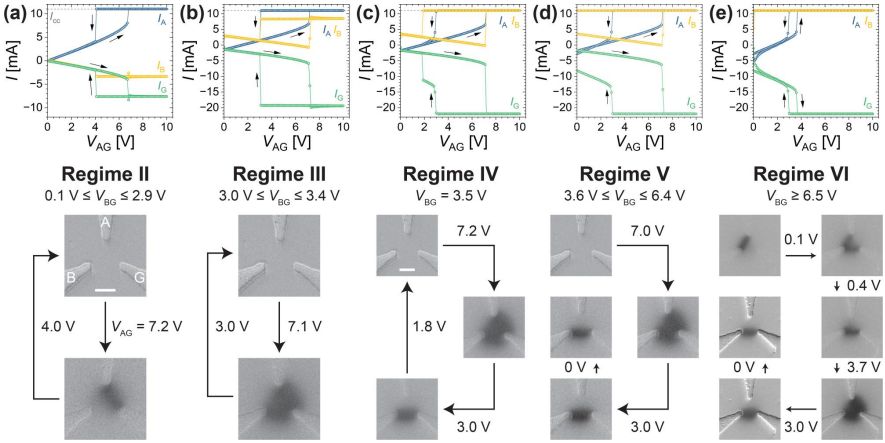


FIG. 2. Voltage-tunable filament geometry. Top panels: measured currents I_A, I_B, I_G—flowing into terminals A, B, and G, respectively—as a function of set voltage on terminal A V_{AG}, with $I_{cc} = 11$ mA. Bottom panels: WFPM images obtained during the voltage sweeps shown in the top panels. Scale bars, 10 μm. The arrows indicate transitions at given values of V_{AG}. The different regimes are discussed in the text. Data shown were taken at the lower boundaries in set voltage V_{BG} of each regime: (a) 0.1 V, (b) 3.0 V, (c) 3.5 V, (d) 3.6 V, and (e) 6.5 V.

between these terminals. Joule heating is thus suppressed close to terminal B, and a filament does not form there.

Regime III spans from $V_{BG} = 3.0$ to 3.4 V, in which the device responds as shown in Fig. 2(b). Here, inducing an AG filament at $V^+ = 7.1$ V triggers the formation a BG filament, which collapses simultaneously when sweeping V_{AG} back below $V^- = 3.0$ V. After switching, the dark (metallic) region extends beyond the electrode tips, connecting all terminals. This extension is less pronounced in the top left, where an AB filament would form. Because Joule heating is suppressed between terminals A and B, as discussed above, we do not expect an AB filament to form at all. The observations below support that scenario.

Regime IV consists of one value of V_{BG}, 3.5 V. Again, at V^+, both an AG and a BG filament form, but upon sweeping back V_{AG}, the filaments collapse at two different V^-. After the AG filament switches back, V_{AG} still provides some Joule heating, which helps sustain the BG filament. Unlike regimes II and III, I_A does not switch back to its pristine curve when the AG filament collapses but remains slightly above it until the BG filament collapses. We attribute this behavior to (i) the overlap of the BG filament with the current path from A to G and (ii) the BG filament increasing the overall device temperature, which lowers the resistance of the insulating region.

Regime V spans from $V_{BG} = 3.6$ to 6.4 V, in which the device responds as shown in Fig. 2(d). Compared to regime IV, the BG filament persists down to $V_{AG} = 0$ V. At $V_{AG} = 0$ V, the filament is narrower than just after the switch at $V_{AG} = 3.0$ V due to reduced Joule heating of the total device. This configuration is persistent as long as V_{BG} is kept above its switching-back voltage V^-.

Finally, in regime VI, $V_{BG} \geq 6.5$ V forms an AB filament already for $V_{AG} = 0$ V. The absence of a BG filament here is likely due to differences in contact resistance between the AB and BG paths as discussed above. Applying V_{AG} of only 0.1 V forms a BG filament in addition by redirecting the current flow away from terminal A and toward terminal G. Further increasing V_{AG} beyond 0.4 V causes the AB filament to collapse. Only the BG filament remains up to $V_{AG} = 3.7$ V, at which an AG filament forms as well and both SMUs reach compliance. Sweeping back V_{AG} below 3.0 V causes the AG filament to collapse. Only the BG filament is observed down to $V_{AG} = 0$ V.

Figure 3 shows how each current, I_A, I_B, and I_G, depends on V_{AG} for various values of V_{BG}. Control measurements show similar characteristics when V_{BG} is swept for various values of V_{AG}. Within each regime, we observe that V_{BG} shifts the current-vs-V_{AG} curves in a continuous manner. In regime II, V_{BG} can be used as a tuning knob for changing the closed hysteresis loop I_A (V_{AG}). Similar shifts in the characteristics were observed by combining a two-terminal VO_2 device with a field-effect transistor (FET)[45] or by tuning the VO_2 hysteresis itself using ionic-liquid gating.[46,47] Contrary to those studies, our three-terminal devices are both completely reversible and require only a VO_2 film and patterned metal electrodes to function.

The thicker, dashed traces in Fig. 3 highlight the regime boundaries. They represent the current traces shown in Figs. 1(f) and 2. At these regime boundaries, especially I_B and I_G show distinctly different behavior compared to the curve taken at slightly lower V_{BG}. The boundaries thus represent resistive switching events between terminals B and G, triggered by sweeping the voltage between terminals A and B.

15 June 2026 07:11:00

© Author(s) 2026

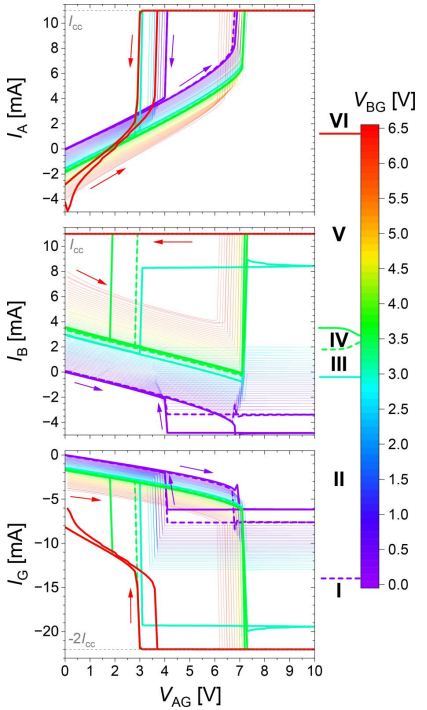


FIG. 3. Continuous tuning of current–voltage characteristics. (a) I_A (V_{AG}), (b) I_B (V_{AG}), and (c) I_G (V_{AG}) for various values of V_{BG}. Between each measurement, V_{BG} was reset to 0 V and increased in increments of 0.1 V from 0 to 6.5 V between subsequent measurements, as indicated by the color scale. Thicker, dashed traces highlight the lowest V_{BG} value for each regime, as described in the text and indicated next to the color scale.

In regimes V and VI, the current I_B measured for $V_{AG} = 0$ V is different before and after the sweep. The control terminal A can thus switch a channel between "drain"—terminal B—and "source"—terminal G—in a hysteretic manner. This functionality closely resembles that of FETs with a memory function,[48,49] an envisioned basic element for in-memory computing. Contrary to FETs, multiterminal ETM devices have interchangeable terminals: input, output, and control are not defined *a priori*; the experiments above show very similar results upon interchanging the A, B, and G terminals. We anticipate that networks of multiterminal ETM devices would have a reconfigurable network topology that depends on the history of inputs to the network. This property is at the heart of emerging network architecture concepts such as memcomputing,[50] evolutionary hardware,[51] and physical learning networks.[52]

To realize such networks, devices should be scalable and operate with low power and latency. These aspects boil down to controlling and reducing the size (volume) of the active (switching) region, i.e., the filament. Multiterminal operation as introduced above is only possible if the filaments are separated geometrically. Hence, for scaling down device size, the filaments must be engineered as narrow as possible. Fortunately, reducing the device length L was shown to reduce the filament width W.[30,53] The filament thickness d should scale with W by radial symmetry.[9] We thus expect the filament volume $V \sim LWd$ to scale down with L^3. These dimensions can be engineered further via the thermal coupling to the environment[9,32–34] and the properties of the active material.[24,39] Volume scaling and thermal engineering were furthermore shown[16,18,38,54] to sharply reduce the required switching power and time (latency). Reducing filament volume will thus benefit strongly the performance and network scalability of multiterminal ETM devices.

We conclude that in multiterminal electrothermal memristors, filaments of the metallic phase can stabilize in various history-dependent configurations. A combination of voltages applied to multiple terminals can control where and when filaments form and vanish. The electric response of our devices depends sensitively, repeatably, and predictably on both the applied inputs and their history. Because filament formation in electrothermal memristors is reversible, local, and fast, multiterminal electrothermal memristors are a promising platform for emerging network architectures with built-in memory functionality.

We thank Christoph Back, Frank Roesthuis, and Daan Wielens for technical support and Jochen Mannhart for helpful discussions. This publication is part of the project NL-ECO: Netherlands Initiative for Energy-Efficient Computing (with Project No. NWA.1389.20.140) of the NWA research programme Research Along Routes by Consortia, which is financed by the Dutch Research Council (NWO).

AUTHOR DECLARATIONS

Conflict of Interest

The authors have no conflicts to disclose.

Author Contributions

Sander Smink: Conceptualization (equal); Data curation (supporting); Formal analysis (lead); Investigation (lead); Methodology (equal); Project administration (supporting); Resources (lead); Supervision (equal); Validation (equal); Visualization (lead); Writing – original draft (lead); Writing – review & editing (lead). **Farnaz Tahouni-Bonab:** Conceptualization (supporting); Data curation (lead); Formal analysis (supporting); Investigation (equal); Resources (supporting); Software (equal); Validation (equal); Visualization (equal); Writing – review & editing (equal). **Wander Schmitz:** Conceptualization (supporting); Data curation (supporting); Formal analysis (supporting); Investigation (supporting); Resources (supporting). **Daniel Janse van Rensburg:** Conceptualization (supporting); Investigation (supporting); Validation (supporting). **Julian van Putten:** Data curation (supporting); Formal analysis (supporting);

15 June 2026 07:11:00

© Author(s) 2026

Investigation (supporting). **Lennart Cool:** Data curation (supporting); Formal analysis (supporting); Investigation (supporting); Writing – review & editing (supporting). **Colin Evers:** Resources (supporting); Writing – review & editing (supporting). **Stefan Guénon:** Conceptualization (supporting); Data curation (supporting); Methodology (supporting); Resources (supporting). **Reinhold Kleiner:** Conceptualization (supporting); Funding acquisition (equal); Project administration (equal); Supervision (equal); Writing – review & editing (supporting). **Dieter Koelle:** Conceptualization (supporting); Funding acquisition (equal); Project administration (equal); Supervision (equal); Writing – review & editing (equal). **Carlos M. M. Rosário:** Conceptualization (equal); Investigation (equal); Resources (supporting). **Hans Hilgenkamp:** Conceptualization (equal); Funding acquisition (equal); Project administration (equal); Supervision (equal); Writing – original draft (supporting); Writing – review & editing (equal).

DATA AVAILABILITY

The data that support the findings of this study are available from the corresponding author upon reasonable request.

REFERENCES

[1] L. Chua and S. M. Kang, "Memristive devices and systems," Proc. IEEE **64**, 209–223 (1976).
[2] A. Ascoli, A. S. Demirkol, R. Tetzlaff, S. Slesazeck, T. Mikolajick, and L. O. Chua, "On local activity and edge of chaos in a NaMLab memristor," Front. Neurosci. **15**, 651452 (2021).
[3] T. D. Brown, S. Kumar, and R. S. Williams, "Physics-based compact modeling of electro-thermal memristors: Negative differential resistance, local activity, and non-local dynamical bifurcations," Appl. Phys. Rev. **9**, 011308 (2022).
[4] T. D. Brown, S. M. Bohaichuk, M. Islam, S. Kumar, E. Pop, and R. S. Williams, "Electro-thermal characterization of dynamical VO_2 memristors via local activity modeling," Adv. Mater. **35**, 2205451 (2023).
[5] M. Brahlek, L. Zhang, J. Lapano, H.-T. Zhang, R. Engel-Herbert, N. Shukla, S. Datta, H. Paik, and D. G. Schlom, "Opportunities in vanadium-based strongly correlated electron systems," MRS Commun. **7**, 27–52 (2017).
[6] F. J. Morin, "Oxides which show a metal-to-insulator transition at the Neel temperature," Phys. Rev. Lett. **3**, 34–36 (1959).
[7] A. Zylbersztejn and N. F. Mott, "Metal-insulator transition in vanadium dioxide," Phys. Rev. B **11**, 4383–4395 (1975).
[8] A. Zimmers, L. Aigouy, M. Mortier, A. Sharoni, S. Wang, K. G. West, J. G. Ramirez, and I. K. Schuller, "Role of thermal heating on the voltage induced insulator-metal transition in VO_2," Phys. Rev. Lett. **110**, 056601 (2013).
[9] I. Valmianski, P. Y. Wang, S. Wang, J. G. Ramirez, S. Guénon, and I. K. Schuller, "Origin of the current-driven breakdown in vanadium oxides: Thermal versus electronic," Phys. Rev. B **98**, 195144 (2018).
[10] L. A. L. de Almeida, G. S. Deep, A. M. Nogueira-Lima, and H. Neff, "Modeling of the hysteretic metal-insulator transition in a vanadium dioxide infrared detector," Opt. Eng. **41**, 2582–2588 (2002).
[11] X. Gao, C. M. M. Rosário, and H. Hilgenkamp, "Multi-level operation in VO_2-based resistive switching devices," AIP Adv. **12**, 015218 (2022).
[12] Y. Zhou and S. Ramanathan, "Mott memory and neuromorphic devices," Proc. IEEE **103**, 1289–1310 (2015).
[13] J. Sakai, "High-efficiency voltage oscillation in VO_2 planer-type junctions with infinite negative differential resistance," J. Appl. Phys. **103**, 103708 (2008).
[14] J. del Valle, P. Salev, F. Tesler, N. M. Vargas, Y. Kalcheim, P. Wang, J. Trastoy, M.-H. Lee, G. Kassabian, J. G. Ramírez, M. J. Rozenberg, and I. K. Schuller, "Subthreshold firing in Mott nanodevices," Nature **569**, 388–392 (2019).
[15] G. Li, D. Xie, H. Zhong, Z. Zhang, X. Fu, Q. Zhou, Q. Li, H. Ni, J. Wang, E.-J. Guo, M. He, C. Wang, G. Yang, K. Jin, and C. Ge, "Photo-induced non-volatile VO_2 phase transition for neuromorphic ultraviolet sensors," Nat. Commun. **13**, 1729 (2022).
[16] S. M. Bohaichuk, S. Kumar, G. Pitner, C. J. McClellan, J. Jeong, M. G. Samant, H.-S. P. Wong, S. S. P. Parkin, R. S. Williams, and E. Pop, "Fast spiking of a Mott VO_2–carbon nanotube composite device," Nano Lett. **19**, 6751–6755 (2019).
[17] G. Li, Z. Wang, Y. Chen, J.-C. Jeon, and S. S. P. Parkin, "Computational elements based on coupled VO_2 oscillators via tunable thermal triggering," Nat. Commun. **15**, 5820 (2024).
[18] Z. Pollner, T. N. Török, L. Pósa, M. Csontos, S. W. Schmid, Z. Balogh, A. Bükkfejes, H. Kim, A. Piqué, J. Leuthold, J. Volk, and A. Halbritter, "VO_2 oscillator circuits optimized for ultrafast, 100 MHz-range operation," Adv. Electron. Mater. **12**, e00433 (2026).
[19] P. Stoliar, J. Tranchant, B. Corraze, E. Janod, M.-P. Besland, F. Tesler, M. Rozenberg, and L. Cario, "A leaky-integrate-and-fire neuron analog realized with a Mott insulator," Adv. Funct. Mater. **27**, 1604740 (2017).
[20] O. Maher, M. Jiménez, C. Delacour, N. Harnack, J. Núñez, M. J. Avedillo, B. Linares-Barranco, A. Todri-Sanial, G. Indiveri, and S. Karg, "A CMOS-compatible oscillation-based VO_2 Ising machine solver," Nat. Commun. **15**, 3334 (2024).
[21] J. Kim, C. Ko, A. Frenzel, S. Ramanathan, and J. E. Hoffman, "Nanoscale imaging and control of resistance switching in VO_2 at room temperature," Appl. Phys. Lett. **96**, 213106 (2010).
[22] X. Zhong, X. Zhang, A. Gupta, and P. LeClair, "Avalanche breakdown in microscale VO_2 structures," J. Appl. Phys. **110**, 084516 (2011).
[23] P. Stoliar, L. Cario, E. Janod, B. Corraze, C. Guillot-Deudon, S. Salmon-Bourmand, V. Guiot, J. Tranchant, and M. Rozenberg, "Universal electric-field-driven resistive transition in narrow-gap Mott insulators," Adv. Mater. **25**, 3222–3226 (2013).
[24] J. del Valle, N. M. Vargas, R. Rocco, P. Salev, Y. Kalcheim, P. N. Lapa, C. Adda, M.-H. Lee, P. Y. Wang, L. Fratino, M. J. Rozenberg, and I. K. Schuller, "Spatiotemporal characterization of the field-induced insulator-to-metal transition," Science **373**, 907–911 (2021).
[25] C. Berglund, "Thermal filaments in vanadium dioxide," IEEE Trans. Electron Devices **16**, 432–437 (1969).
[26] J. Duchene, M. Terraillon, P. Pailly, and G. Adam, "Filamentary conduction in VO_2 coplanar thin-film devices," Appl. Phys. Lett. **19**, 115–117 (1971).
[27] K. Okimura, N. Ezreena, Y. Sasakawa, and J. Sakai, "Electric-field-induced multistep resistance switching in planar VO_2/c-Al_2O_3 structure," Jpn. J. Appl. Phys. **48**, 065003 (2009).
[28] Y. Zhao, J. Hao, C. Chen, and Z. Fan, "Electrically controlled metal–insulator transition process in VO_2 thin films," J. Phys.: Condens. Matter **24**, 035601 (2012).
[29] E. Freeman, G. Stone, N. Shukla, H. Paik, J. A. Moyer, Z. Cai, H. Wen, R. Engel-Herbert, D. G. Schlom, V. Gopalan, and S. Datta, "Nanoscale structural evolution of electrically driven insulator to metal transition in vanadium dioxide," Appl. Phys. Lett. **103**, 263109 (2013).
[30] J. Yoon, G. Lee, C. Park, B. S. Mun, and H. Ju, "Investigation of length-dependent characteristics of the voltage-induced metal insulator transition in VO_2 film devices," Appl. Phys. Lett. **105**, 083503 (2014).
[31] E. Kisiel, P. Salev, I. Poudyal, D. J. Alspaugh, F. Carneiro, E. Qiu, F. Rodolakis, Z. Zhang, O. G. Shpyrko, M. Rozenberg, I. K. Schuller, Z. Islam, and A. Frano, "High-resolution full-field structural microscopy of the voltage-induced filament formation in VO_2-based neuromorphic devices," ACS Nano **19**, 15385–15394 (2025).
[32] S. Guénon, S. Scharinger, S. Wang, J. G. Ramírez, D. Koelle, R. Kleiner, and I. K. Schuller, "Electrical breakdown in a V_2O_3 device at the insulator-to-metal transition," Europhys. Lett. **101**, 57003 (2013).
[33] T. Luibrand, A. Bercher, R. Rocco, F. Tahouni-Bonab, L. Varbaro, C. W. Rischau, C. Domínguez, Y. Zhou, W. Luo, S. Bag, L. Fratino, R. Kleiner, S. Gariglio, D. Koelle, J.-M. Triscone, M. J. Rozenberg, A. B. Kuzmenko, S. Guénon, and J. del Valle, "Characteristic length scales of the electrically induced insulator-to-metal transition," Phys. Rev. Res. **5**, 013108 (2023).
[34] F. Tahouni-Bonab, M. Hepting, T. Luibrand, G. Cristiani, C. Schmid, G. Logvenov, B. Keimer, R. Kleiner, D. Koelle, and S. Guénon, "Nonvolatile multistate electrothermal resistive switching in a strongly correlated insulator thin-film device," Phys. Rev. Appl. **24**, 034014 (2025).
[35] R. Waser, R. Dittmann, G. Staikov, and K. Szot, "Redox-based resistive switching memories—Nanoionic mechanisms, prospects, and challenges," Adv. Mater. **21**, 2632–2663 (2009).

15 June 2026 07:11:00

© Author(s) 2026

[36]H.-S. P. Wong, H.-Y. Lee, S. Yu, Y.-S. Chen, Y. Wu, P.-S. Chen, B. Lee, F. T. Chen, and M.-J. Tsai, "Metal–oxide RRAM," Proc. IEEE **100**, 1951–1970 (2012).
[37]J. S. Brockman, L. Gao, B. Hughes, C. T. Rettner, M. G. Samant, K. P. Roche, and S. S. P. Parkin, "Subnanosecond incubation times for electric-field-induced metallization of a correlated electron oxide," Nat. Nanotechnol. **9**, 453–458 (2014).
[38]S. W. Schmid, L. Pósa, T. N. Török, B. Sánta, Z. Pollner, G. Molnár, Y. Horst, J. Volk, J. Leuthold, A. Halbritter, and M. Csontos, "Picosecond femtojoule resistive switching in nanoscale VO_2 memristors," ACS Nano **18**, 21966–21974 (2024).
[39]M. Lange, S. Guénon, Y. Kalcheim, T. Luibrand, N. M. Vargas, D. Schwebius, R. Kleiner, I. K. Schuller, and D. Koelle, "Imaging of electrothermal filament formation in a Mott insulator," Phys. Rev. Appl. **16**, 054027 (2021).
[40]X. Gao, T. J. Roskamp, T. Swoboda, C. M. M. Rosário, S. Smink, M. Muñoz Rojo, and H. Hilgenkamp, "Multibridge VO_2-based resistive switching devices in a two-terminal configuration," Adv. Electron. Mater. **9**, 2300304 (2023).
[41]K. M. Mayer, R. Gross, J. Parisi, J. Peinke, and R. P. Huebener, "Spatially resolved observation of current filament dynamics in semiconductors," Solid State Commun. **63**, 55–59 (1987).
[42]J. Mannhart, J. Parisi, K. Mayer, and R. Huebener, "A new cryoelectronic device family," IEEE Trans. Electron Devices **34**, 1802–1806 (1987).
[43]H.-T. Zhang, L. Zhang, D. Mukherjee, Y.-X. Zheng, R. C. Haislmaier, N. Alem, and R. Engel-Herbert, "Wafer-scale growth of VO_2 thin films using a combinatorial approach," Nat. Commun. **6**, 8475 (2015).
[44]M. Lange, S. Guénon, F. Lever, R. Kleiner, and D. Koelle, "A high-resolution combined scanning laser and widefield polarizing microscope for imaging at temperatures from 4 K to 300 K," Rev. Sci. Instrum. **88**, 123705 (2017).
[45]N. Shukla, A. Thathachary, A. Agrawal, H. Paik, A. Aziz, D. Schlom, S. Gupta, R. Engel-Herbert, and S. Datta, "A steep-slope transistor based on abrupt electronic phase transition," Nat. Commun. **6**, 7812 (2015).
[46]M. Nakano, K. Shibuya, D. Okuyama, T. Hatano, S. Ono, M. Kawasaki, Y. Iwasa, and Y. Tokura, "Collective bulk carrier delocalization driven by electrostatic surface charge accumulation," Nature **487**, 459–462 (2012).
[47]J. Jeong, N. Aetukuri, T. Graf, T. D. Schladt, M. G. Samant, and S. S. P. Parkin, "Suppression of metal-insulator transition in VO_2 by electric field–induced oxygen vacancy formation," Science **339**, 1402–1405 (2013).
[48]J. S. Meena, S. M. Sze, U. Chand, and T.-Y. Tseng, "Overview of emerging nonvolatile memory technologies," Nanoscale Res. Lett. **9**, 526 (2014).
[49]V. K. Sangwan, H.-S. Lee, H. Bergeron, I. Balla, M. E. Beck, K.-S. Chen, and M. C. Hersam, "Multi-terminal memtransistors from polycrystalline monolayer molybdenum disulfide," Nature **554**, 500–504 (2018).
[50]M. Di Ventra and F. L. Traversa, "Perspective: Memcomputing: Leveraging memory and physics to compute efficiently," J. Appl. Phys. **123**, 180901 (2018).
[51]S. K. Bose, C. P. Lawrence, Z. Liu, K. S. Makarenko, R. M. J. van Damme, H. J. Broersma, and W. G. van der Wiel, "Evolution of a designless nanoparticle network into reconfigurable Boolean logic," Nat. Nanotechnol. **10**, 1048–1052 (2015).
[52]M. Stern, D. Hexner, J. W. Rocks, and A. J. Liu, "Supervised learning in physical networks: From machine learning to learning machines," Phys. Rev. X **11**, 021045 (2021).
[53]J. Yoon, H. Kim, B. S. Mun, C. Park, and H. Ju, "Investigation on onset voltage and conduction channel temperature in voltage-induced metal-insulator transition of vanadium dioxide," J. Appl. Phys. **119**, 124503 (2016).
[54]Y. Higuchi, T. Kanki, and H. Tanaka, "Joule-heat-driven high-efficiency electronic-phase switching in freestanding VO_2/TiO_2 nanowires," Appl. Phys. Express **10**, 033201 (2017).

15 June 2026 07:11:00

© Author(s) 2026

Acknowledgements

"Physics helped me find happiness again."

From the bottom of my heart, I would like to thank everyone who stood by my side throughout my PhD journey—my family, friends, colleagues, and supervisors. Your support, patience, and encouragement gave me the strength to overcome every challenge and reach this milestone.